Doctoral Dissertation

Two-dimensional metal-free carbon nitride materials as catalysts for energy applications (CO_2RR, N_2RR, and ORR): A density functional theory study

エネルギー分野への応用（CO_2RR、N_2RR 及び ORR）における触媒としての二次元メタルフリー窒化炭素材料：密度汎関数理論の研究

WANG YUELIN

October 2023

Graduate School of Engineering,
Osaka University

Abstract

Metal-free carbon nitride materials (CN_x) have exhibited impressive catalytic activity for various energy conversion reactions, such as carbon dioxide reduction reaction (CO_2RR), nitrogen reaction reaction/nitrogen fixation (N_2RR), and oxygen reduction reaction (ORR). Their unique surface chemistry and abundant functional groups facilitate the interaction with reactants, leading to improved reaction kinetics and selectivity. In this thesis, to investigate the specific active site in CN_x for different catalytic reactions (CO_2RR, N_2RR, and ORR), I used density functional theory (DFT) to calculate the catalytic mechanism and activity of CO_2RR, N_2RR, and ORR on C_3N_5, B-doped g-C_9N_{10} and N-doped graphdiyne (NGDY), respectively.

Firstly, N=N linkage has Lewis base sites, which can be hybridized with Lewis acid molecule CO_2, and may improve CO_2RR activity. To prove this, a new-type nitrogen-rich carbon nitride material, C_3N_5 with azo (–N=N–) linkage, was investigated as a photocatalyst for CO_2 reduction. The DFT results showed the C_3N_5 has a longer visible-light region in the absorption spectrum with 2.0 eV of band gap. Compared with g-C_3N_4, which has a band gap of 2.7 eV, the C_3N_5 has much higher photocatalytic efficiency than g-C_3N_4. The Gibbs free energies for possible CO_2 reaction paths on C_3N_5 showed that CO_2 can be efficiently reduced to CH_4 and CH_3CH_2OH.

Secondly, the B atom is an electron-deficient atom with Lewis acid characteristics that can drive the "σ donation-π backdonation" with Lewis base N_2. To prove this, I systemically investigated the mechanism of N_2 adsorption and fixation on B-doped g-C_9N_{10}, a new carbon nitride material, with three different doping configurations, namely substitutions of B at C (B_{C1}), N (B_{N1}) sites, and B anchored g-C_9N_{10} (B_A). I found that N_2RR can only proceed on B_{N1} and B_A due to N_2 chemisorption ability. B_{N1} has a good N_2RR catalytic activity and selectivity while doping B_A is blocked by H poisoning due to stronger binging with H.

Finally, unlike graphene, GDY has a large pore with high mass transfer efficiency and is composed of sp- and sp^2-hybridized carbon atoms with a nonuniform electronic distribution. N-doping was found to favor sp-hybridized carbon atoms as the most preferable sites, and these sp-N were identified as highly attractive centers for capturing O_2 molecules. To prove this, I systematically studied the ORR mechanism on sp-N1GDY and pyridinic (Pyri)-NGDY support by graphene (G) with solvation effect. I found that the dissociative mechanism is preferred on sp-N1GDY/G and the surface is easily terminated by the OH* intermediate, while the OH* pre-adsorbed surface (sp-N1GDY(OH)/G) prefers the associative mechanism. Pyri-NGDY/G also prefers the associative mechanism without any termination. Then, the solvation effect stabilizes all ORR intermediates in both cases. From the calculated free energy diagram, a model with water solvent gives a more appropriate estimation of the overpotential than the one without water solvent, and sp-N1GDY/G with OH* pre-adsorbed has a lower overpotential (0.46 V) which is close to the experiment value (0.36 V), compared with Pyri-NGDY/G (0.75 V).

From my works, I would like to emphasize that depending on target reactions, it is possible to introduce specific active sites to design new catalysts based on theoretical simulations.

I dedicate this thesis to my beloved parents and husband.

Contents

Chapter 1

General Introduction

The growing global population and the rapid increase in reliance on advanced electronic devices have resulted in a significant rise in global energy consumption. The development of clean and sustainable energy conversion systems has become of paramount importance. These energy conversions rely on several important reactions including oxygen reduction reaction (ORR), oxygen evolution reaction (OER), hydrogen evolution reaction (HER), carbon dioxide reduction reaction (CO_2RR), and nitrogen reduction reaction (N_2RR). All of these reactions require photocatalysts or electrocatalysts, making it a good strategy to address environmental problems [1-3]. Currently, metal-based catalysts are widely employed but suffer from several inherent disadvantages, including low selectivity, poor durability, and negative environmental impacts [4]. Therefore, there is a pressing need to develop alternative catalysts that are readily available, cost-effective, and exhibit comparable or even superior catalytic performance to metal-based catalysts.

In 2009, Dai *et al.* reported that nitrogen-doped carbon nanotubes (N-CNTs) were discovered as the first metal-free carbon-based electrocatalysts for the oxygen reduction reaction [5]. This finding triggers the interesting field of carbon-based metal-free catalysts, especially carbon nitride materials (CN_x), for growing exponentially to include ORR, OER, HER, NRR, CO_2RR, and many other reactions. CN_x can be divided into nitrogen-poor (CN_x, $x < 1$) nitrogen-doped (N-doped) carbon materials, and nitrogen-rich carbon nitride materials (CN_x, $x > 1$) [6]. Figure 1.1 shows the typically metal-free CN_x-based materials as catalysts for energy applications in the last ten years [7-13]. Chen *et al.* reported that N-doped holey graphene sheets show remarkable electrocatalytic activity for both hydrazine oxidation and oxygen reduction [8]. Zhao *et al.* reported that carbon nitride ($g\text{-}C_3N_4$) based multi-functional

nanocomposite (PCCN) for light-driven water splitting, exhibited great activity [10]. Dai group synthesized the silicon (Si) and nitrogen (N) co-doped porous carbon, which increased CO_2 reduction and O_2 evolution activity, as a result, they achieved photovoltaic-driven neutral CO_2 overall splitting using a metal-free bifunctional electrocatalyst [11]. Liu *et al.* reported that defective carbon-doped boron nitride nanosheets (C-BN) exhibit exceptional electrocatalytic activity and long-term durability [12]. While Figure 1.1 may not capture every detail, it serves as a valuable framework and overview for examining the progress in the development of multifunctional carbon-based metal-free catalysts. This includes aspects such as structure design, synthesis methods, the mechanism of multifunctional electrocatalysis, and potential applications, as well as the existing challenges and prospects in this dynamic field.

2022

(g)

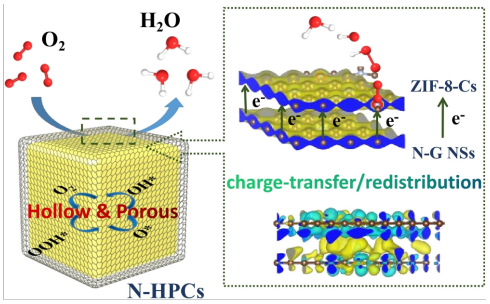

An N-doped hollow and hierarchically porous carbon nanocage catalyst exhibits excellent ORR performance in both alkaline and acidic media [13].

2020

(f)

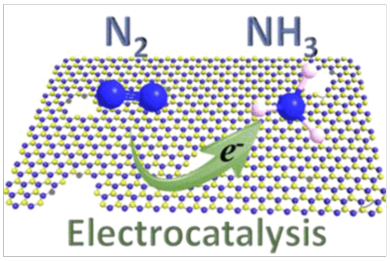

Defective carbon-doped boron nitride nanosheets (C-BN) show excellent electrocatalytic activity and durability in N_2 fixation [12].

2018

(e)

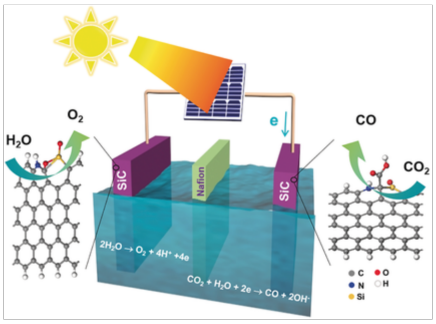

Silicon and nitrogen co-doped porous carbon synthesized by pyrolysis exhibited good CO_2RR and OER activity [11].

2016

(d)

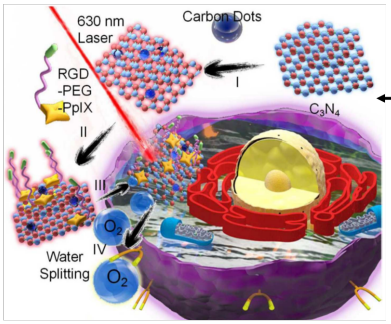

Carbon nitride (g-C_3N_4) based multi-functional nano-composite (PCCN) for light-driven water splitting [10].

2014

(c)

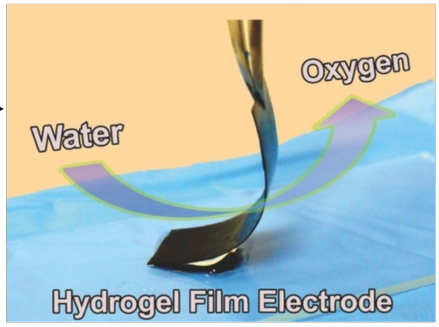

N, O co-doped graphene nanotube hydrogel film shows a remarkable OER catalytic performance [9].

2013

(b)

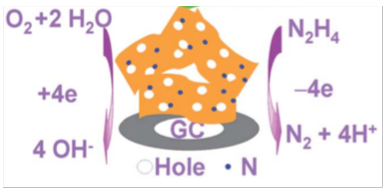

N-doped holey graphene sheets show a remarkable electro-catalytic activity for both hydrazine oxidation and oxygen reduction [8].

2011

(a)

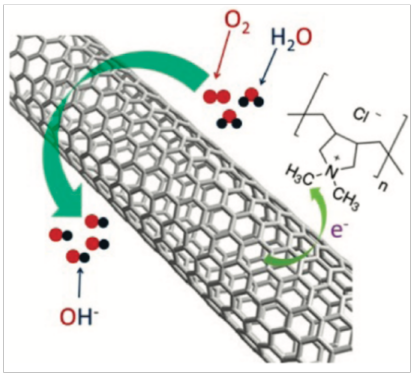

Certain polyelectrolyte (e.g., PDDA) functionalized carbon nanotubes for ORR [7].

Figure 1.1: Important developments in multifunctional metal-free CN_x-based materials catalysts: a timeline. (a) Reprinted with permission from [7]. Copyright 2011 American Chemical Society, (b) Reprinted with permission from [8]. Copyright 2013 Royal Society of Chemistry. (c) Reprinted with permission from [9]. Copyright 2014 Wiley-VCH. (d) Reprinted with permission from [10]. Copyright 2016 American Chemistry Society. (e) Reprinted with permission from [11]. Copyright 2018 Wiley-VCH. (f) Reprinted with permission from [12]. Copyright 2020 American Chemical Society. (g) Reprinted with permission from [13]. Copyright 2022 Wiley-VCH.

1.1 CO_2 Reduction Reaction (CO_2RR)

1.1.1 Fundamentals of CO_2RR

The continuous increase in CO_2 concentration in the atmosphere has resulted in global warming and various experimental challenges. Effectively reducing CO_2 concentration in the air has become a crucial worldwide research topic. Carbon capture and storage (CCS) [14], which involves storing atmospheric CO_2 underground in a supercritical state, was once considered one of the most feasible methods for reducing airborne CO_2 concentration. However, this technology is inherently energy-intensive, prone to leaks, and non-renewable. In contrast to carbon capture and storage, CO_2 conversion strategies offer a more direct approach to reducing CO_2 levels by transforming them into high-value-added chemicals or fuels, thus achieving carbon recycling. CO_2 conversion strategies primarily encompass photocatalytic and electrocatalytic methods [15-17].

Motivated by the process of photosynthesis in plants, the photocatalytic reduction of CO_2 has gained growing interest and is recognized as one of the most promising approaches for generating renewable fuels through photoexcitation [18-23]. In 1979, the Honda research group

first used semiconductors (TiO_2) for photocatalytic reduction of CO_2 to organic compounds such as HCOOH, HCHO, CH_3OH, and CH_4 [24]. Based on this finding, more and more semiconductor materials are being applied to the photocatalytic conversion of CO_2.

Conceptually, photocatalysis involves three steps [25-26], as illustrated in Figure 1.2. In the first step, under light illumination of nanoparticles of semiconductors, electrons are excited to generate in the conduction band (CB), and holes are generated in the valence band (VB). These electron-hole pairs can either recombine within the bulk or diffuse toward the surface, leading to the second step, which entails charge separation and surface diffusion. Due to the presence of numerous defects and dangling bonds in nanoparticles, these imperfections can capture electrons and holes, preventing their recombination [25]. In the third step, the photogenerated electrons and holes respectively participate in reducing CO_2 and oxidizing H_2O.

Electrocatalytic CO_2RR involves using catalysts to facilitate the conversion of CO_2 at the cathode of an electrochemical cell. The catalyst promotes the reduction of CO_2 molecules, enabling the formation of fuels like carbon monoxide (CO), methane (CH_4), and ethylene (C_2H_4). The applied potential provides the necessary energy to drive the reaction, and the choice of catalyst material and structure significantly influences the reaction selectivity and efficiency [16, 27-28].

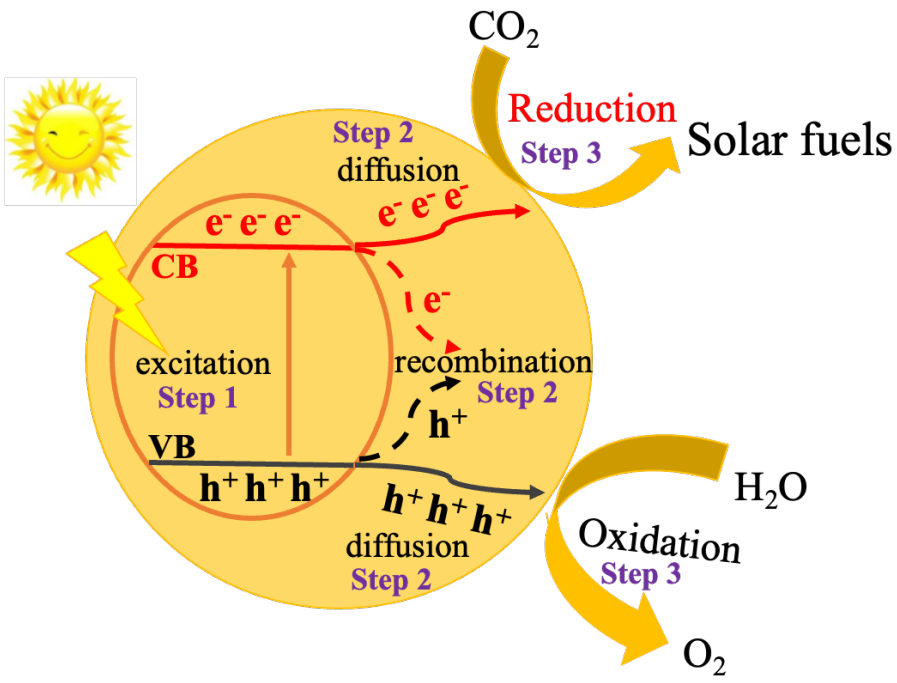

Figure 1.2: The three-step process of photocatalysis: (1) photoexcitation, (2) charge separation or recombination, and (3) charge transfer along with the corresponding oxidation and reduction reactions.

1.1.2 CO_2RR Mechanism

Investigating the reaction mechanism provides a deeper understanding of the CO_2RR, offering theoretical insights and guidance for designing novel and efficient CO_2RR catalysts. Experimentally, detecting intermediates involved in CO_2RR in aqueous electrochemical environments or photochemical environments poses significant challenges. The abundance of intermediates and the complexity of reaction pathways make it difficult to determine the effectiveness of a specific pathway. By employing DFT calculations, researchers can explore various reaction pathways, identify intermediate species, and determine the transition states and reaction barriers. This comprehensive analysis provides valuable insights into the intricate steps and mechanisms governing the catalytic reaction. The computational hydrogen electrode (CHE) model, as proposed by the Nørskov group [29], is one of the most used methods for

thermodynamically analyzing catalytic reactions (such as CO_2 reduction, N_2RR, and ORR) among the numerous existing calculation models [30-32]. CO_2RR is a multi-electron transfer mechanism that leads to a complex reaction pathway. Common CO_2RR reduction single-carbon (C1) products include carbon monoxide (CO, 2-electron transfer), formic acid/formate (HCOOH/HCOO, 2-electron transfer), formaldehyde (HCHO, 4-electron transfer), methanol (CH_3OH, 6-electron transfer), and methane (CH_4, 8-electron transfer) as shown in Figure 1.3. Multi-carbon compounds such as C2 and C3 can also be created by the C-C coupling process. Ethylene (C_2H_4), ethane (C_2H_6), and ethanol (C_2H_5OH) are the most common C2 and C3 products, respectively. In most multi-carbon compounds, the creation of the C–C bond is the most important step. The two chemical routes for C–C bond formation, according to earlier theoretical study, are (1) dimerization of two CO molecules; and (2) CO attaches to unsaturated coordination intermediates (e.g., CHO*, CH*, and CH_2*). The chemical process to produce the C2 product is depicted in Figure 1.4.

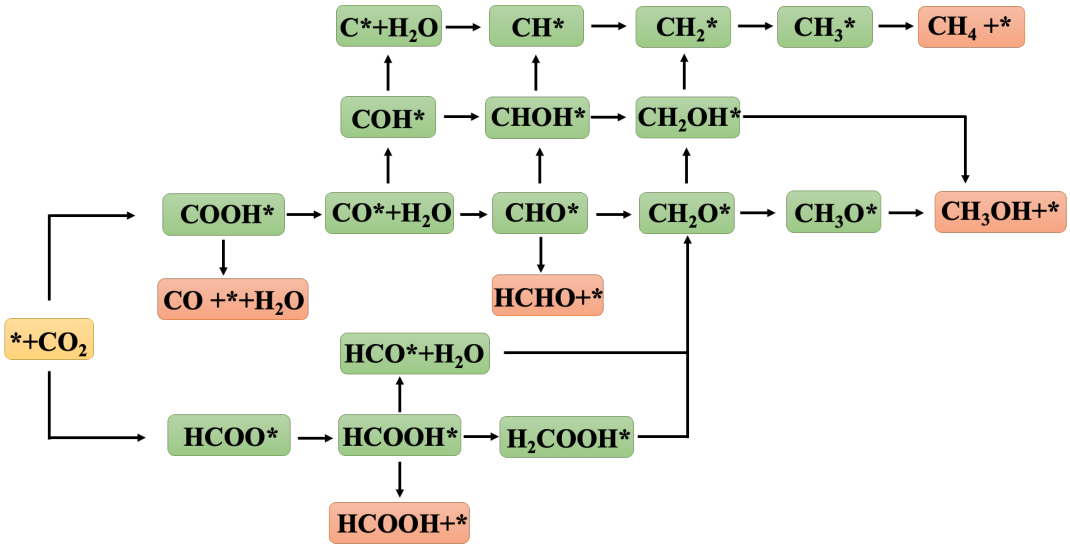

Figure 1.3: The mechanism pathways for CO_2RR producing C1 products.

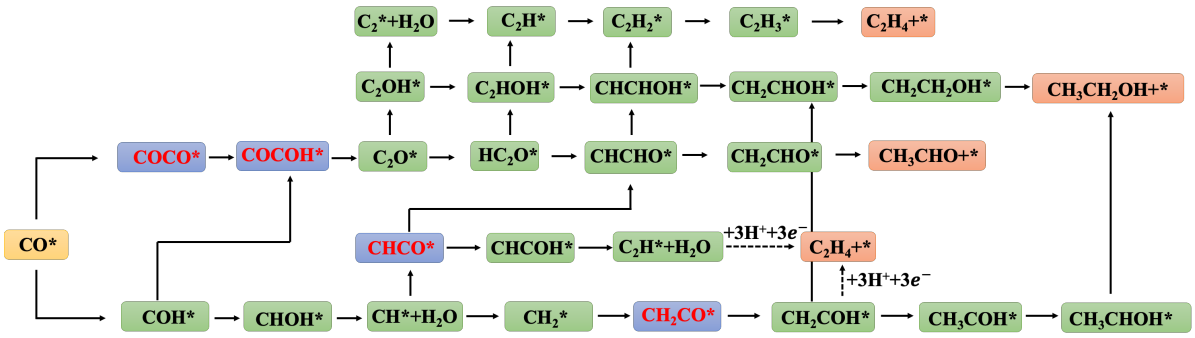

Figure 1.4: The mechanism pathways for CO_2RR producing C2 products.

1.1.3 CN_x Catalysts for CO_2RR

In recent years, CN_x materials have attracted attention as a catalyst for CO_2RR. Specifically, nitrogen-rich carbon nitrides with –NH and $–NH_2$ groups have Lewis-base sites, which enhance CO_2 adsorption capacity [6, 33]. Zhang *et al.* [34] applied porous structured g-C_3N_4 in CO_2 photocatalytic reduction to CO, and the introduction of porosity enhanced the photooxidation capability of graphitic carbon nitride by providing more photogenerated holes and active sites compared to bulk structures [34]. Peng and the co-author reported the direct heating of urea or melamine to produce two types of g-C_3N_4 photocatalysts capable of reducing CO_2 to organic fuels under visible light. These photocatalysts exhibited varying photoactivity and selectivity in the formation of CH_3OH and C_2H_5OH [35]. Enriched C vacancies in graphitic carbon nitride increased CO_2 to CO conversion rates by more than twofold, thanks to enhanced CO_2 adsorption/activation, an elevated conduction band, and improved charge carrier concentration and lifetime [36]. Vinu and colleagues documented that mesoporous carbon nitrides possessing a well-organized 3D structure and a substantial nitrogen content exhibit a distinctive CN framework characterized by a C and N stoichiometry of C_3N_5. These materials displayed an impressive CO_2 capture capacity of up to 5.63 mmol g^{-1} at 273 K and 30 bar [33].

1.2 N_2 Reduction Reaction/N_2 Fixation (N_2RR)

1.2.1 Fundamentals of N_2RR

In industrial processes, ammonia (NH_3) plays a vital role as both an essential agricultural fertilizer and a key industrial chemical. Traditionally, its synthesis occurs at elevated temperatures (350-550 °C) and high pressures (150-350 atm) through the energy- and capital-intensive Haber-Bosch process. This process, however, not only consumes a lot of energy but also produces a lot of greenhouse gases. Researchers discovered that photocatalytic or electrocatalytic N_2 reduction is an efficient way to achieve long-term NH_3 production [37-41]. Similar to photocatalytic and electrocatalytic processes on CO_2RR, the photocatalytic N_2RR process also can be separated into three stages. The photoelectrons are excited to jump from VB to CB of photocatalysts while holes are generated in the VB of photocatalysts. Then, charge separation and diffusion to the photocatalysts surface, occurs when these electron-hole pairs either recombine or diffuse toward the photocatalysts surface. Finally, the photogenerated electrons and holes can reduce N_2 and oxidized H_2O on photocatalyst surfaces, respectively [42]. In electrocatalytic N_2RR, a cathode is employed within an electrochemical cell, and a catalyst is applied to facilitate the N_2 to NH_3 conversion. The reaction involves the reduction of N_2 molecules through the addition of protons (H^+) and electrons (e^-), leading to the formation of ammonia [42]. Efficient catalysts play a pivotal role in enabling this process by lowering the activation energy required for the reaction and enhancing its overall efficiency.

1.2.2 N_2RR Mechanism

The N_2 molecule is made up of two N atoms that have been linearly combined (Figure 1.5 (a)). Each N atom contains two electrons in the 2s orbital, with opposite spin directions, and three lone-pair electrons in the 2p orbital, all sharing the same spin direction. (Figure 1.5 (a)).

Following atomic orbital hybridization, new bonding orbitals (σ and π orbitals) and antibonding orbitals (σ* and π* orbitals) emerge. The shared electrons in these orbitals contribute to the formation of a highly intense triple bond (N≡N). The single electron transfer reaction is significantly complicated due to a substantial gap of 10.82 eV between the highest occupied molecular orbital (HOMO) and the lowest unoccupied molecular orbital (LUMO), coupled with a high ionization energy of 15.58 eV. These factors indeed hinder the electron transfer [43-44]. One effective approach for weakening the N≡N triple bond involves the utilization of active centers. The processes involved in N_2RR encompass N_2 adsorption, activation, cleavage of the N≡N bond, hydrogenation of adsorbed N_2 molecules or N atoms, and NH_3 desorption. Various mechanisms have been proposed for the conversion of N_2 into NH_3, with the most prevalent ones being the dissociative and associative pathways. The associative pathways can be further categorized into alternating, distal, and enzymatic pathways (Figure 1.5 (b)) [45-48].

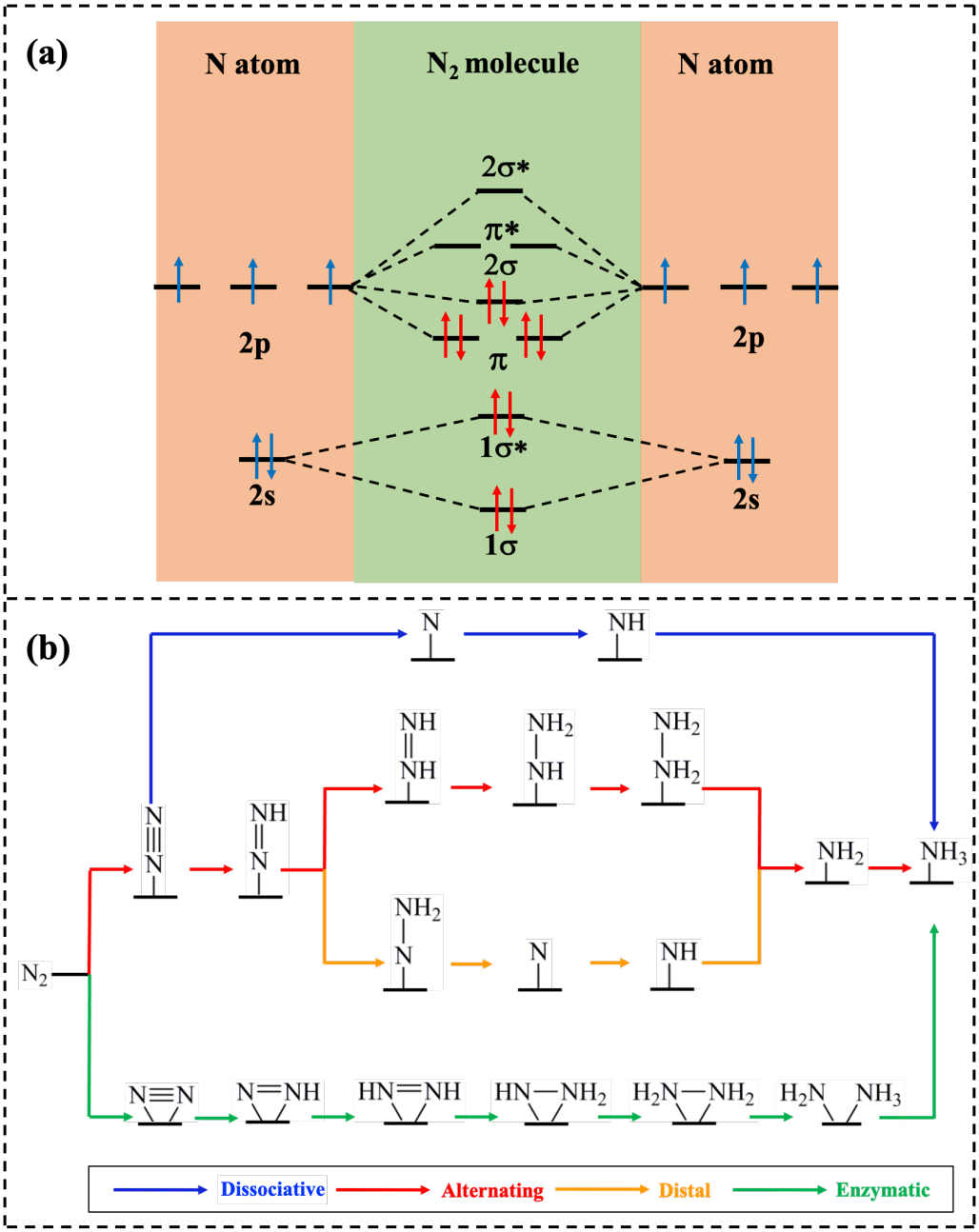

Figure 1.5: (a) Orbitals of N atoms and their linear combination to create N_2 molecular orbitals. (b) Illustration of reaction pathways involved in the conversion of N_2 to NH_3, encompassing both dissociative and associative pathways (distal, alternating, and enzymatic pathways).

1.2.3 CN_x Catalysts for N_2RR

Photocatalytic and electrocatalytic N_2 fixation are captivating and demanding approaches for achieving artificial nitrogen fixation under mild conditions. These approaches leverage

abundant and renewable solar energy as the driving force, and the electricity needed for N_2RR can be generated from sustainable sources such as solar and wind energy [49-50]. The pioneering investigation into photocatalytic N_2 fixation can be attributed to Schrauzer and Guth, who reported their findings in 1977, their study demonstrated that iron-doped TiO_2 exhibited photocatalytic activity in reducing molecular nitrogen (N_2) to ammonia under UV light irradiation [51]. During the last 5-6 years, CN_x materials have also been studied as catalysts for N_2RR/N_2 fixation [50-56]. Dong *et al.* discovered that nitrogen vacancies (NVs) can endow g-C_3N_4 with photocatalytic N_2 fixation capability [50]. Zhao *et al.* reported that N-doped porous carbon (NPC) was effective for fixating N_2 to ammonia and produced a high rate of ammonia [52]. Aside from N doping, due to its lower electronegativity and positive charge upon incorporation in the CN_x, boron (B) serves as an ideal Lewis acid site for binding N_2, which is a weak Lewis base. This interaction provides opportunities for N_2 activation and catalytic transformations, offering potential advancements in the field of nitrogen fixation [53-55]. Recently, Wang *et al.* simulated N_2RR on B-doped g-C_3N_4 photocatalyst by DFT. The findings show that B-doped g-C_3N_4 can effectively reduce N_2 to NH_3 and effectively expand the visible light absorption range, making it an ideal material for photocatalytic N_2 reduction [56]. Hao *et al.* reported that boron-enriched carbonitride (BCN) materials exhibited outstanding NRR performance, together with excellent stability [57]. The DFT results indicate that the boron sites within BCN facilitate low-energy barriers for the rate-determining steps of N_2RR and promote the spontaneous adsorption of nitrogen.

1.3 Oxygen Reduction Reaction (ORR)

1.3.1 Fundamentals of ORR

The identification and adoption of a sustainable energy resource to replace fossil fuels is a critical and pressing task for addressing global environmental concerns. Fossil fuels, which are finite and non-renewable, release significant amounts of greenhouse gases when burned, leading to the acceleration of climate change and other environmental problems. In recent years, fuel cell (FC) technology has emerged as a promising alternative to traditional combustion-based energy sources [58-59]. FC generates electricity from clean and renewable fuels, such as hydrogen or methanol, without the release of harmful pollutants or greenhouse gases, except for water vapor. As a result, FC technology has gained significant attention from policymakers, industry leaders, and scientists as a potential solution to meet the world's growing energy demand while mitigating the adverse effects of greenhouse gas emissions on the environment [60-65]. FC is an electrochemical cell that employs a set of redox processes to convert the chemical energy of a fuel, typically hydrogen, and an oxidizing agent, commonly oxygen, into electricity. (Figure 1.6). ORR is a crucial reaction in the cathode [66, 67]. The dynamic process of ORR is slow due to the multi-step electron transfer process, which has a significant impact on the energy conversion efficiency of fuel cells and limits their use on a broad scale [68-70]. As a result, much effort is put into developing ORR electrocatalysts with high efficiency, cheap cost, and long durability.

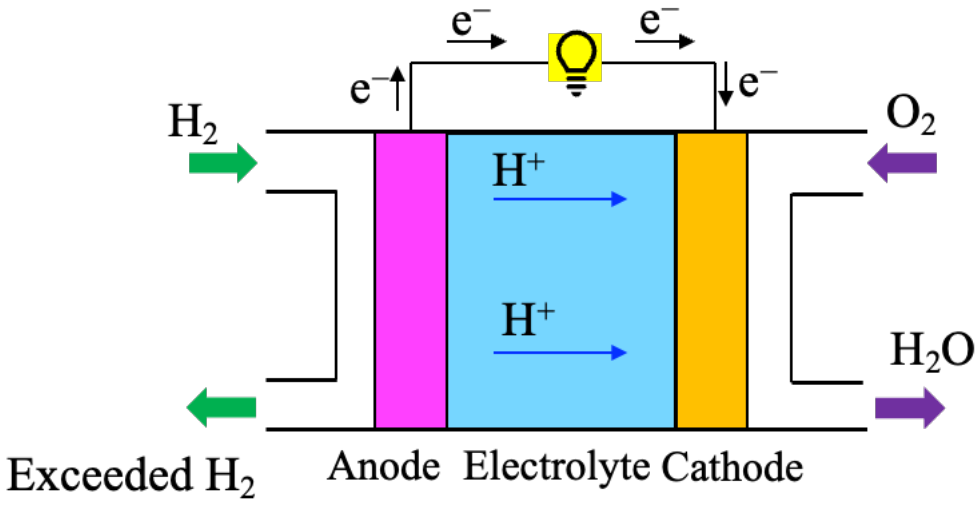

Figure 1.6: Schematic diagram of the fuel cells.

1.3.2 ORR Mechanism

The kinetics of the ORR is a complex process involving multiple steps of electron transfer, specifically the transfer of four electrons. However, the complexity of ORR kinetics extends beyond electron transfer and encompasses significant influences from factors such as the pH value, solvation effects, and polarity of water. Extensive literature confirms that metal-free carbon electrocatalysts exhibit remarkable activity for ORR in alkaline solutions. However, in acidic electrolytes, the catalytic performance of these carbon-based catalysts is significantly inferior to that of metal-based catalysts (especially Pt) [71-73]. In electrocatalytic reactions following the inner-sphere Helmholtz plane electron transfer (ET-IHP) mechanism, it is commonly postulated that the initial step involves either the adsorption of reactant species (either through dissociative or non-dissociative pathways) or an electron transfer process [74]. However, within the numerous elementary reaction steps involved in the oxygen reduction reaction (ORR), there may exist a surface-independent outer-sphere Helmholtz plane electron transfer (ET-OHP) [75, 76] component that contributes to the overall electrocatalytic process of the four-electron ET-IHP. As shown in Figure 1.7, utilizing the pH-relevant RHE as the

reference electrodes, Ramaswamy and Mukerjee demonstrated that the overpotential for the initial electron-transfer step ($O_2/O_2^{\bullet-}$) decrease from 1.53 V (vs. SHE) at pH = 0 to 0.7 V (vs. SHE) at pH = 14 [77]. Because of the substantial overpotential needed for the $O_2/O_2^{\bullet-}$ redox reaction in acidic environments, only particular catalyst surfaces, like platinum, which possess significant adsorption energy for O_2, can facilitate the ORR process in acidic conditions [77]. Nonetheless, within alkaline solutions, the reduction in overpotential for $O_2/O_2^{\bullet-}$ allows almost all electronically conducting electrode materials to demonstrate ORR activity in alkaline pH environments, indicating ORR will be following the ET-OHP mechanism. Due to the lack of reactivity in O_2 chemisorption, achieving high ORR activity at low pH is challenging for carbon materials [78]. Choi *et al.* [79] reported that in N-doped graphene, the ET-OHP mechanism still can react in acidic conditions, due to DFT results, it has been observed that there are scarcely any thermodynamically favorable sites for O_2 binding in proximity to the N-doped graphene sites, except the graphitic-N sites, while in the experiment the ORR activity on N-doped graphene is very good in acidic condition. Therefore, the ET-OHP mechanism offers a potential solution to the challenge of identifying thermodynamically unstable O_2 binding sites in carbon materials.

The overall reaction equation of ORR in fuel cells in acidic is as shown in the following:

$$O_2 + 4e^- + 4H^+ \rightarrow 2H_2O \quad (1\text{-}1)$$

The ET-IHP mechanism also can be divided into dissociative pathway and associative mechanism, dissociative pathway is generally considered to go through the following steps:

$$O_2 + * \rightarrow O_2^* \rightarrow 2O^* \quad (1\text{-}2)$$

$$2O^* + H^+ + e^- \rightarrow O^* + OH^* \quad (1\text{-}3)$$

$$O^* + OH^* + H^+ + e^- \rightarrow O^* + H_2O \quad (1\text{-}4)$$

$$O^* + H^+ + e^- \rightarrow OH^* \quad (1\text{-}5)$$

$$OH^* + H^+ + e^- \rightarrow H_2O \quad (1\text{-}6)$$

The associative mechanism goes through the following elementary steps:

$$O_2 + * \rightarrow O_2^* \quad (1\text{-}7)$$

$$O_2^* + H^+ + e^- \rightarrow OOH^* \quad (1\text{-}8)$$

$$OOH^* + H^+ + e^- \rightarrow O^* + H_2O \quad (1\text{-}9)$$

$$O^* + H^+ + e^- \rightarrow OH^* \quad (1\text{-}5)$$

$$OH^* + H^+ + e^- \rightarrow H_2O \quad (1\text{-}6)$$

For alkaline conditions, the proton donor will be H_2O rather than H_3O^+, so the overall reaction equation will change to:

$$O_2 + 4e^- + 2H_2O \rightarrow 4OH^- \quad (1\text{-}10)$$

For the dissociative pathway, it will be the following steps:

$$O_2 + * \rightarrow O_2^* \rightarrow 2O^* \quad (1\text{-}2)$$

$$2O^* + H_2O + e^- \rightarrow O^* + OH^* + OH^- \quad (1\text{-}11)$$

$$O^* + OH^* + e^- \rightarrow O^* + OH^- \quad (1\text{-}12)$$

$$O^* + H_2O + e^- \rightarrow OH^* + OH^- \quad (1\text{-}13)$$

$$OH^* + e^- \rightarrow OH^- + * \quad (1\text{-}14)$$

and associative mechanism proceeds as follows:

$$O_2 + * \rightarrow O_2^* \quad (1\text{-}7)$$

$$O_2^* + H_2O + e^- \rightarrow OOH^* + OH^- \quad (1\text{-}15)$$

$$OOH^* + e^- \rightarrow O^* + OH^- \quad (1\text{-}16)$$

$$O^* + H_2O + e^- \rightarrow OH^* + OH^- \quad (1\text{-}13)$$

$$OH^* + e^- \rightarrow OH^- + * \quad (1\text{-}14)$$

ET-OHP mechanism refers to the process of long-range electron transfer to non-adsorbed O_2 occurring on the outer Helmholtz plane. In acidic conditions, the mechanism will be as follows:

$$O_2 + H^+ + e^- + * \rightarrow \bullet OOH\ (aq) \rightarrow OOH^* \quad (1\text{-}17)$$

$$OOH^* + H^+ + e^- \rightarrow O^* + H_2O \quad (1\text{-}9)$$

$$O^* + H^+ + e^- \rightarrow OH^* \quad (1\text{-}5)$$

$$OH^* + H^+ + e^- \rightarrow H_2O \quad (1\text{-}6)$$

In alkaline conditions, the mechanism will be as follows:

$$O_2 + H_2O + e^- + * \rightarrow \bullet OOH\ (aq) \rightarrow OOH^* + OH^- \quad (1\text{-}18)$$

$$OOH^* + e^- \rightarrow O^* + OH^- \quad (1\text{-}16)$$

$$O^* + H_2O + e^- \rightarrow OH^* + OH^- \quad (1\text{-}13)$$

$$OH^* + e^- \rightarrow OH^- + * \quad (1\text{-}14)$$

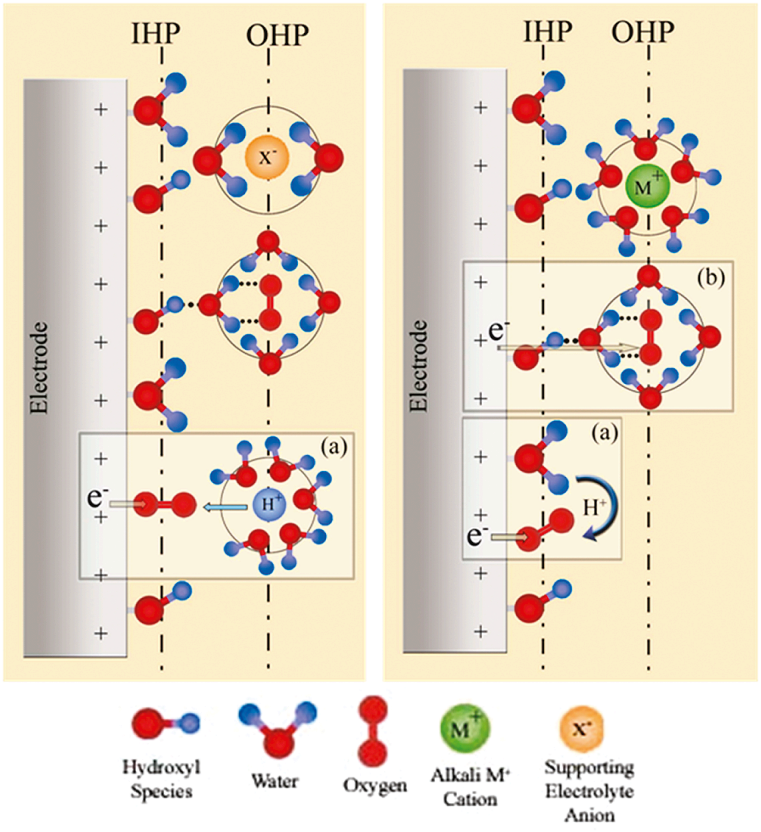

Figure 1.7: Diagram depicting the double-layer structure during ORR in acidic (left) and alkaline (right) conditions. Insets (a) and (b) demonstrate the processes of inner- and outer-sphere electron transfer. Reprinted with permission [77]. Copyright 2011 American Chemical Society.

1.3.3 CN_x Catalysts for ORR

Carbon materials, in their pristine form, are generally inert towards the adsorption and activation of O_2 and its intermediates in the ORR. However, several strategies have been proposed to transform carbon into active electrocatalysts for ORR. These strategies include chemical doping, physical intermolecular charge transfer, and the introduction of structural defects. N-doping is a particularly advantageous method for modifying carbon materials for the ORR. N possesses one additional electron compared to C, making it favorable for electron-transfer reactions like the ORR [80]. N-doped carbon nanotubes (CNTs) with a core of pristine CNTs and N-doped carbon layers as the shell have been successfully synthesized. These N-doped CNTs exhibit a high electrical conductivity of 3.3 $S \cdot cm^{-1}$ in alkaline conditions [81]. The surface's nitrogen atom enrichment, in conjunction with the presence of undamaged inner carbon walls, contributes to significantly enhanced oxygen reduction reaction (ORR) activity compared to regular N-doped CNTs [82-84]. Rao and Ishikawa conducted a study where they prepared metal-free nitrogen-doped carbon nanotubes (N-CNTs) with a nitrogen content of 8 % using a template-assisted pyrolysis method. The synthesized N-CNTs demonstrated comparable ORR activity to Pt/C catalysts, following a 4-electron pathway, and exhibited higher tolerance towards ethanol in alkaline solutions [85]. Lately, a freshly prepared N-doped graphdiyne (GDY) catalyst has demonstrated commendable ORR performance, encompassing favorable peak potential, half-wave potential, and current density. In alkaline conditions, it exhibited performance on par with commercial Pt/C, showcasing accelerated kinetics [86]. While its performance in acidic conditions falls slightly short of Pt/C, it outperforms other metal-free materials. Consequently, the pursuit of efficient metal-free carbon-based catalysts for acidic electrolytes remains crucial, albeit a challenging endeavor. [87-94].

1.4 Outline of Dissertation

Based on the above-mentioned previous studies, more and more metal-free CN_x-based materials have been synthesized and applied to become catalysts in the energy conversion field (CO_2RR, N_2RR, ORR, and so on). Efficient catalyst design still requires in-depth theoretical research. Theoretical calculations can not only explore the electronic properties and electron transfer mechanisms within materials but also explain the reaction pathways of properties that cannot be explored experimentally, such as HER, CO_2RR, N_2RR, etc. In addition, when experiments cannot determine whether a catalyst can be used for photocatalysis, its properties can be predicted through theoretical calculations. Therefore, theoretical calculations in material design and chemical reaction simulation are becoming increasingly important.

In this thesis, I chose three potential CN_x materials, namely C_3N_5, B-doped g-C_9N_{10}, and N-doped graphdiyne (GDY) to apply for CO_2RR, N_2RR, and ORR, respectively. The research content is divided into three parts in chapters 3-5:

Chapter 3: DFT calculation of CO_2RR on N-rich C_3N_5 was investigated, and the optimal reaction paths were selected based on the thermodynamic energy barrier of the reaction process, providing a new design strategy for designing new and efficient CO_2RR catalysts.

Chapter 4: DFT calculation of N_2RR on different B doping sites on g-C_9N_{10} was investigated. Electronic structures and optical properties of these structures were also performed, and the optimal reaction paths and suitable catalysts were selected based on the thermodynamic energy of the reaction process.

Chapter 5: I systematically studied the ORR mechanism on sp-N1GDY and Pyri-NGDY support by graphene (G) with solvation effect which is performed by using density functional theory (DFT) as well as *ab initio* molecular dynamics (AIMD) simulations.

References

[1] M. Shao, Q. Chang, J. P. Dodelet, R. Chenitz, Chem. Rev., **116**, 3594 (2016).

[2] Y. P. Zhu, C. Guo, Y. Zheng, S. Z. Qiao, Acc. Chem. Res., **50**, 915 (2017).

[3] X. Liu, L. Dai, Nat. Rev. Mater., **1**, 16064 (2016).

[4] L. Dai, Y. Xue, L. Qu, H. J. Choi, J. B. Baek, Chem. Rev., **115**, 4823-4892 (2015)

[5] K. Gong, F. Du, Z. Xia, M. Durstock, L. Dai, Science, **323**, 760-764 (2009).

[6] D. R. Miller, J. R. Holst, E. G. Gillan,. Inorg. Chem., **46**, 2767-2774 (2007).

[7] S. Wang, D. Yu, L. Dai, J. Am. Chem. Soc., **133**, 5182-5185 (2011).

[8] D. Yu, L. Wei, W. Jiang, H. Wang, B. Sun, Q. Zhang, K. Goh, R. Si, Y. Chen, Nanoscale, **5**, 3457-3464 (2013).

[9] S. Chen, J. Duan, M. Jaroniec, S. Z. Qiao, Adv. Mater., **26**, 2925-2930 (2014).

[10] D. W. Zheng, B. Li, C. X. Li, J. X. Fan, Q. Lei, C. Li, Z. Xu, X. Z. Zhang, ACS nano, **10**, 8715-8722 (2016).

[11] M. A. Ghausi, J. Xie, Q. Li, X. Wang, R. Yang, M. Wu, Y. Wang, L. Dai, Angew. Chem. Int. Ed., **57**, 13135-13139 (2018).

[12] Z. Liu, M. Zhang, H. Wang, D. Cang, X. Ji, B. Liu, W. Yang, D. Li, J. Liu, ACS Sustain. Chem. Eng., **8**, 5278-5286 (2020).

[13] F. T. Kong, X. Z. Cui, Y. F. Huang, H. L. Yao, Y. F. Chen, H. Tian, G. Meng, C. Chen, Z. W. Chang, J. L. Shi, Angew. Chem. Int. Ed., **61**, e202116290 (2022).

[14] C. J. Nielsen, H. Herrmann, C. Weller, Chem. Soc. Rev., **41**, 6684-704 (2012).

[15] W. Tu, Y. Zhou, Z. Zou, Adv. Mater., **26**, 4607-4626 (2014).

[16] C. Costentin, M. Robert, J. M. Savéant, Chem. Soc. Rev., **42**, 2423-36 (2013).

[17] Qiao J, Liu Y, Hong F, J. Zhang, Chem Soc Rev., **43**, 631-675 (2014).

[18] K. Iizuka, T. Wato, Y. Miseki, K. Saito, A. Kudo, J Am Chem Soc, **133**, 20863-20868 (2011).

[19] J. Lee, D. C. Sorescu, X. Y. Deng, J. Am. Chem. Soc., **133**, 10066-10069 (2011).

[20] B. A. Rosen, A. Salehi-Khojin, M. R. Thorson, W. Zhu, D.T. Whipple, P. J. Kenis, R. I. Masel, Science, **334**, 643-644 (2011).

[21] H. He, P. Zapol, L. A. Curtiss, J. Phys. Chem. C., **114**, 21474-21481 (2010).

[22] C. J. Wang, R. L. Thompson, Baltrus J, C. Matranga, J. Phys. Chem. Lett., **1**, 48-53 (2010).

[23] E. E. Barton, D. M. Rampulla, A. B. Bocarsly, J. Am. Chem. Soc., **130**, 6342-6344 (2008).

[24] T. Inoue, A. Fujishima, S. Konishi, K. Honda, Nature, **277**, 637-638 (1979).

[25] J. Wu, Y. Huang, W. Ye, Y. Li, Adv. Sci., **4**, 1700194 (2017).

[26] X. Li, J. Wen, J. Low, Y. Fang, J. Yu, Sci. China Mater., **57**, 70 (2014).

[27] J. P. Jones, G K S. Prakash, G A. Olah, J. Isr, Chem., **54**, 1451-66 (2014).

[28] W. Zhang, Y. Hu, L. Ma, G. Zhu, Y. Wang, X. Xue, R. Chen, S. Yang, Z. Jin, Adv. Sci, **5**, 1700275 (2018).

[29] J. K. Nørskov, J. Rossmeisl, A. Logadottir, L. Lindqvist, J. R. Kitchin, T. Bligaard, H. Jónsson, J. Phys. Chem. B, **108**, 17886-17892 (2004).

[30] Z. W. Seh, J. Kibsgaard, C. F. Dickens, I. Chorkendorff, J. K. Nørskov, T. F. Jaramillo, Science, **355**, 6321 (2017).

[31] A. A. Peterson, J. K. Nørskov, J. Phys. Chem. Lett., **3**, 251-258 (2012).

[32] J. B. Varley, Y. Wang, K. Chan, F. Studt, J. K. Nørskov, Phys. Chem. Chem. Phys., **17**, 29541-29547 (2015).

[33] D. H. Park, K. S. Lakhi, K. Ramadass, M. K. Kim, S. N. Talapaneni, S. Joseph, U. Ravon, K. A. Bahily, A. Vinu, Chem. Eur. J., **23**, 10753-10757 (2017).

[34] G. Dong, L. Zhang, J. Mater. Chem., **22**, 1160-1166 (2012).

[35] J. Mao, T. Peng, X. Zhang, K. Li, L, Ye, L. Zan, Catal. Sci. Technol., **3**, 1253-1260 (2015).

[36] M. Shen, L. Zhang, M. Wang, J. Tian, X. Jin, L. Guo, L. Wang, J. Shi, J. Mater. Chem. A, **7**, 1556-1563 (2019).

[37] P. Garrido-Barros, J. Derosa, M. J. Chalkley, P. C. Jonas, Nature, **609**, 71-76 (2022).

[38] V. Rosca, M. Duca, M. T. de Groot, M. T. M. Koper, Chem. Rev., **109**, 2209 (2009).

[39] S. Zhao, D. W. Wang, R. Amal, L. Dai, Adv. Mater., **31**, 1801526 (2019).

[40] M. Kitano, Y. Inoue, Y. Yamazaki, F. Hayashi, S. Kanbara, S. Matsuishi, T. Yokoyama, S.-W. Kim, M. Hara, H. Hosono, Nat. Chem., **4**, 934 (2012).

[41] M. M. Shi, D. Bao, B. R. Wulan, Y. H. Li, Y. F. Zhang, J. M. Yan, Q. Jiang, Adv. Mater., **29**, 1606550 (2017).

[42] G. Zhang, Y. Li, C. He, X. Ren, P. Zhang, H. Mi, Adv. Energy Mater., **11**, 2003294 (2021).

[43] G. Chen, S. Ren, L. Zhang, H. Cheng, Y. Luo, K. Zhu, L. Ding, H. Wang, Small Methods, **3**, 1800337 (2019).

[44] B. Ma, H. Zhao, T. Li, Q. Liu, Y. Luo, C. Li, S. Lu, A. M. Asiri, D. Ma, X. Sun, Nano Res., **14**, 555-569 (2021).

[45] L. L. Zhang, G. F. Chen, L. X. Ding, H. H. Wang, Chem. Eur. J., **25**, 12464-12485 (2019).

[46] Y. C. Wan, J. C. Xu, R. T. Lv, Mater. Today, **27**, 69-90 (2019).

[47] X. F. Li, Q. K. Li, J. Cheng, L. L. Liu, Q. Yan, Y. C. Wu, X. H. Zhang, Z. Y. Wang, Q. Qiu, Y. Luo, J. Am. Chem. Soc., **138**, 8706-8709 (2016).

[48] X. Y. Cui, C. Tang, Q. Zhang, Adv. Energy Mater., **8**, 1800369 (2018).

[49] C. Y. Ling, X. W. Bai, Y. X. Ouyang, A. J. Du, J. L. Wang, J. Phys. Chem. C, **122**, 16842-16847 (2018).

[50] T. Xu, J. Liang, S. Li, Z. Xu, L. Yue, T. Li, Y. Luo, Q. Liu, X. Shi, A. M. Asiri, C. Yang, X. Sun, Small Sci., **1**, 2000069 (2021).

[51] G. Dong, W. Ho, C. Wang, J. Mater. Chem. A, **3**, 23435-23441 (2015).

[52] G. N. Schrauzer, T. D. Guth, J. Am. Chem. Soc., **99**, 7189-7193 (1977).

[53] Y. Liu, Y. Su, X. Quan, X. Fan, S. Chen, H. Yu, J. Zhao, ACS Catal., **8**, 1186-1191 (2018).

[54] B. Liu, Y. Zheng, H. Peng, B. Ji, Y. Yang, Y, Tang, C. Lee, W. Zhang, ACS Energy Lett., **5**, 2590-2596 (2020).

[55] L. H. Zhang, F. Yu, N. R. Shiju, ACS Sustainable Chem. Eng., **9**, 7687-7703 (2021).

[56] C. Ling, X. Niu, Q. Li, A. Du, J. Wang, J. Am. Chem. Soc., **140**, 14161-14168 (2018).

[57] B. Chang, L. Lili, D. Shi, H. Jiang, Z. Ai, S. Wang, Y. Shao, J. Shen, Y. Wu, Y. Li, X. Hao, Appl. Catal. B, **283**, 119622 (2021).

[58] H. Chen, Z. Song, X. Zhao, T. Zhang, P. Pei, C. Liang, Appl. Energy, **224**, 289-299 (2018).

[59] G. Wang, Y. Yu, H. Liu, C. Gong, S. Wen, X. Wang, Z. Tu, Fuel Process. Technol., **179**, 203-228 (2018).

[60] K. Priya, K. Sathishkumar, N. Rajasekar, Renew. Sust. Energy Rev., **93**, 121-144 (2018).

[61] Z. Jiang, J. Yu, T. Huang, M. Sun, Polymers, **10**, 1397 (2018).

[62] Y. Nie, L. Li, Z. Wei, Chem. Soc. Rev., **44**, 2168-2201 (2015).

[63] G. Wu, J. Wang, W. Ding, Y. Nie, L. Li, X. Qi, S. Chen, Z. Wei, Angew. Chem. Int. Ed., **55**, 1340-1344 (2016).

[64] Y. Wang, J. Li, Z. Wei, ChemElectroChem, **5**, 1764-1774 (2018).

[65] M. Song, Y. Song, W. Sha, B. Xu, J. Guo, Y. Wu, Catalysts, **10**, 141 (2020).

[66] C. Song, J. Zhang, PEM fuel cell electrocatalysts and catalyst layers: fundamentals and applications, London: Springer London, 89-134 (2008).

[67] W. Niu, S. Pakhira, K. Marcus, Z. Li, J. L. Mendoza-Cortes, Y. Yang, Adv. Energy Mater., **8**, 1800480 (2018).

[68] G. Wu, P. Zelenay. Acc. Chem. Res., **46**, 1878-1889 (2013).

[69] X. Zhou, J. Qiao, L. Yang, J. Zhang, Adv. Energy Mater., **4**, 1301523 (2014).

[70] M. Klingele, P. Van, A. Fischer, S. Thiele, Fuel Cells, **16**, 522-529 (2016).

[71] J. Masa, A. Zhao, W. Xia, M. Muhler, W. Schuhmann, Electrochim. Acta, **128**, 271-278 (2014).

[72] T. Sun, J. Wang, C. Qiu, X. Ling, B. Tian, W. Chen, C. Su, Adv. Sci., **5**, 1800036 (2018).

[73] F. An, X. Q. Bao, X. Y. Deng, Z. Z. Ma, X. G. Wang, New Carbon Mater., **37**, 338-354 (2022).

[74] A. J. Bard, J. Am. Chem. Soc., **132**, 7559-7567 (2010).

[75] A. J. Appleby, Compr. Treatise Electrochem., **7**, 173 (1983).

[76] J. O. Bockris, J. Appleby, S. S., Ed. Penner, Pergamon Press: Oxford, U.K., **11**, 95 (1986).

[77] N. Ramaswamy, S. Mukerjee, J. Phys. Chem. C, **115**, 18015-18026 (2011).

[78] X. Ge, A. Sumboja, D. Wuu, T. An, B. Li, F. T. Goh, Z. Liu, ACS Catal., **5**, 4643-4667 (2015).

[79] C. H. Choi, H. K. Lim, M. W. Chung, J. C. Park, H. Shin, H. Kim, S. I. Woo, J. Am. Chem. Soc., **136**, 9070-9077 (2014).

[80] L. Yang, J. Shui, L. Du, Y. Shao, J. Liu, L. Dai, Z. Hu, Adv. Mater., **31**, 1804799 (2019).

[81] K. Wan, Z. Yu, X. Li, M. Liu, G. Yang, J. Piao, Z. Liang, ACS Catal., **5**, 4325 (2015).

[82] G. Tian, Q. Zhang, B. Zhang, Y. Jin, J. Huang, D. S. Su, F. Wei, Adv. Funct. Mater., **24**, 5956 (2014).

[83] C. Xiao, X. Chen, Z. Fan, J. Liang, B. Zhang, S. Ding, Nanotechnology, **27**, 445402 (2016).

[84] X. Zhao, S. Li, H. Cheng, J. Schmidt, A. Thomas, ACS Appl. Mater. Interfaces, **10**, 3912 (2018).

[85] C. V. Rao, Y. Ishikawa, J. Phys. Chem. C, **116**, 4340-4346 (2012).

[86] Q. Lv, W. Si, Z. Yang, N. Wang, Z. Tu, Y. Yi, C. Huang, L. Jiang, M. Zhang, J. He, Y. Long, ACS Appl. Mater. Interfaces, **9**, 29744-29752 (2017).

[87] J. Shui, M. Wang, F. Du, L. Dai, Sci. Adv., **1**, e1400129 (2015).

[88] D. Yu, Q. Zhang, L. Dai, J. Am. Chem. Soc., **132**, 15127-15129 (2010).

[89] Z. Xiang, Y. Xue, D. Cao, L. Huang, J. F. Chen, L. Dai, Angew. Chem. Int. Ed., **53**, 2433-2437 (2014).

[90] S. Kundu, T. C. Nagaiah, W. Xia, Y. Wang, S. V. Dommele, J. H. Bitter, M. Santa, G. Grundmeier, M. Bron, W. Schuhmann, M. Muhler, J. Phys. Chem. C, **113**, 14302-14310 (2009).

[91] X.Q. Wang, J.S. Lee, Q. Zhu, J. Liu, Y. Wang, S. Dai, Chem. Mater., **22**, 2178-2180 (2010).

[92] Y.G. Li, W. Zhou, H.L. Wang, L. Xie, Y. Liang, F. Wei, J. C. Idrobo, S. J. Pennycook, H. Dai, Nat. Nanotechnol., **7**, 394-400 (2012).

[93] Q. Q. Shi, F. Peng, S. X. Liao, H. Wang, H. Yu, Z. Liu, B. Zhang, D. Su, J. Mater. Chem. A, **1**, 14853-14857 (2013).

[94] C. Hu, Y. Xiao, Y. Zou, L. Dai, Electrochem. Energy Rev., **1**, 84-112 (2018).

Chapter 2

Methods

The development of quantum mechanics allowed for the exploration of the micro world (Figure 2.1). The established quantum chemistry calculation model, on this basis, improves the combination of computational science and experiment. Computational simulation is now being used in a growing number of experiments to explain experimental phenomena and reaction mechanisms. Furthermore, the calculation and simulation can predict the reaction and provide theoretical guidance for new material design.

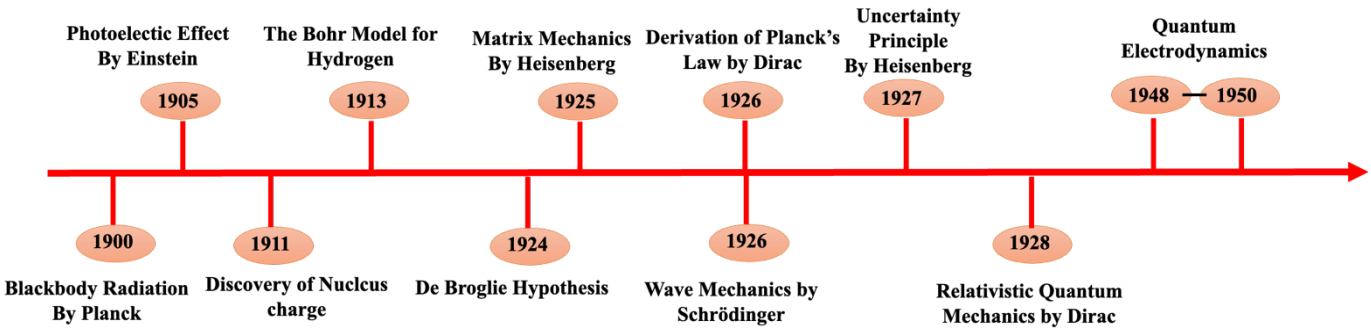

Figure 2.1: The development of quantum mechanics.

2.1 Schrödinger Equation

The core principle in quantum mechanics, known as the Born hypothesis, states that the state of a microparticle can consistently be described by an associated wave function $\psi(r,t)$. To understand the behavior of the particle, Schrödinger proposed the Schrödinger wave dynamics equation (i.e. Schrödinger equation) to solve this problem. the time-independent Schrödinger equation is [1]:

$$\hat{\mathrm{H}}\psi(r,t) = i\hbar\frac{\partial}{\partial t}\psi(r,t) = -\frac{\hbar^2}{2m}\frac{\partial^2\psi(r,t)}{\partial r^2} + V(r,t)\psi(r,t) \tag{2-1}$$

where $\hat{H}$ is a Hamiltonian operator that represents the system's total energy. The Hamiltonian operator is denoted as:$\hat{H} = -\frac{\hbar^2}{2m}\nabla^2 + V(r)$, ∇^2 is called the Laplace operator; $\hbar = \frac{h}{2\pi}$, h is Planck constant. $V(r,t)$ the wave function can be written as:

$$\psi(r,t) = f(t)\psi(r) \tag{2-2}$$

Substituting Eq. (2-2) into Eq. (2-1):

$$i\hbar\frac{\partial f(t)}{\partial t}\psi(r) = -\frac{\hbar^2}{2m}f(t)\frac{\partial^2\psi(r)}{\partial r^2} + V(r)\psi(r)f(t) \tag{2-3}$$

Shift, variable separation and final get:

$$\hat{H}\psi = E\psi \tag{2-4}$$

E is the eigenvalue of the energy operator.

2.2 Density Function Theory

Density functional theory (DFT) is a theory that expresses energy using electron density [2]. Instead of solving the complex many-electron Schrödinger equation directly, DFT aims to find the ground-state electronic density of a system that minimizes the total energy. This approach simplifies the calculations while still providing accurate predictions of properties. DFT is widely used in physics and chemistry, particularly in the study of molecule and condensed matter properties. It is a widely used method in condensed matter physics and computational chemistry.

2.2.1 Hohenberg-Kohn Theorems

In 1964, P. Hohenberg and W. Kohn [3] showed that the density of particles in the ground state of a quantum many-body system carries particular significance. This density can be regarded as a fundamental parameter, meaning that all system properties can be expressed as specific functionals of the ground state density. DFT was formulated by Hohenberg and Kohn

as a comprehensive theory for many-body systems comprising interacting particles subject to an external potential, denoted as $V_{ext}(\vec{r})$.

Theorem 1: In the case of any system of interacting particles subject to an external potentia$V_{ext}(\vec{r})$, the ground state particle density $\rho_0(\vec{r})$ uniquely determines the potential $V_{ext}(\vec{r})$, except for an additive constant.

Theorem 2: A universal energy functional, denoted as $E[n]$ and dependent on the density $\rho(\vec{r})$, can be formulated to apply to any external potential $V_{ext}(\vec{r})$. The exact ground state energy of the system corresponds to the minimum value of this functional for any given $V_{ext}(\vec{r})$. The density $\rho(\vec{r})$ that minimizes the functional represents the precise ground state density $\rho_0(\vec{r})$.

2.2.2 Kohn-Sham Equation

Although the Hohenberg-Kohn theorem provides the theoretical foundation for DFT, it does not specify the type of functional or propose a practical method for calculating the properties of ground states using electron density [4]. Kohn and Sham then proposed the Kohn-Sham approach. The Kohn-Sham equation is shown as:

$$\left(-\frac{1}{2}\nabla^2 + V_{\text{eff}}(\vec{r})\right)\Psi_i(\vec{r}) = \varepsilon_i\Psi_i(\vec{r}) \tag{2-5}$$

where $\mathrm{V_{eff}}$ is effective potential, $V_{\text{eff}} = V_{\text{c}} + V_{\text{Ne}} + V_{\text{xc}}$; $\mathrm{V_c}$ is called Coulomb potential; $\mathrm{V_{Ne}}$ represents the attractive potential of electrons in atomic nuclei. V_{xc} is exchange-correlation potential, $V_{\text{xc}} = \frac{\partial E_{\text{xc}}}{\partial \rho}$. It is noted that all ground state properties of multiparticle systems are density functional, the total energy of the system can be expressed as:

$$E[\rho] = T[\rho] + U[\rho] + E_{\text{xc}}[\rho] \tag{2-6}$$

where $T[\rho]$ is the kinetic energy of particles without interaction, $U[\rho]$ is the general Coulomb force, which is the knowable term that can be accurately obtained, and $E_{\text{xc}}[\rho]$ is the exchange-correlation energy. So, getting the exchange-correlation energy can know the exchange-

correlation potential. The self-consistent field iterative method is used to solve this process, and the solution flow chart as shown in Figure 2.2.

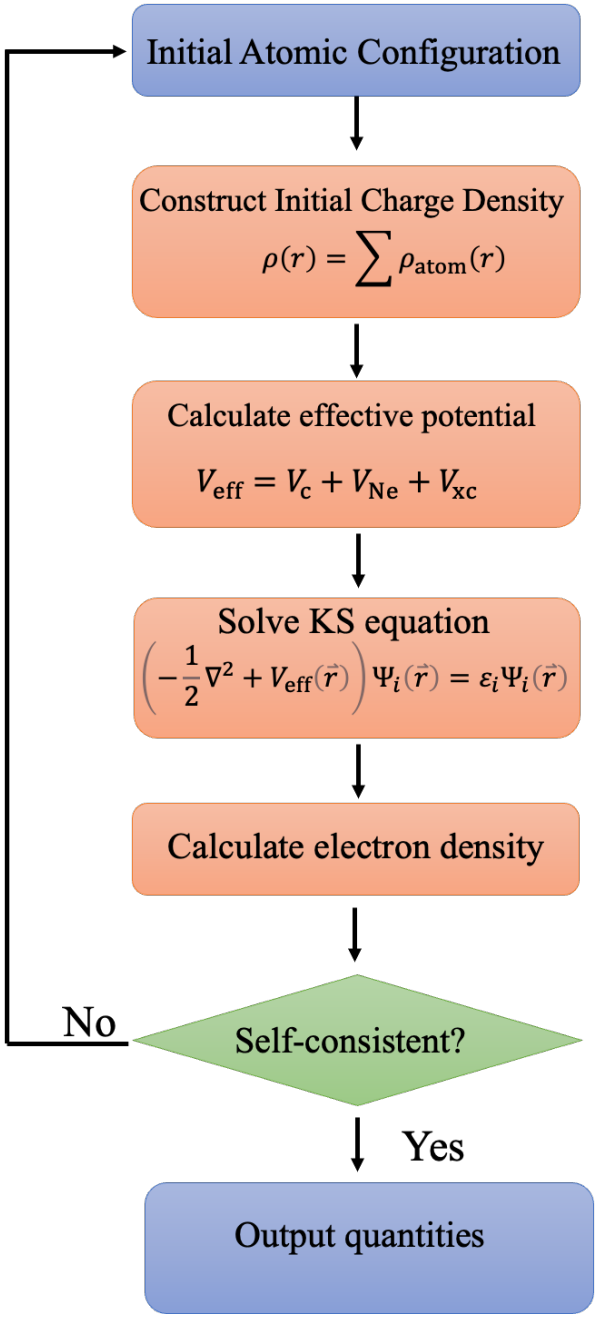

Figure 2.2: Flow chart of a general self-consistent field cycle for the solution of the Kohn-Sham equation.

2.2.3 Exchange-Correlation Functional

Although the Kohn-sham equation solves the problems of particle density $\rho(\vec{r})$ and kinetic energy functional $T[\rho]$, to apply the Kohn-sham method to the actual calculation, the exchange-correlation energy $E_{xc}[\rho]$ must be determined. As a result, whether the calculation result of a multi-system problem is accurate is determined by a reasonable approximate expression of the exchange-correlation functional. Although no exact solution has been discovered, many approximation methods have been proposed. Currently, the most commonly used exchange-correlation functionals are the local density approximation (LDA) [4] and the generalized gradient density approximation (GGA) [5-7].

2.2.3.1 Local Density Approximation

Kohn and Sham proposed the LDA approximate density functional in 1965. It is the earliest, most basic, and simplest approximate exchange-correlation function. If the electron density varies little with distance, the uniform electron gas exchange-correlation density can be used instead of the non-uniform electron gas exchange-correlation density. Although LDA has had great success, it has many drawbacks, such as the system's binding energy being easily overestimated, the reaction activation energy being underestimated, the lattice bond length, the band gap, and so on.

2.2.3.2 Generalized Gradient Approximation

To reduce the error caused by the uneven distribution of electron density, it is considered that the exchange-correlation energy $E_{\mathrm{xc}}[\rho]$ is not only related to electron density but also related to electron density gradient. Therefore, based on LDA, the correlation of electron density gradient is introduced, and the GGA functional is proposed, the equation is:

$$E_{\mathrm{XC}}^{\mathrm{GGA}} = \int f\left(\rho_{\alpha}, \rho_{\beta,} \nabla\rho_{\alpha}, \nabla\rho_{\beta}\right) d\vec{r} \tag{2-7}$$

where $\rho_{\alpha}, \rho_{\beta}$ expresses as spin density, $\nabla\rho_{\alpha}, \nabla\rho_{\beta}$ represents the spin density gradient.

GGA has the advantage of more precise atomic and molecular energy and reaction activation energy when compared to LDA. It is primarily employed in solid calculations. Because the findings computed with the GGA functional are compatible with the experimental data, many theoretical computations now use the GGA functional. Many approximation forms based on GGA have been developed as computing technology has progressed, including Perdew Wang 91 (PW91), suggested by Perdew and Wang in 1991 [8]; Perdew Burke ernzerhof (PBE) [7], which is also one of the most often used functional.

Revised Perdew-Burke-Ernzerhof (RPBE) [9] is an extension of the PBE functional designed to address the shortcomings related to dispersion forces. RPBE includes a dispersion correction that improves its treatment of van der Waals interactions. This correction accounts for the attractive forces between atoms and molecules that arise from temporary fluctuations in electron distribution.

2.2.3.3 Heyd-Scuseria-Ernzerhof (HSE) Exchange-Correlation Functional

Hybrid functionals, in the context of density functional theory (DFT), merge a portion of the exact exchange from Hartree-Fock theory with the remaining exchange-correlation derived from other references. A common approach involves blending the Hartree-Fock exact exchange functional with a hybrid exchange-correlation functional through a linear combination:

$$E_{\mathrm{X}}^{\mathrm{HF}} = -\frac{1}{2}\sum_{i,j}\iint \psi_i^*(r_1)\psi_j^*(r_2)\frac{1}{r_{12}}\psi_{j(r_1)}\psi_{i(r_2)}dr_1dr_2 \tag{2-8}$$

The HSE exchange-correlation functional [10-11] employs an error-function-screened Coulomb potential to compute the exchange component of the energy, enhancing computational efficiency, the equation is:

$$E_{\mathrm{xc}}^{\omega\mathrm{PBEhybrid}} = aE_{\mathrm{x}}^{\mathrm{HF,SR}}(\omega) + (1-a)E_{\mathrm{x}}^{\mathrm{PBE,SR}}(\omega) + E_{\mathrm{x}}^{\mathrm{PBE,LR}}(\omega) + E_{\mathrm{c}}^{\mathrm{PBE}}(\omega) \tag{2-9}$$

where, a represents the mixing parameter, and ω is a tunable parameter that governs the short-range nature of the interaction. When the values of a = 0.25 and ω = 0.2 are applied, it is referred to as the HES06 functional, which is always used to calculate the band structure of semiconductors and give good results with experiment values. $E_{\mathrm{x}}^{\mathrm{HF,SR}}(\omega)$ is the short-range Hartree-Fock exact exchange functional, $E_{\mathrm{x}}^{\mathrm{PBE,SR}}(\omega)$ and $E_{\mathrm{x}}^{\mathrm{PBE,LR}}(\omega)$ represent the short-range and long-range components of the PBE exchange functional and $E_{\mathrm{c}}^{\mathrm{PBE}}(\omega)$ is the PBE correlation functional.

2.3 *Ab Initio* Molecular Dynamics (AIMD)

In the previous section, we focused on the ground-state electrical characteristics of the static external potential produced by the nuclei, assuming that they are fixed. More complex techniques are required if nuclear movements need to be considered, such as when examining the effects of finite temperatures. A successful strategy involves combining DFT electronic structure computations with molecular dynamics simulations, often known as *ab initio* molecular dynamics (AIMD) or first principles molecular dynamics. In 1985, AIMD simulations were pioneered by Car and Parrinello [12]. These simulations are based on the fundamental premise that the forces acting on the nuclei may be calculated from electronic structure calculations carried out "on the fly" as the molecular dynamics trajectory is being formed. AIMD enables the objective and accurate study of chemical processes in condensed phases, ushering in new paradigms for understanding microscopic mechanisms, validating experimental findings, and generating testable predictions for novel phenomena. In comparison to classical molecular dynamics (MD), AIMD offers several advantages: 1) It directly calculates the potential energy surface from the Schrödinger equation; 2) AIMD can describe bond breaking and making during simulations; 3) it also can calculate the electronic properties. The Car-Parrinello molecular dynamics (CPMD) method [13], which uses a single algorithm

to handle both electrons and ions, became prominent in the era of AIMD. A few years later, the conceptually simpler Born-Oppenheimer molecular dynamics (BOMD) method [14] also gained popularity.

2.3.1 Born-Oppenheimer MD Method (BOMD)

The Hamiltonian for both the fixed nuclei $\{R_I\}$ and electrons $\{r_i\}$ can also be formulated as follows: [14]:

$$\hat{\mathrm{H}} = -\frac{\hbar^2}{2M_I}\sum_I \nabla_I^2 + \hat{\mathrm{H}}_e(\{r_i\};\{R_I\}) \tag{2-10}$$

where, $\hat{\mathrm{H}}_e$ is expected to represent the Hamiltonian of the electronic system. Subsequently, the precise solution to the corresponding time-independent electronic Schrödinger equation is given as follows:

$$\hat{\mathrm{H}}_e(\{r_i\};\{R_I\})\Psi_k = E_k(\{R_I\})\Psi_k(\{r_i\};\{R_I\}) \tag{2-11}$$

Next, the total wave function for the time-dependent Schrödinger equation can be expanded as follows:

$$\Phi(\{r_i\};\{R_I\};t) = \sum_{l=0}^{\infty}\Psi_l(\{r_i\};\{R_I\})\, x_l(\{R_I\};t) \tag{2-12}$$

here is using a normalized nuclear and electrical wave function. Ψ_l is the eigenfunctions for $\hat{\mathrm{H}}_e$, x_l is the time-dependent expansion coefficients. After being introduced into the time-dependent Schrödinger equation, $\Psi_k(\{r_i\};\{R_I\})$ must be multiplied from the left and integrated across electronic coordinates to produce a set of coupled differential equations:

$$\left[-\sum_I \frac{\hbar^2}{2M_I}\nabla_I^2 + E_k(\{R_I\})\right]x_k + \sum_l C_{kl}x_{kl} = i\hbar\frac{\partial}{\partial t}x_k \tag{2-13}$$

where C_{kl} represents coupling operators, which are dependent on the nuclei's kinetic energy and momenta. In Born-Oppenheimer approximation, it is further assumed that $C_{kl} \approx 0$. Therefore, the equation will be change to:

$$\left[-\sum_I \frac{\hbar^2}{2M_I}\nabla_I^2 + E_k(\{R_I\})\right] x_k = i\hbar\frac{\partial}{\partial t}x_k \tag{2-14}$$

The nuclei are also regarded as classical objects in accordance with Newton's equations. First, it should be rewriting the wave function using amplitude factor A_k and a phase S_k:

$$x_k(\{R_I\};t) = A_k(\{R_I\};t)e^{\frac{iS_k(\{R_I\};t)}{\hbar}} \tag{2-15}$$

Then, applying the following transformation to change the nuclei's momenta:

$$\mathbf{P}_I = \nabla_I S_k \tag{2-16}$$

Finally, the Newtonian equations of motion $\dot{\mathbf{P}}_I = -\nabla_I U_k(\{R_I\})$ can be written as:

$$\frac{dP_I}{dt} = -\nabla_I E_k \tag{2-17}$$

or

$$M_I\ddot{\mathbf{R}}_I(t) = -\nabla_I U_k^{BO}(\{R_I(t)\}) \tag{2-18}$$

It is true independently for any electrical state k, that is decoupled. The nuclei move according to classical mechanics in an effective potential U_k^{BO}, which is determined by the Born-Oppenheimer potential energy surface E_k. Therefore, this method is called as BOMD.

2.3.2 Car-Parrinello MD Method (CPMD)

The CPMD method's core concept can be grasped as a classical-mechanical division between the rapid electronic movements and the sluggish nuclear motions, relying on the distinctions in adiabatic energy scales The following class of Lagrangians was proposed by Car and Parrinello [13]:

$$\mathcal{L}_{CP} = \sum_I \frac{1}{2}M_I\dot{R}_I^2 + \sum_i \mu\langle\dot{\psi}_i|\dot{\psi}_i\rangle - \langle\Psi_0|\hat{\mathrm{H}}_e|\Psi_0\rangle + constraints \tag{2-19}$$

where $\langle\Psi_0|\hat{\mathrm{H}}_e|\Psi_0\rangle$ is the energy of the electronic subsystem, which is certainly a function of $\{R_I\}$ and can be treated as a functional of the wave function Ψ_0 and thus of a set of orbitals $\{\psi_i\}$. The first term plus the second term represent the kinetic energy, the third term is potential

energy, and final term is the orthonormality term. Next, the accompanying Euler-Lagrange equations are used to derive the appropriate Newtonian equations of motion.

$$\frac{d}{dt}\frac{\partial \mathcal{L}}{\partial \dot{R}_I} = \frac{\partial \mathcal{L}}{\partial R_I} \tag{2-20}$$

Finally, it gets following equations of motion:

$$M_I \ddot{\mathbf{R}}_I(t) = -\frac{\partial}{\partial R_I}\langle \Psi_0 | \hat{\mathrm{H}}_e | \Psi_0 \rangle + \frac{\partial}{\partial R_I}\{constraints\} \tag{2-21}$$

$$\mu_i \ddot{\psi}_i(t) = -\frac{\delta}{\delta \psi_i^*}\langle \Psi_0 | \hat{\mathrm{H}}_e | \Psi_0 \rangle + \frac{\delta}{\delta \psi_i^*}\{constraints\} \tag{2-22}$$

where, μ_i refers to the fictitious masses or inertia parameters that are assigned to the degrees of freedom associated with orbitals.

References

[1] E. Schrödinger, Ann. Phys. **385**, 437-490 (1926).

[2] W. Kohn, A. D. Becke, R. G. Parr, J. Phys. Chem., **100**, 12974-12980 (1996).

[3] P. Hohenberg and W. Kohn, Phys. Rev., **136**, B864 (1964).

[4] W. Kohn, L. J. Sham, Phys. Rev., **140**, A1133-A1138 (1965).

[5] J. P. Perdew, A. Zunger, Phys. Rev. B, **23**, 5048 (1981).

[6] J. P. Perdew, J. A. Chevary, S. H. Vosko, K. A. Jackson, M. R. Pederson, D. J. Singh, C. Fiolhais, Phys. Rev. B, **46**, 6671 (1992).

[7] J. P. Perdew, K. Burke, M. Ernzerhof, Phys. Rev. Lett., **77**, 3865 (1996).

[8] B. Kieron, J. P. Perdew, Y. Wang. Electronic Density Functional Theory: recent progress and new directions. Boston, MA: Springer US, 81-111(1998).

[9] B. Hammer, L. B. Hansen, J. K. Nørskov, Phys. Rev. B, **59**, 7413 (1999).

[10] J. Heyd, G. E. Scuseria, M. Ernzerhof, J. Chem. Phys., **118**, 8207-8215 (2003).

[11] He J. Heyd, G. E. Scuseria, J. Chem. Phys., **121**, 1187-1192 (2004).

[12] R. Car, M. Parrinello, Phys. Rev. Lett. **55**, 2471 (1985).

[13] J. M. Haile, Molecular Dynamics Simulation: Elementary Methods, Wiley Professional. (1997).

[14] T. D. Kühne, M. Krack, F. R. Mohamed, M. Parrinello, Phys. Rev. Lett., **98**, 066401 (2007).

Chapter 3

Density Functional Theory Study on a Nitrogen-Rich Carbon Nitride Material C_3N_5 as a Photocatalyst for CO_2 Reduction to C1 and C2 Products

3.1 Introduction

The emission of carbon dioxide (CO_2), a greenhouse gas, from the excessive use of fossil fuels can cause severe global warming and environmental pollution. Photocatalytic CO_2 reduction into hydrocarbon fuels is a promising strategy that not only lowers the atmospheric CO_2 level but also provides clean fuels, such as carbon monoxide (CO), formic acid (HCOOH), methane (CH_4), and methanol (CH_3OH), ethanol (CH_3CH_2OH) and ethylene (C_2H_4) to replace the conventional fossil resources. Various metal-based materials (such as Cu [1] Pd [2], Ag [3] Sn [4], and Au [5]) as catalysts for CO_2 reduction reaction (CO_2RR) have been intensively studied. Although these catalysts can convert CO_2 into various chemicals, they still have some challenges as follows [6-7]: (1) their catalytic efficiencies are low due to high overpotential, low stability, and poor selectivity; (2) some catalysts are expensive, thereby increasing the cost. Therefore, searching for highly efficient and low-cost metal-free photocatalysts is extremely demanding.

Carbon nitride materials (CN_x), metal-free catalysts, have attracted more attention because of their unique properties e.g., semi-conductivity, high stability, simplicity of synthesis, etc. Developing nitrogen-rich CN materials becomes an effective strategy for multifunctional properties. Graphitic carbon nitride (g-C_3N_4) with 3:4 C:N stoichiometry is the one of

representative nitrogen-rich CN_x materials, which has been intensively investigated as a promising photocatalyst [8]. Except for the band gap (2.70 eV) [9], the presence of numerous nitrogen-rich sites and ordered defects provide active centers for substrate interaction, which increases catalytic ability [10]. However, like other semiconductors, pure g-C_3N_4 has some internal disadvantages such as carrier recombination. Doping with metal (Co, Cu, Fe) [11-13] or non-metal (S, P, B, O) [14-17] atoms and constructing heterojunctions (g-C_3N_4/SnS_2, [18] g-C_3N_4/$AgPO_4$ [19]) have been utilized to improve photocatalytic ability effectively. After all, there is a limit to improving the photocatalytic properties of g-C_3N_4 by structural modification. In my previous work, I designed $(C_6N_7)_n$, $[C_6N_7(C_2)_{1.5}]_n$, $[C_6N_7(C_4)_{1.5}]_n$ and $[C_6N_7(C_3N_3)]_n$ via C_6N_7 unit of g-C_3N_4 connected with C–C, C–C≡C–C, C–C≡C–C≡C–C and C_3N_3 ring. Density functional theory (DFT) calculations indicated that the band gaps of designed structures decrease, and absorption spectrum edges all red-shift compared with g-C_3N_4 [20]. In 2013, Kroke *et al.* speculated that −N=N− linkage replacing the connecting bridge carbon atoms based on the C_6N_7 motif is an efficient way to increase N atoms content, which the C:N ratio is increased from 3:4 in g-C_3N_4 to 3:5, named as C_3N_5 [21]. Due to the combination of azo chromophores (−N=N−) with aromatic compounds, azo-bridged aromatic compounds are well known for visible light absorption [22]. Recently, Shankar *et al.* have successfully synthesized the C_3N_5-modified carbon nitride framework by thermal deammoniation of 2,5,8-trihydrazino-s-heptazine and proved that C_3N_5 exhibits remarkably photocatalytic activity [23]. The catalytic activity of C_3N_5 for CO_2RR, however, needs to be clarified.

And recently, many studies proposed that the CO_2RR not only can generate the C1 products (such as CO, HCOOH, CH_4, and CH_3OH) but also can generate the multi-carbon products, especially C2 products (such as CH_3CH_2OH and C_2H_4) [24-27]. Yeo *et al.* showed that CuAg composite catalysts enhanced CO_2 reduction selectivity toward C_2H_5OH [24]. Zhao *et al.* reported that boron-doped graphdiyne exhibits high-electrocatalytic activity for the

conversion of CO_2 to C_2H_4 by DFT [25], while a single iron atom supported on graphdiyne. can provide an active site for further coupling with CO to generate C_2H_5OH [26]. Xu *et al.* simulated that FeFe-grafiN_6 and FeCu-grafiN_6 could reduce CO_2 to C1 and C2 products [27]. Based on these studies, I also investigated the possibility of C2 products being generated.

In this work, the CO_2RR mechanism on C_3N_5 is investigated by DFT calculations. It is found that C_3N_5 is a locally stable structure and has a more suitable band gap (2.0 eV) than g-C_3N_4. C_3N_5 can efficiently catalyze CO_2 to CH_4 with a rather low limiting potential of −0.54 V and to CH_3CH_2OH with a rather low limiting potential of −0.61 V driven by solar energy.

3.2 Computational Details

All the geometric optimizations and single-point energy calculations were performed using the DMol^3 code [28,29]. The generalized gradient approximation (GGA) with the Perdew-Burke-Ernzerhof (PBE) exchange-correlation functional [30] was used to describe exchange and correlation effects. To accurately describe weak interactions between species involved in the CO_2RR and catalysts, the PBE + D2 method with the Grimme van der Waals (vdW) correction was employed [31]. The criteria for convergence in energy, force, and displacement are 1.0×10^{-5} Ha, 0.002 Ha/Å, and 0.005Å, respectively. A conductor-like screening model (COSMO) was used to simulate the water solvent environment in the whole process [32]. The vacuum space in the Z direction was set to 15 Å, which is large enough to avoid the interlayer interaction. 4 × 4 × 1 *k*-points were selected for efficient geometry optimizations. The band structure, projected density of states (PDOS) onto the (pseudo-)atomic orbitals, and absorption spectra were simulated using the plane-wave ultrasoft (PWUS) pseudopotential method with kinetic cut-off energies of 500 eV and Heyd-Scuseria-Ernzerhof (HSE06) [33] hybrid functional in the Cambridge Sequential Total Energy Package (CASTEP) [34,35] code. The activation energy barrier was performed by using the climbing image nudged

elastic band (CI-NEB) method [36]. The activation energy (E_a) can be evaluated by the following equation:

$$E_a = E_{TS} - E_{IS} \tag{3-1}$$

where E_{IS} and E_{TS} stand for the DFT calculated total energy of initial and transition state, respectively. The adsorption energies (E_{ads}) were calculated by the following equation [37]:

$$E_{ads} = E_{tot}(\text{A-S}) - [E_{tot}(\text{S}) + E_{tot}(\text{A})] \tag{3-2}$$

where E_{tot}(A-S), E_{tot}(S), E_{tot}(A) are the total energies of adsorbate-substrate (A-S) complex, clean substrate (S), and gas-phase adsorbate (A), respectively. I decompose E_{ads} into interaction energy (E_{int}) and deformation energies (E_{def}), as calculated by following the equation [38]:

$$E_{int}(\text{A-S}) = E_{tot}(\text{A-S}) - [E_{tot}(\text{S-ads}) + E_{tot}(\text{A-ads})] \tag{3-3}$$

$$E_{def}(\text{A}) = E_{tot}(\text{A-ads}) - E_{tot}(\text{A}) \tag{3-4}$$

$$E_{def}(\text{S}) = E_{tot}(\text{S-ads}) - E_{tot}(\text{S}) \tag{3-5}$$

where E_{int}(A-S) is the interaction energy between adsorbate and substrate. E_{tot}(S-ads) and E_{tot}(A-ads) are the total energies of substrate and adsorbate at their adsorption geometry in the A-S complex, respectively. Deformation energy (E_{def}) is defined as the energy necessary to deform the adsorbate and substrate upon adsorption.

The Gibbs free energy change (ΔG) [39,40] was defined as:

$$\Delta G = \Delta E + \Delta E_{ZPE} - T\Delta S + \Delta G_{pH} + \Delta G_U \tag{3-6}$$

where ΔE, ΔE_{ZPE} and ΔS are the total energy difference, the zero-point energy difference and the entropy change between the products and reactants obtained from DFT calculations, respectively. The zero-point energies and total entropies of the gas phase were computed from the vibrational frequencies, and the vibrational frequencies of adsorbed species also were computed to obtain ZPE contribution in the free energy expression. Only vibrational modes of the adsorbates were computed explicitly, while the catalyst sheet was fixed (assuming that vibration contribution to the free energy from the substrate is negligible) [41-43]. T is the

temperature (298.15K). $\Delta G_U = -neU$, where ne is the number of electrons transferred and U is the electrode potential applied. ΔG_{pH} is the free energy correction due to the concentration of H^+. $\Delta G_{pH} = k_B T \times \ln 10 \times pH$, where k_B is the Boltzmann constant, and the value of pH was assumed to be zero for acidic condition. The limiting potential (U_L) of the whole reduction process is determined by the potential-limiting step which has the most positive ΔG (ΔG_{max}) as computed by:

$$U_L = -\Delta G_{max}/e \quad (3\text{-}7)$$

3.3 Results and Discussions

3.3.1 Geometric Structures and *Ab Initio* Molecular Dynamics

Azofra *et al.* [44] suggested corrugated g-C_3N_4 is more stable than planar configuration. In my case, I find the optimized corrugated C_3N_5 (a = b = 14.97 Å, Figure 3.1 (a)) is also more stable than planar configuration (a = b = 15.12 Å, Figure 3.1 (a)). The total energy difference (ΔE) between planar and corrugated reaches 0.24 eV in unit cell. According to the different chemical environment, N atoms are categorized into three N types, namely N_1, N_2 and N_3. N_1 and N_2 represent 2-fold and 3-fold coordinated with two C atoms in C_6N_7-unit, respectively, and N_3 represents N atoms in azo bridges. As shown in Figure 3.1 (b), due to the introduction of −N=N− linkage, the pore size of corrugated C_3N_5 is larger (14.86 Å) than that of corrugated g-C_3N_4 (5.09 Å). The effect of pore size will be discussed in following.

To evaluate the stability of C_3N_5, *ab initio* molecular dynamics (AIMD) simulations for 10 ps were performed. As shown in Figure 3.2, the structure well remains even though the

temperature increases to 500 K. Therefore, it proves that C_3N_5 is at least a locally stable structure.

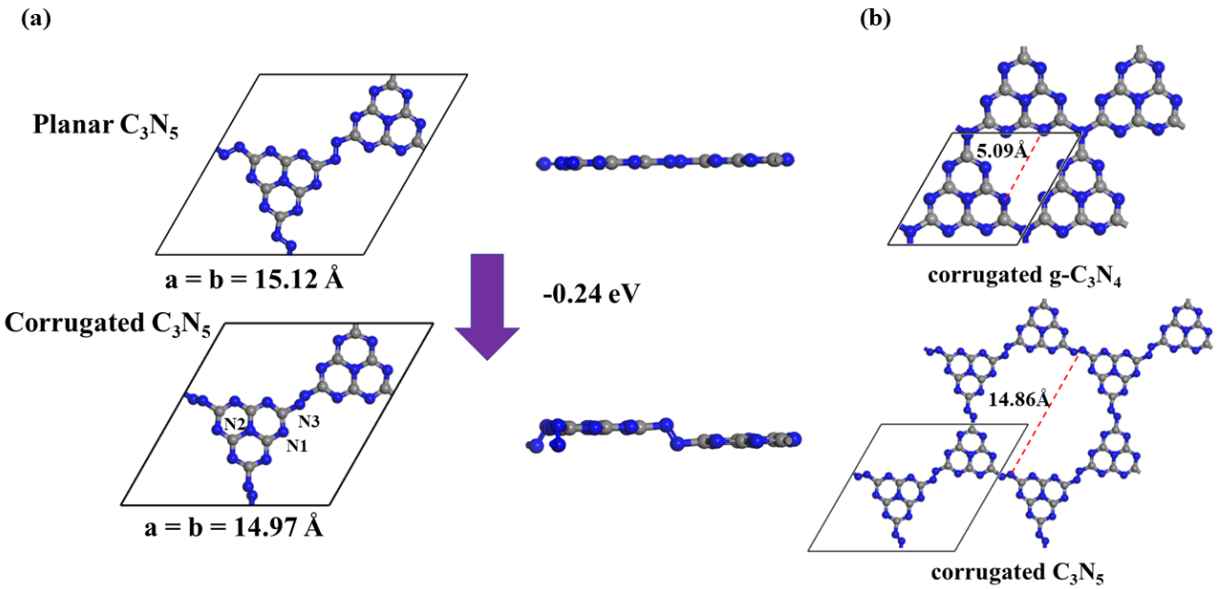

Figure 3.1: (a) Optimized unit cell geometric structures of planar and corrugated C_3N_5, (b) supercell configurations of corrugated g-C_3N_4 and C_3N_5.

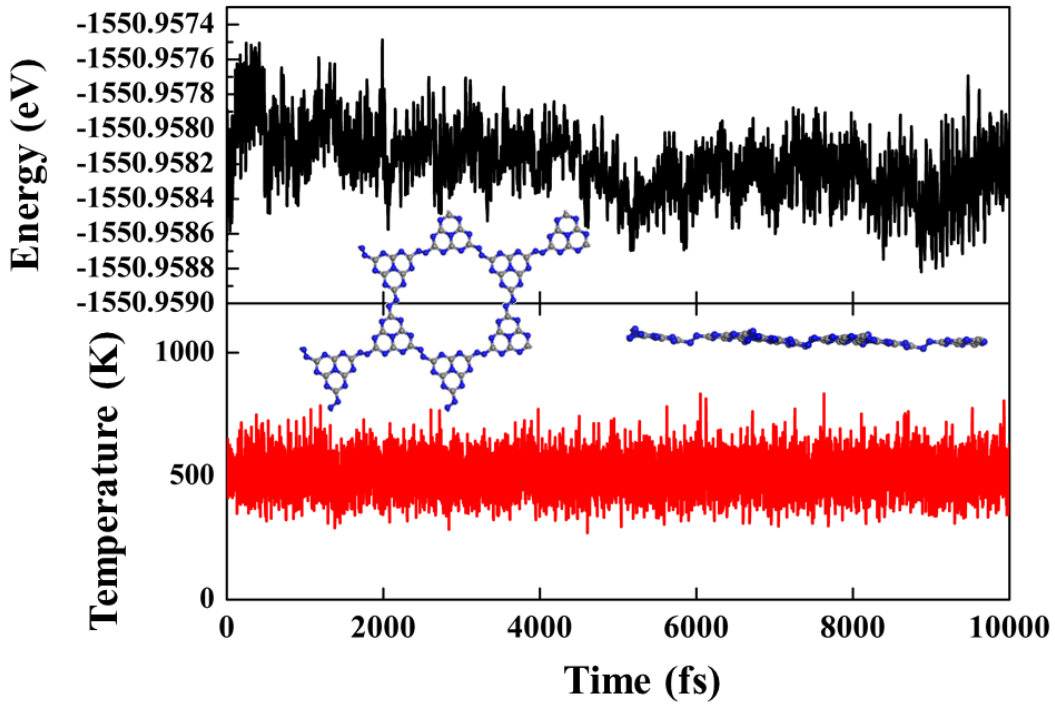

Figure 3.2: Variations of temperature and energy against time for MD simulations of C_3N_5, and the insets show top and side views of the snapshot of atomic configuration. The simulation is performed at 500 K for 10 ps with a time step of 1 fs.

3.3.2 Electronic and Optical Properties

The electronic and optical properties of C_3N_5 were subsequently explored. The band structure and PDOS calculated by using HSE06 are shown in Figure 3.3 (a)-(b). The computed band gap is 2.0 eV, which is close to the experimental one (1.76 eV) [23] and smaller than that of the computed value by HSE06 for g-C_3N_4 (2.81 eV, Figure 3.4 (a)). The PDOS analysis shows that the valence band (VB) and conduction band (CB) are mainly contributed by N_1 and N_3 atoms. The highest occupied crystal orbital (HOCO) and the lowest unoccupied crystal orbital (LUMO) of C_3N_5 plotted in Figure 3.3 (c) mainly distribute on N atoms, especially on −N=N− linkage. Compared with the HOCO and LUCO of g-C_3N_4 (Figure 3.4 (b)), they are spatially separated in C_3N_5, namely, HOCO is mostly located at the heptazine ring, while LUCO is mostly located at −N=N− linkage, thus I expect that C_3N_5 has a better ability to separate the photogenerated e^-/h^+ pairs and higher photocatalytic efficiency than g-C_3N_4. As shown in Figure 3.3 (d), C_3N_5 has a strong absorption peak near 440 nm and the wavelength of the optical absorption edge (λ_{edge}) is 660 nm, which is in good agreement with the experimental result [23]. Compared to g-C_3N_4 (Figure 3.4 (c)), the strong absorption peak and λ_{edge} of C_3N_5 red-shifts by 90 nm and 110 nm, respectively. Moreover, C_3N_5 has a bigger overlap area with visible light (about 400-780 nm) than that of g-C_3N_4. Therefore, the introduction of −N=N− linkage extends π conjugated network, which can decrease the band gap and improve the light response range [23].

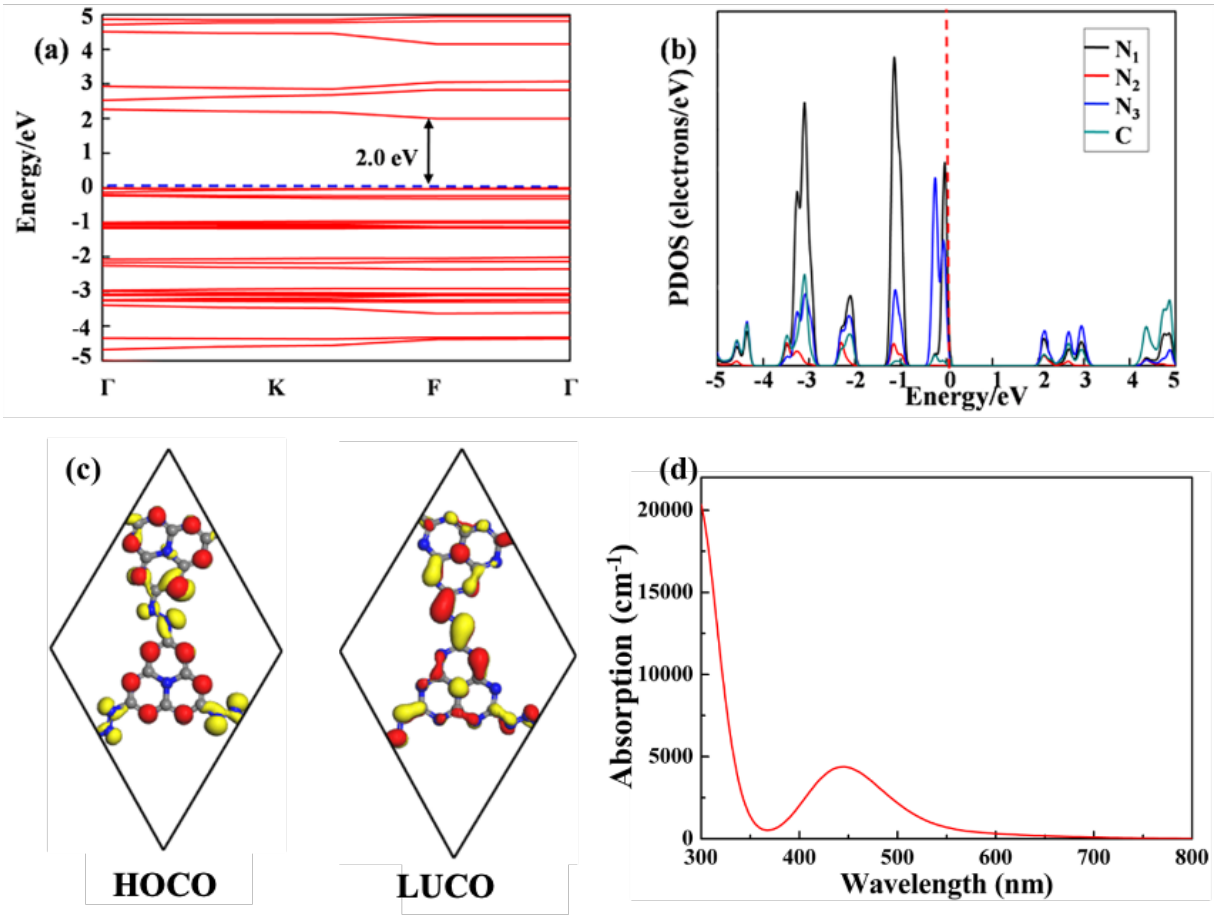

Figure 3.3: (a) Band structure, (b) Projected density of states (PDOS) onto the (pseudo-)atomic orbitals, (c) HOCO and LUCO distributions, and (d) absorption spectra of C_3N_5. The red and yellow isosurfaces represent positive and negative values of the wave function, respectively.

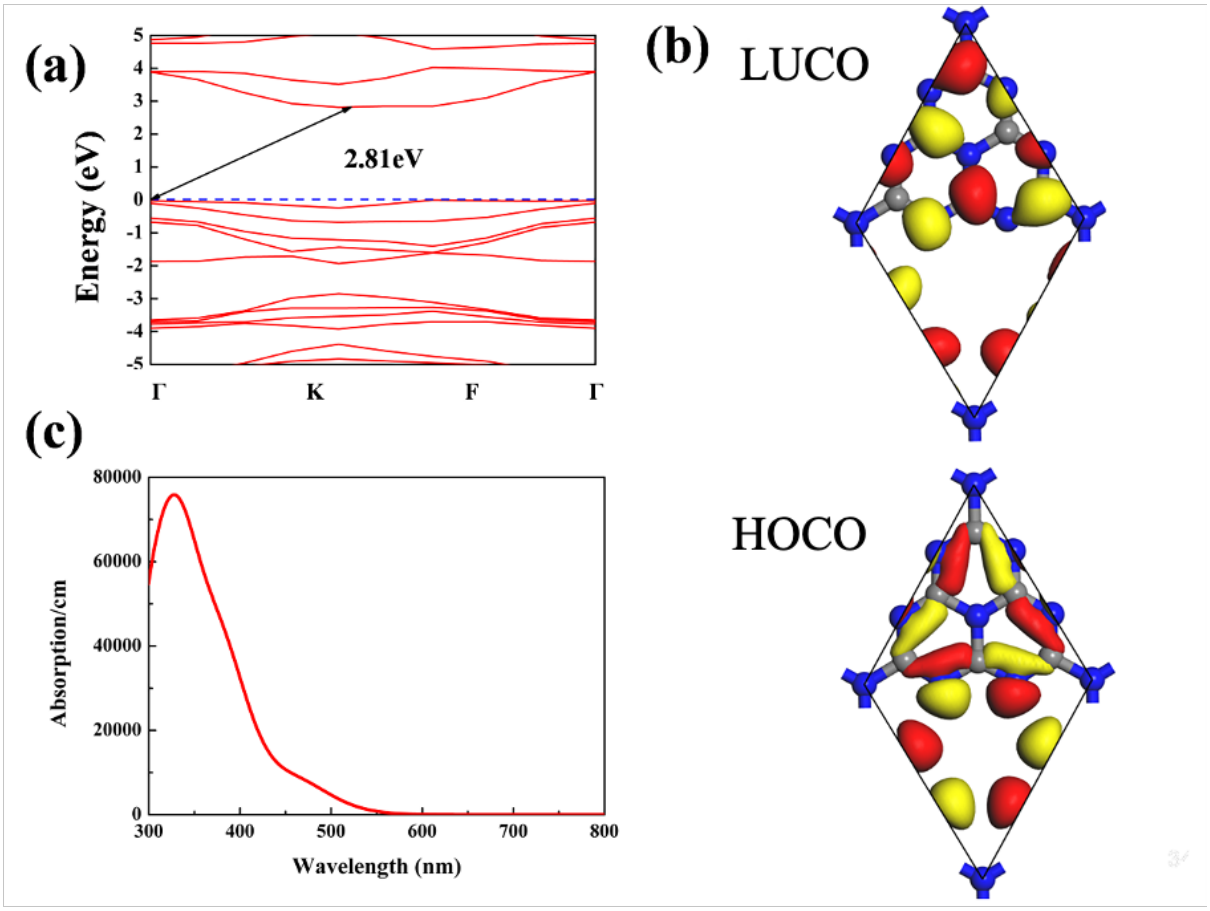

Figure 3.4: (a) Band structure, (b) HOCO and LUCO, and (c) absorption spectra of g-C_3N_4. The red and yellow isosurfaces in HOCO and LUCO represent positive and negative values of the wave function, respectively.

3.3.3 The Mechanism of C1 Product Reduction Path

Based on the above results, the important question is whether C_3N_5 can efficiently catalyze CO_2, like other CN_x materials [45,46]. In the following, the mechanism of CO_2 reduction to C1 product catalyzed by C_3N_5 is explored by DFT calculations, and the free energy diagrams and optimized structures for CO_2 reduction to CH_4 are shown in Figure 3.5 (a)-(c). The overall reaction of CO_2 reduction to CH_4 on C_3N_5 in the presence of hydrogen is expressed as follows:

$$CO_2 + 8H^+ + 8e^- \rightarrow CH_4 + 2H_2O \quad (3\text{-}8)$$

All possible adsorption sites of each intermediate were considered and confirmed that the active site for CO_2RR is N_3 atom in −N=N− linkage (see Figure 3.1(a)). The reaction paths in free energy (ΔG) diagram on C_3N_5 and g-C_3N_4 are shown in Figure 3.5 (b). It has been already proved [45] that the optimal reaction path of CO_2 reduction on g-C_3N_4 is $CO_2 \rightarrow$ COOH* $\rightarrow$ CO* $\rightarrow$ HCO* $\rightarrow$ HCHO* $\rightarrow$ CH_3O* $\rightarrow$ CH_3OH (see Figure 3.5 (b)). The ΔG for $CO_2 \rightarrow$ COOH* and $CO_2 \rightarrow$ HCOO* on C_3N_5 is 0.54 eV and 2.42 eV (Table A.1), respectively, so the formation of HCOO* is not considered due to large ΔG. In addition, the ΔG of $CO_2 \rightarrow$ COOH* is far less than that on g-C_3N_4 (1.41 eV [16], Figure 3.5 (b), Table A.1). The adsorption energy of CO* on C_3N_5 is −1.80 eV (Table A.2), and the optimized structure of CO* shows that C atom of CO links to N_3 atom in −N=N− linkage and N_1 atom in C_6N_7 unit to form five-membered ring (Figure 3.5 (c)). Compared with g-C_3N_4, CO adsorption on C_3N_5 is much stronger than that on g-C_3N_4 (−0.23 eV, Table A.2). Therefore, CO is easier to be further hydrogenated rather than desorbed. In the following step, the $H^+ + e^-$ pair attacks the O atom of CO* to generate COH* ($\Delta G = -0.17$ eV), while the ΔG of HCO formation is 0.79 eV. The formed COH* species can be further reduced by another $H^+ + e^-$ pair to C* or CHOH* species. The formed CHOH* is energetically much more stable than that of C*. The CHOH* can be further hydrogenated to CH* or CH_2OH*, the formation of CH*($\Delta G = -0.30$ eV) is easier than that of CH_2OH* ($\Delta G = 0.41$ eV). In the subsequent step, CH* will be hydrogenated to CH_4 by reacting with three $H^+ + e^-$ pairs. The values of ΔG for CH_2*, CH_3, and CH_4 formation are −0.30 eV, 0.12 eV, and −0.14 eV, respectively, so CH_4 is the final C1 product. The C1 product optimal pathway on C_3N_5 is $CO_2 \rightarrow$ COOH* $\rightarrow$ CO* $\rightarrow$ COH* $\rightarrow$ CHOH* $\rightarrow$ CH* $\rightarrow$ CH_2 *$\rightarrow$ CH_3* $\rightarrow$ CH_4 and the first step ($CO_2 \rightarrow$ COOH*) is the rate-determining step with a ΔG_{max} of 0.54 eV, it can be seen that the U_L on C_3N_5 and g-C_3N_4 are −0.54 V and −1.43 V, respectively.

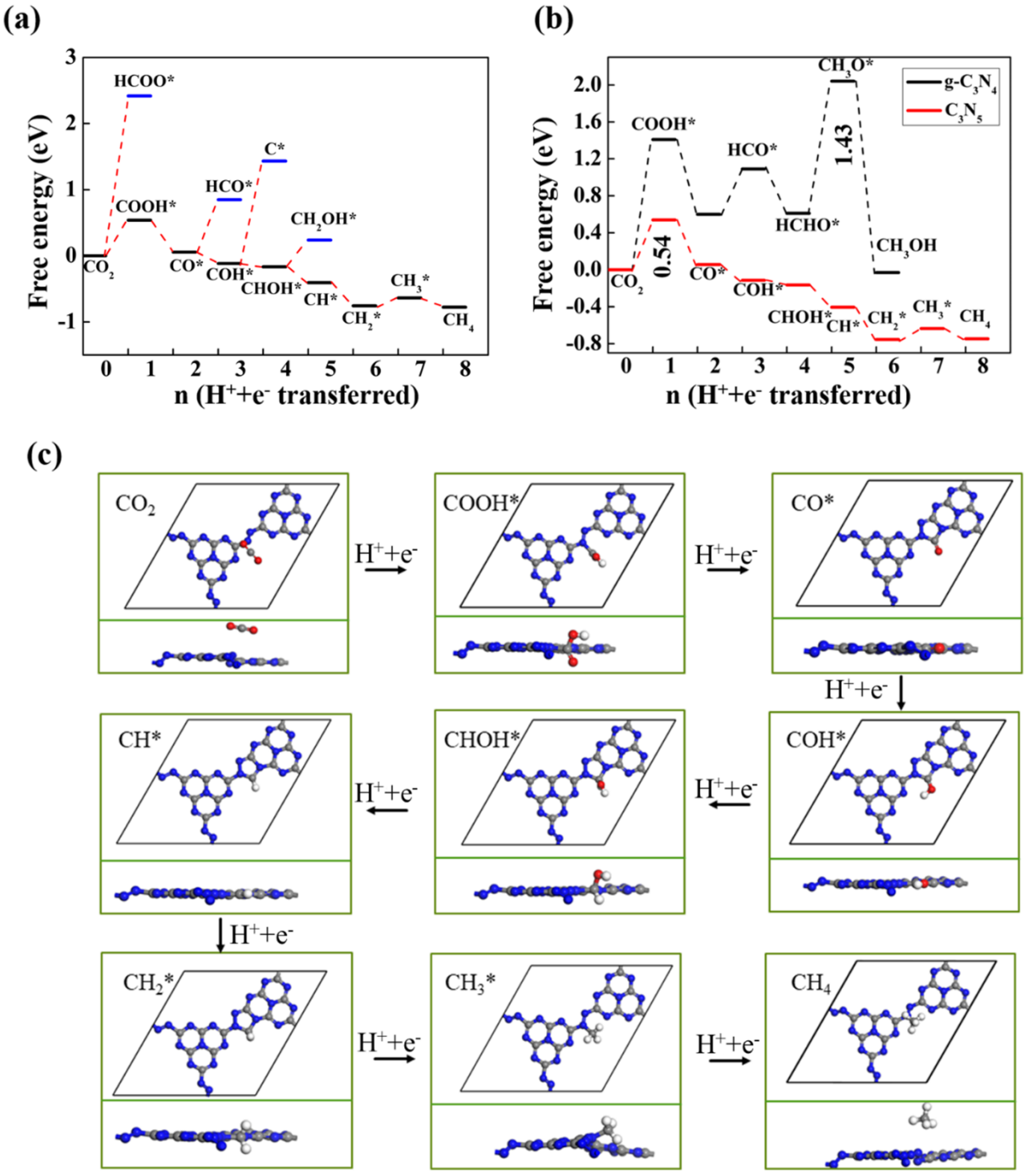

Figure 3.5: (a) Calculated free energy diagram corresponding to the reaction path followed by the CO_2 reduction to CH_4 on C_3N_5. (b) Calculated free energy diagram corresponding to the optimal path followed by the CO_2 conversion on the C_3N_5 and g-C_3N_4. (c) Calculated structures corresponding to the optimal reaction path for the CO_2RR on C_3N_5.

To provide insights into the different adsorption strengths of COOH on C_3N_5 and g-C_3N_4, I first decomposed E_{ads} of COOH into interaction (E_{int}) and deformation energies (E_{def}) (Table 3.1). The calculations and electronic structure analysis (will be discussed in the following) are performed using STATE code [47] without the solvent model using the PBE+D2 functional and the lattice parameters of C_3N_5 and g-C_3N_4 from the DMol^3 code results. I confirmed the relative stability of the COOH adsorptions on C_3N_5 and on g-C_3N_4 does not alter when the solvent model is not included. From Table 3.1, E_{int} is the key contributor to causing the binding strength difference of COOH adsorbed on C_3N_5 and g-C_3N_4, thus the difference in E_{ads} is mainly due to the differences in chemical bonding characters of COOH with C_3N_5 and g-C_3N_4. Moreover, I found that C_3N_5 is more flexible upon COOH adsorption, as indicated by the less positive deformation energy of C_3N_5 (Table 3.1). It is due to the pore size of C_3N_5 (14.86 Å, Figure 3.1(b)), which is significantly larger than that of g-C_3N_4 (5.09 Å, Figure 3.1(b)), thus less Pauli repulsive interactions between COOH and neighboring atoms of substrates appear.

Table 3.1: The calculated adsorption energies (E_{ads}) and their contribution [interaction energies (E_{int}) and deformation energies (E_{def})] of COOH on C_3N_5 and g-C_3N_4 using STATE code[a] [48-50] without solvation model. The energy difference (ΔE) between COOH/C_3N_5 and COOH/g-C_3N_4 is included. The results using DMol^3 code with solvation model are given in parentheses. [a] The ionic cores are replaced by ultrasoft pseudopotentials, whereas the valance electrons are expanded using plane basis sets with kinetic cutoff energies of 36 and 400 Ry for wave functions and augmented charge densities, respectively.

	E_{ads}(COOH/S)	E_{int} (COOH/S)	E_{def} (COOH)	E_{def} (S)
substrate	eV	eV	eV	eV
C_3N_5	−2.21 (−2.48)	−3.27	0.45	0.61
g-C_3N_4	−1.28 (−1.61)	−2.51	0.51	0.72
ΔE	−0.93 (−0.87)	−0.76	−0.06	−0.11

To further investigate the bonding contribution, we calculated the PDOS [48-50] onto the crystal orbitals (CO) of the isolated COOH and crystal orbital overlap population (COOP) [48-50] (Figure 3.6 (a) and (b)). Positive and negative values of COOP imply bonding and antibonding characteristics between the adsorbate and the substrate, respectively. The HOCO, singly occupied crystal orbital (SOMO), and LUCO of the isolated COOH at their adsorption configurations on substrates are shown in Figure 3.6 (c), respectively. Gross Population (GPOP) for those COs of isolated COOH, COOH/C_3N_5, and COOH/g-C_3N_4 are listed in Table 3.2.

As shown in Figure 3.6 (a), there is a significant hybridization between SOCO of COOH and wave functions of C_3N_5 as indicated by several bonding peaks at ~ E_F − 14 eV, E_F − 10 eV, E_F − 5 eV, and E_F − 2 eV. Moreover, LUCO of COOH almost has no interaction with wave functions of C_3N_5 due to only weak bonding peaks at ~E_F − 3 eV and E_F − 1 eV. Similarly, in the case of COOH/g-C_3N_4 (Figure 3.6 (b)), SOCO of COOH also has a strong bonding character with the wave functions of g-C_3N_4. Nevertheless, I found an antibonding peak of SOCO appeared at the Fermi level, indicating the repulsive interaction between this CO and g-C_3N_4. Notably, LUCO of COOH has a small hybridization with g-C_3N_4, which is totally different from the case of COOH on C_3N_5, where the LUCO of COOH interacts very weakly with C_3N_5. At the Fermi level, there is a partially bonding PDOS peak of LUCO of COOH, originating from an σ-bonding between *p* orbital of N atom in g-C_3N_4 and that of C atom in COOH (Figure 3.6 (d)). As listed in Table 3.2, total charge transfer from g-C_3N_4 (C_3N_5) to LUCO of COOH is 0.20 (0.06) e^-, indicating there is more charge transfer from g-C_3N_4 to LUCO of COOH compared with that from C_3N_5. The work functions of clean g-C_3N_4 and C_3N_5 are 5.8 eV and 6.9 eV, respectively, clearly reflecting the ability of charge transfer of those materials. From above analysis, the destabilization of COOH/g-C_3N_4 is attributed to the appearances of the partially occupied antibonding peak of SOCO and bonding peak of LUCO at the Fermi level.

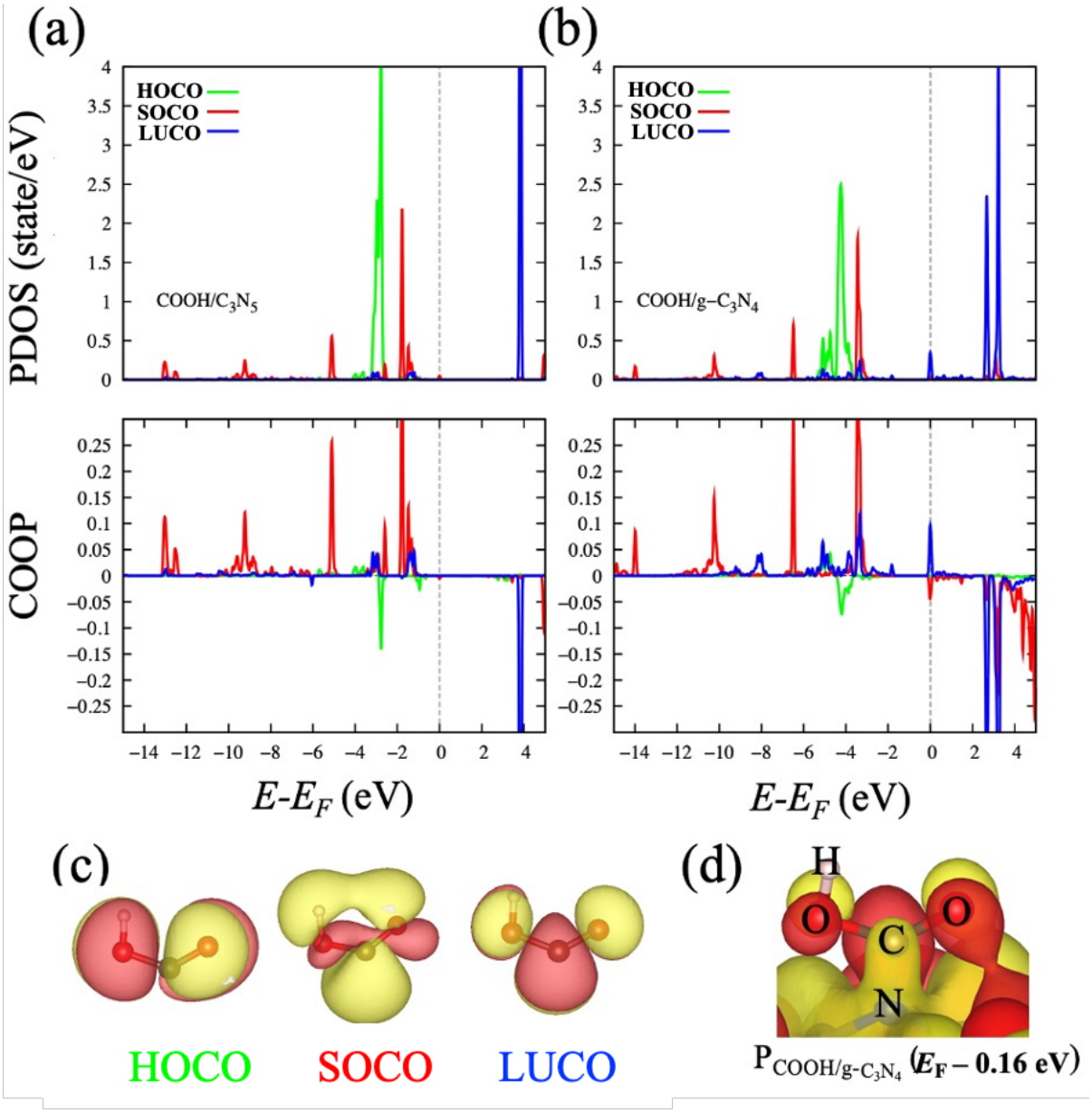

Figure 3.6: Projected density of states (PDOS) (upper) onto crystal orbitals (CO) and crystal orbital overlap population (COOP) (bottom) of COOH adsorbed on C_3N_5 (a), g-C_3N_4 (b). COs of isolated COOH at their adsorption configurations (c). The wave functions of COOH adsorbed on g-C_3N_4 at the Fermi level (d). The red and yellow isosurfaces represent positive and negative values of wave function, respectively.

Table 3.2: Gross Population (GPOP) for crystal orbitals of isolated COOH, COOH/C_3N_5 and COOH/g-C_3N_4.

GPOP	HOCO	SOCO	LUCO
isolated COOH	2.00	1.00	0.00
COOH/C_3N_5	1.98	0.76	0.06
COOH/g-C_3N_4	1.98	0.78	0.20

3.3.4 The Mechanism of C2 Product Reduction Path

Based on the previous studies [24-27], the possible of C2 products also are considered. All possible adsorption sites of each intermediate were considered and the optimal reaction paths in free energy diagram and optimized structures are shown in Figure 3.7 (a)-(b) and the ΔG of all intermediates are shown Table A.3. C–C bond coupling is key step to generate the C2 products. According to the reaction pathways (Scheme 3.1), CO may be coupled with CO*, COH*, CH*, CH_2* to get C–C bond coupling. In my case, CO* is much easier hydrogenated to COH*($\Delta G = -0.17$ eV) than that is coupled with CO ($\Delta G = -0.02$ eV) and the following step (COHCO* → CCO*) has a quite high uphill ($\Delta G = 1.51$ eV), so the formation of COCO* is not considered. The second possibility is that the CO may be coupled with COH*, the results on ΔG show that even though the ΔG of COH* → COHCO* ($\Delta G = -0.48$ eV) is smaller than that of COH→ CHOH* ($\Delta G = -0.10$ eV), the next step (COHCO* → CCO*) has a large positive ΔG (1.51 eV), so the COCOH cannot be further hydrogenated to CCO*. In the other path, COHCO* also can be hydrogenated to HOCCOH* due to the $H^+ + e^-$ pair attacks the left side O atom of COHCO*, while HOCCOH* hydrogenation to CCOH* is not feasible due to the large ΔG (1.60 eV). Therefore, the CO coupled with COH* to COHCO* is not considered. Similarly, CH* is much easier hydrogenated to CH_2* than that is coupled with CO (Table A.3).

In the following step, CH_2 also can be considered to couple with CO to CH_2CO* or hydrogenated to CH_3*. The simulated results indicate that coupling to CH_2CO* is much more favourable, because the process of CH_2* → CH_2CO*($\Delta G = -0.64$ eV) is exothermic, whereas the ΔG of CH_2* → CH_3* is 0.30 eV.

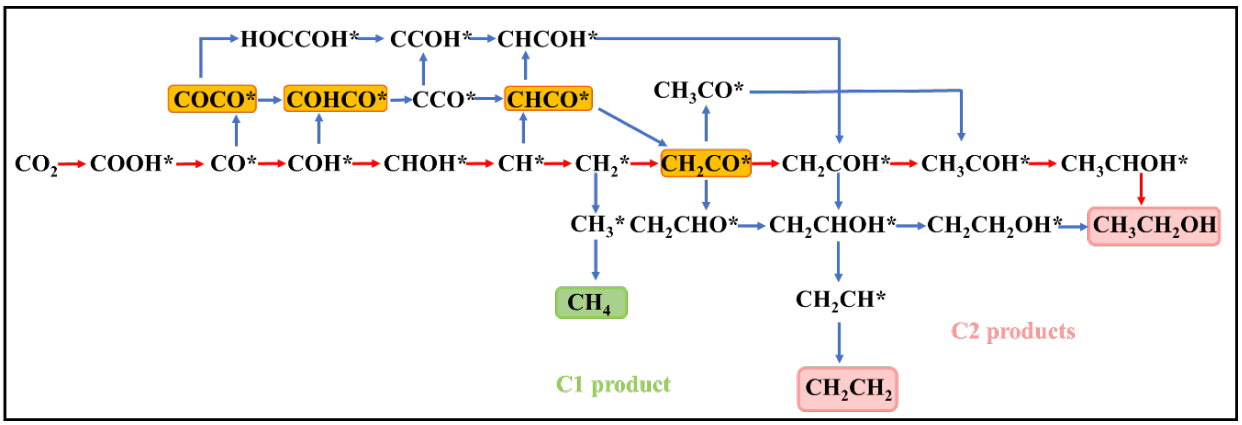

Scheme 3.1: Proposed reaction paths for CO_2 reduction on C_3N_5 for producing C1 and C2 products.

C–C bond coupling step is confirmed, next steps are back to hydrogenation. CH_2CO* may be further hydrogenated to CH_2COH*, CH_2CHO* and CH_3CO* due to the $H^+ + e^-$ pair attacks. Based on the results, the formation to CH_2COH* (ΔG = 0.33 eV) is more easily than the formation to CH_3CO* (ΔG = 0.58 eV) or CH_2CHO*(ΔG = 1.03 eV). Next step, there are two possibilities for hydrogenation of CH_2COH* to CH_3COH* or CH_2CHOH*, which is key step for CH_3CH_2OH or CH_2CH_2 formation. From the results on free energy shown that the CH_2COH* → CH_3COH* and CH_2COH* → CH_2CHOH* are exothermic, it means that CH_3COH* and CH_2CHOH* are possible intermediates by considering the thermodynamics. However, to further investigate which one is more easily hydrogenated by CH_2COH*, the activation barriers (E_a) for CH_2COH* + H* → CH_3COH* and CH_2COH* + H* → CH_2CHOH* on C_3N_5 are also calculated and shown in Figure 3.7 (c). The results shown that the E_a of CH_2COH* + H* → CH_3COH* and CH_2COH* + H* → CH_2CHOH* are 0.20 eV and 3.50 eV, respectively, thus it can be reduced to CH_3COH* easily compared with reduced to CH_2CHOH*

due to the less E_a. According to the calculation, the next step is $CH_3COH^* \rightarrow CH_3CHOH^*$ with ΔG of 0.61 eV. Finally, CH_3CH_2OH is the C2 product. In summary, the ΔG of rate-determining step ($CH_3COH^* \rightarrow CH_3CHOH^*$) and the limiting potential (U_L) are 0.61 eV and −0.61 V, respectively, and the C2 product optimal reaction path on C_3N_5 I have proposed above, $CO_2 \rightarrow COOH^* \rightarrow CO^* \rightarrow COH^* \rightarrow CHOH^* \rightarrow CH^* \rightarrow CH_2 ^* \rightarrow CH_2CO^* \rightarrow CH_2COH^* \rightarrow CH_3COH^* \rightarrow CH_3CHOH^* \rightarrow CH_3CH_2OH$ seems to be reasonably feasible.

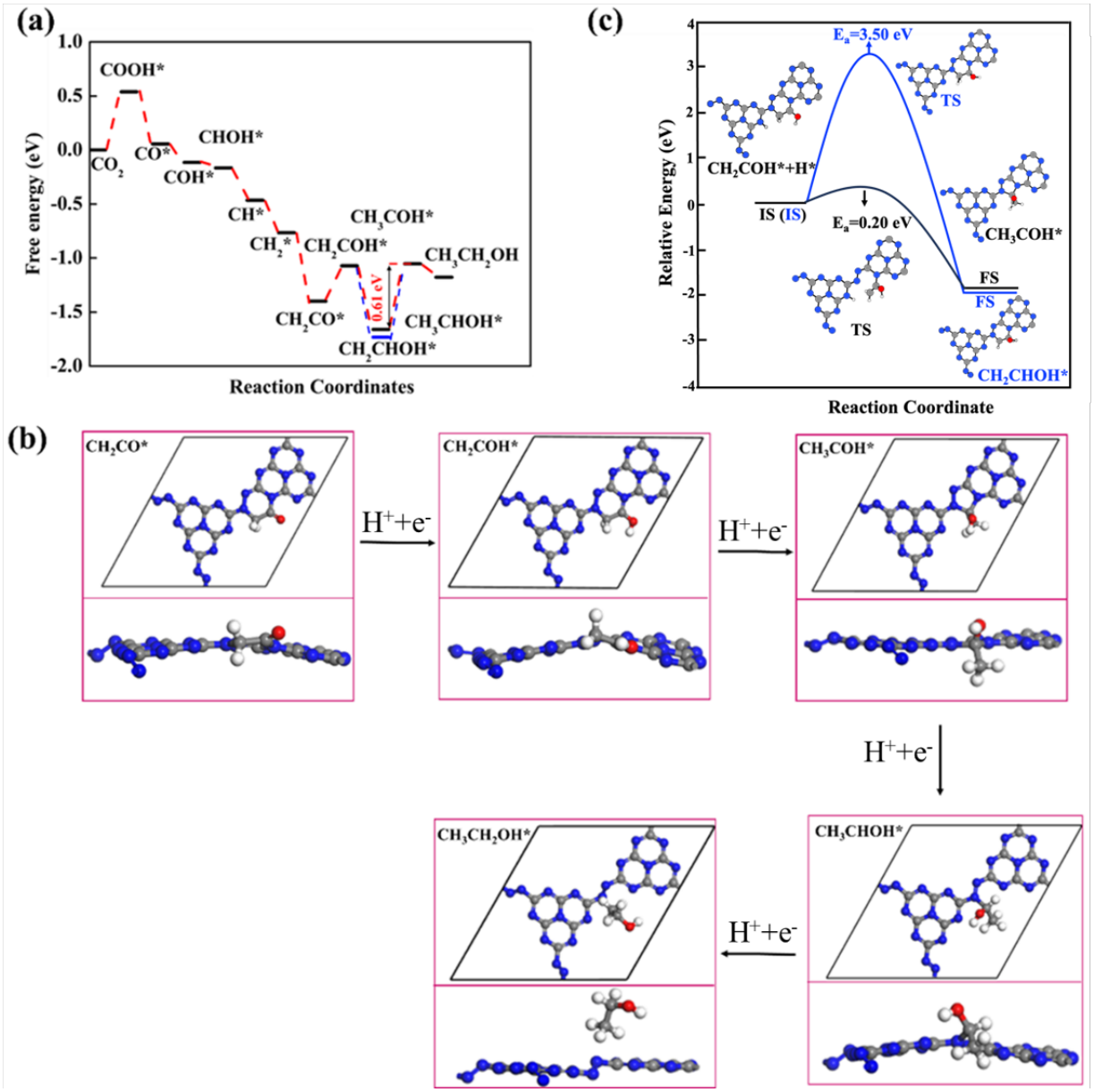

Figure 3.7: (a) Calculated free energy diagram corresponding to the reaction path followed by the CO_2 reduction to CH_3CH_2OH on C_3N_5. (b) Calculated structures corresponding to the

optimal reaction path for CH_3CH_2OH on C_3N_5. (c) Initial state (IS), transition state (TS) and final state (FS) structure diagrams and activation barriers involved in the reaction CH_2COH^* + $H^* \rightarrow CH_3COH^*$ and $CH_2COH^* + H^* \rightarrow CH_2CHOH^*$ on C_3N_5 using CI-NEB.

3.3.5 Side Reaction Analyses

In CO_2RR, the competing hydrogen evolution reaction (HER) should be considered [51]. As shown in Figure 3.8 (a), the free energy diagram of HER (ΔG = 1.18 eV) is all larger than the ΔG of rate-determining step for C1 product (0.54 eV) and C2 product (0.61 eV) on C_3N_5. Thus, C_3N_5 exhibits high suppressing effect on HER during the CO_2RR process. For g-C_3N_4, the free energy diagram of HER (ΔG = 0.25 eV) indicates that HER is easy, which is consistent with the experimental result [12]. So g-C_3N_4 is not an efficient catalyst for CO_2RR because of strong catalytic ability on HER. Furthermore, the difference of limiting potentials between CO_2 reduction and H_2 evolution (i.e., $U_L(CO_2) - U_L(H_2)$) can evaluate the selectivity of CO_2 reduction, which more positive $U_L(CO_2) - U_L(H_2)$ corresponds to a higher selectivity toward CO_2 reduction [52,53]. As shown in Figure 3.8 (b), $U_L(CO_2) - U_L(H_2)$ for C1 product (0.64 V) and C2 product (0.57 V) are all more positive than that for Ni/Fe-N-C (about 0.08 V) [52], which is recently proved to have high selectivity for CO_2 reduction experimentally. Therefore, it further infers that C_3N_5 has a higher CO_2 reduction selectivity.

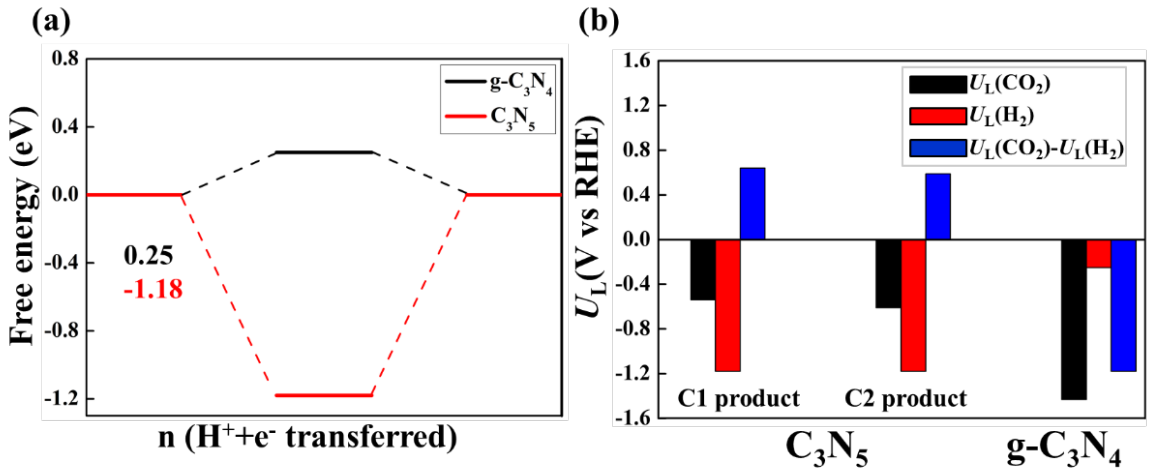

Figure 3.8: (a) Energy profile for the HER on the C_3N_5 and g-C_3N_4. (b) Calculated limiting potentials for CO_2RR, HER, and their difference.

3.4 Summary

In summary, I systematically studied the CO_2RR catalytic mechanism of new-type nitrogen-rich carbon nitride materials, namely C_3N_5 by DFT calculations. The AIMD simulations show that C_3N_5 is at least locally stable 2D structure. Due to introducing −N=N− linkage, C_3N_5 possesses a more suitable band gap (2.0 eV) than that of g-C_3N_4 and extends the π network resulting in more electron transfer, which effectively separates the photogenerated e^-/h^+ pairs. Compared with g-C_3N_4, the photocatalytic efficiency of C_3N_5 is enhanced. The thermodynamic computations demonstrate that C_3N_5 is a promising CO_2RR photocatalyst with an outstanding photocatalytic activity and reduced to CH_4 and CH_3CH_2OH with rather low limiting potential of −0.54 V and −0.61 V, resepctively, which can be driven by solar energy. It is expected that the present work would motivate further experimental and theoretical studies focusing on development of C_3N_5 photocatalysts.

References

[1] A. S. Varela, W. Ju, T. Reier, P. Strasser, ACS Catal. **6**, 2136-2144 (2016).

[2] D. Gao, H. Zhou, F. Cai, J. Wang, G. Wang, X. Bao, ACS Catal. **8**, 1510-1519 (2018).

[3] S. Liu, H. Tao, L. Zeng, Q. Liu, Z. Xu, Q. Liu, J. L. Luo, J. Am. Chem. Soc. **139**, 2160-2163 (2017).

[4] J. T. Feaster, C. Shi, E. R. Cave, T. Hatsukade, D. N. Abram, K. P. Kuhl, C. Hahn, J. K. Nørskov, T. F. Jaramillo, ACS Catal., **7**, 4822-4827 (2017).

[5] C. Dong, J. Fu, H. Liu, T. Ling, J. Yang, S. Z. Qiao, X. W. Du, J. Mater. Chem. A, **5**, 7184-7190 (2017).

[6] J. Qiao, Y. Liu, F. Hong, J. Zhang, Chem. Soc. Rev., **43**, 631-675 (2014).

[7] X. Duan, J. Xu, Z. Wei, J. Ma, S. Guo, S. Wang, H. Liu, S. Dou, Adv. Mater., **29**, 1701784 (2017).

[8] W. Ong, L. Tan, Y. Ng, S. Yong, S. Chai, Chem. Rev., **116**, 7159-7329 (2016).

[9] X. Wang, K. Maeda, A. Thomas, K. Takanabe, G. Xin, J. M. Carlsson, K. Domen, M. Antonietti, Nat. Mater., **8**, 76 (2008).

[10] P. Kumar, R. Boukherroub, K. Shankar, J. Mater. Chem. A, **6**, 12876-12931 (2018).

[11] Y. Zheng, Y. Jiao, Y. Zhu, Q. Cai, A. Vasileff, L. H. Li, Y. Han, Y. Chen, S. Z. Qiao, J. Am. Chem. Soc., **139**, 3336-3339 (2017).

[12] Y. Jiao, Y. Zheng, P. Chen, M. Jaroniec, S. Z. Qiao, J. Am. Chem. Soc., **139**, 18093-18100 (2017).

[13] S. Tonda, S. Kumar, S. Kandula, V. Shanker, J. Mater. Chem. A, **2**, 6772-6780 (2014).

[14] Y. L. Wang, Y. Tian, L. K. Yan, Z. M. Su, J. Phys. Chem. C, **122**, 7712-7719 (2018).

[15] J. Ran, T. Y. Ma, G. Gao, X.W. Du, S. Z. Qiao, Energy Environ. Sci., **8**, 3708-3717(2015).

[16] N. Sagara, S. Kamimura, T. Tsubota, T. Ohno, Appl. Catal., B, **192**, 193-198. (2016)

[17] J. Li, B. Shen, Z. Hong, B. Lin, B. Gao, Y. Chen, Chem. Commun., **48**, 12017-12019 (2012).

[18] Y. L. Wang, Y. Tian, Z. L. Lang, W. Guan, L.K. Yan, J. Mater. Chem. A, **6**, 21056-21063 (2018).

[19] Y. He, L. Zhang, B. Teng, M. Fan, Environ. Sci. Technol., **49**, 649-656 (2015).

[20] Y. L. Wang, C. X. Wu, Y. Tian, L. K. Yan, H. Q. Tan, Z. M. Su, Appl. Surf. Sci., **453**, 442-448 (2018).

[21] A. Schwarzer, T. Saplinova, E. Kroke, Coord. Chem. Rev., **257**, 2032-2062 (2013).

[22] M. B. Robin, W. T. Simpson, J. Chem. Phys., **36**, 580-588 (1962).

[23] P. Kumar, E. Vahidzadeh, U. K. Thakur, P. Kar, K. M. Alam, A. Goswami, N. Mahdi, K. Cui, G. M. Bernard, V. K. Michaelis, K. Shankar, J. Am. Chem. Soc., **141**, 5415-5436 (2019).

[24] L. R. L. Ting, O. Piqué, S. Y. Lim, M. Tanhaei, F. Calle-Vallejo, B. S. Yeo, ACS Catal., **10**, 4059-4069 (2020).

[25] J. Zhao, Z. Chen, J. Zhao, J. Mater. Chem. A, **7**, 4026-4035 (2019).

[26] X. Liu, Z. Wang, Y. Tian, J. Zhao, J. Phys. Chem. C, **124**, 3722-3730 (2020).

[27] S. Chen, H. Yuan, S. I. Morozov, L. Ge, L. Li, L. Xu, W. A. Goddard, J. Phys. Chem. Lett., **11**, 2541-2549 (2020).

[28] B. Delley, J. Chem. Phys., **92**, 508-517 (1990).

[29] B. Delley, J. Chem. Phys., **113**, 7756-7764 (2000).

[30] J. P. Perdew, K. Burke, M. Ernzerhof, D.of Physics and NOL 70118 J. Quantum theory group Tulane University. Phys. Rev. Lett., **77**, 3865-3868 (1996).

[31] S. Grimme, J. Comput. Chem., **27**, 1787-1799 (2006).

[32] A. Klamt, G. Schuurmann, J. Chem. Soc., Perkin Trans., **2**, 799-805 (1993).

[33] J. Heyd, G. E. Scuseria, J. Chem. Phys., 1**21**, 1187-1192 (2004).

[34] M. D. Segall, P. L. D. Lindan, M. J. Probert, C. J. Pickard, P. J. Hasnip, S. J. Clark, M. C. Payne, J. Phys.: Condens. Matter, **14**, 2717-2744 (2002).

[35] J. Heyd, G. E. Scuseria, M. Ernzerhof, J. Chem. Phys., **118**, 8207-8215 (2003).

[36] G. Henkelman, Jonsson, H. J. Chem. Phys., **113**, 9978-9985 (2000).

[37] S. Zuluaga, S. Stolbov, J. Chem. Phys., **135**, 134702 (2011).

[38] Y. Hamamoto, I. Hamada, K. Inagaki, Y. Morikawa, Phys. Rev. B, **93**, 245440 (2016).

[39] J. K. Nørskov, J. Rossmeisl, A. Logadottir, L. Lindqvist, J. Phys. Chem. B, **108**, 17886-17892 (2004).

[40] D. H. Lim, J. Wilcox, J. Phys. Chem. C, **116**, 3653-3660 (2012).

[41] Y. Wang, H. Yuan, Y. Li, Z. Chen, Nanoscale, **7**, 11633-11641(2015).

[42] S. Kattel, P. Atanassov, B. Kiefer, J. Phys. Chem. C, **116**, 17378-17383 (2012).

[43] S. J. Clark, M. D. Segall, C. J. Pickard, P. J. Hasnip, M. I. J. Probert, K. Refson, M. C. Payne, Z. Kristallogr., **220**, 567-570 (2005).

[44] L. M. Azofra, D. R. MacFarlane, C. Sun, Phys. Chem. Chem. Phys., **18**, 18507-18514 (2016).

[45] W. J. Ong, L. L. Tan, Y. H. Ng, S.T. Yong, S. P. Chai, Chem. Rev., **116**, 7159-7329 (2016).

[46] X. Li, J. Yu, S. Wageh, A. A. Al-Ghamdi, J. Xie, Small, **12**, 6640-6696 (2016).

[47] Y. Morikawa, Phys. Rev. B, **51**, 14802 (1995).

[48] I. Hamada, Y. Morikawa, J. Phys. Chem. C, **112**, 10889-10898 (2008).

[49] I. Hamada, Y. Morikawa, J. Chem. Phys., **134**, 154701 (2011).

[50] T. N. Pham, Y. Hamamoto, K. Inagaki, D. N. Son, I. Hamada, Y. Morikawa, J. Phys. Chem. C, **124**, 2968-2977 (2020).

[51] H. Shen, Y. Li, Q. Sun, J. Phys. Chem. C, **121**, 3963-3969 (2017).

[52] W. Ren, X. Tan, W. Yang, C. Jia, S. Xu, K. Wang, S. C. Smith, C. Zhao, Angew. Chem. Int. Ed., **58**, 6972-6976 (2019).

[53] D. Kim, C. Xie, N. Becknell, Y. Yu, M. Karamad, K. Chan, E. J. Crumlin, J. K. Nørskov, P. Yang, J. Am. Chem. Soc., **139**, 8329-8336 (2017).

Chapter 4

Activity and Selectivity of N_2 Fixation on B-doped g-C_9N_{10}: A Density Functional Theory Study

4.1 Introduction

N_2 fixation to produce ammonia (NH_3) is an important process because NH_3 can be utilized as a raw material of fertilizers and energy storage intermediate. Although N_2 is abundant in the earth's atmosphere (> 70%), the N≡N bond in N_2 is very stable, leading to difficulty in reducing N_2 to NH_3 at ambient conditions [1-3]. Ammonia is produced industrially from N_2 and H_2 via the Haber-Bosch method, but it not only requires extreme conditions (high temperatures and pressures) but also produces greenhouse CO_2 gas. Photocatalysis and electrocatalysis of N_2 are of great interest as environmentally friendly methods of NH_3 production because they can significantly enhance the reaction rate, increase selectivity, decrease the energy consumption of the reactions, and avoid CO_2 generation [4-6]. Therefore, exploring a suitable catalyst for the N_2 reduction reaction (N_2RR) holds importance for sustainable society development.

Up to now, N_2RR is carried out by using metal-based catalysts due to a strong N_2 adsorption ability [7-8]. However, metal-based catalysts exhibit several drawbacks such as low selectivity, poor durability, and high price. Compared with metal-based catalysts, metal-free carbon materials have attracted more attention recently due to their advantages such as excellent stability, low price, high surface area, and environmental friendliness [9]. Based on these advantages, metal-free carbon materials are widely used in various catalytic reactions, such as carbon dioxide reduction reaction (CO_2RR), oxygen reduction/evolution reaction

(ORR/OER), nitrogen reduction reaction (N_2RR) and hydrogen evolution reaction (HER) [10]. More and more carbon nitride materials (CN_x) are synthesized and proven to have good catalytic activity for various photocatalysis reactions. According to the C:N ratio from 0.6 to 3, the names of CN_x materials are distinguished as C_3N_5, C_3N_4, C_2N, C_9N_4, C_3N, and so on. Graphitic carbon nitride (g-C_3N_4) with a C:N ratio of 0.75 is the one of representative CN_x materials, which has a good catalytic activity for water splitting [11]. Increasing the N concentration, as found in a recently synthesized C_3N_5, also provides outstanding photocatalytic activity by reducing the band gap and making visible light with longer wavelength available [12]. I previously investigated the catalytic activity of C_3N_5 for CO_2RR and indicated that C_3N_5 is a promising CO_2RR photocatalyst with an outstanding photocatalytic activity [13]. In 2013, Kroke *et al.* [14] proposed a hypothetical new CN two-dimensional material of which the unit cell is composed of one C_6N_7 motif and one C_3N_3 motif connected via C–C bonds resulting in a graphene-like carbon nitride with a C:N ratio of 9:10 (referred to as g-C_9N_{10}). Li *et al*. [15] indicated that g-C_9N_{10} is stable as shown in phonon spectrum and *ab initio* molecular dynamics (AIMD) simulations, and it could be synthesized in the near future.

Typically, the chemisorption of N_2 on the catalyst is a prerequisite condition for an efficient N_2RR catalyst. Braunschweig *et al*. [16] reported that the boron (B) atom is an electron-deficient atom, and it has Lewis-acid characteristics, so 2s and 2p orbitals will first hybridize to generate sp^3 orbitals when the B atom is attacked by Lewis base (such as N_2). The unoccupied sp^3 orbitals of B atom will accept the lone-pair electrons of N_2 and the occupied sp^3 orbitals of B donate the electrons to empty π^* orbitals, which can drive the "σ donation-π backdonation process" [16].

Several experimental and theoretical works on B-doped CN_x materials and B-based clusters proved that boron materials are beneficial for N_2RR activity [17-21]. Zhao *et al.* [17] reported BCN matrix and Ni nanoparticles promote a synergetic effect for the electrochemical

N_2RR efficiency. Li *et al.* [22] proved that the doped B−N pairs in a carbon matrix can highly efficiently improve N_2RR activity. Wang *et al*. [23] reported that a single B atom doped g-C_3N_4 with sp^3 hybridization also contains occupied and empty orbitals simultaneously, indicating its potential for N_2 fixation by DFT. Inspired by the above studies, I got the idea to combine the characteristics of B atoms and g-C_9N_{10} to design novel catalysts for N_2 fixation.

In this work, I construct the seven B atom doping structures, namely B substituted C or N and anchored on g-C_9N_{10}. The stability of different doping sites is evaluated and B_{N1} and B_A (B_{C1}) are stable at N-poor (rich) conditions. I found that N_2 chemisorbed on B_{N1} and B_A ones due to "σ donation-π backdonation" process. The free energy results show that the preferable N_2RR mechanism of the B_{N1}- and B_A-doped g-C_9N_{10} is a mix I mechanism starting from the end-on N_2 with a low limiting potential of −0.62 V and −0.44 V, respectively. B_{N1}-doped g-C_9N_{10} has excellent catalytic activity and selectively for N_2RR due to low limiting potential and stronger N_2 adsorption over H adsorption, while B_A-doped g-C_9N_{10} suffers the stronger H poisoning effect due to stronger H adsorption. The electronic structure analysis reveals the origin leading to the different adsorption behavior of N_2 and H.

4.2 Computational Details

Most of our DFT calculations were performed with the Simulation Tool for the Atom TEchnology (STATE) program package [24-27]. The Perdew-Burke-Ernzerhof (PBE) exchange-correlation functional of the generalized gradient approximation (GGA) was used to describe the electron interactions [28]. The PBE+D2 method with the Grimme van der Waals (vdW) [29] correction was employed to describe the weak interactions between various intermediates. Electron spin-polarization was considered in all the calculations. Ionic cores were described by using the ultrasoft pseudopotentials [30], and valence electron states were expanded by a plane wave basis set with the kinetic energy cutoffs of 36 and 400 Ry for wave

functions and augmented charge density, respectively. The vacuum space of 20 Å is inserted in between two neighboring B-doped g-C_9N_{10} sheets to avoid spurious interactions between the two sheets. Brillouin zone integration was sampled by 4×4×1 with the Monkhorst-Pack k-points set.

The Gibbs free energy change (ΔG) was defined as [31-32]:

$$\Delta G = \Delta E + \Delta E_{ZPE} - T\Delta S + \Delta G_{pH} + \Delta G_U \quad (4\text{-}1)$$

where ΔE is the reaction energy directly obtained from DFT calculations, ΔE_{ZPE} and ΔS are the change of vibrational zero-point energy estimated from vibrational frequencies and entropy at room temperature (T = 298.15 K), respectively. To calculate the vibrational frequencies, I displaced the positions of adsorbates atoms while B doped C_9N_{10} atoms are fixed to evaluate the Hessian matrices. To verify this approach, I estimated the contribution of substrate vibration to free energy and found that this contribution can be offset as shown in Table B.1. The total entropies of the gas phase were computed from the vibrational frequencies based on the ideal gas model, while entropies of adsorbed species were negligible. The effect of electrode potential is described via $\Delta G_U = -neU$, where ne is the number of transferred electrons and U is the electrode potential. ΔG_{pH} is the correction of the H^+ free energy by the concentration, $\Delta G_{pH} = k_B T \ln 10 \times pH$, where k_B is the Boltzmann constant, and the value of pH was set to be zero to represent acidic condition in this work. The limiting potential (U_L) of the whole reduction process is determined by the potential-limiting step which has the most positive ΔG (ΔG_{max}) as computed by:

$$U_L = -\Delta G_{max}/e \quad (4\text{-}2)$$

The adsorption energies (E_{ads}) of adsorbates were calculated by the following equation:

$$E_{ads} = E_{tot}(A\text{-}S) - [E_{tot}(S) + E_{tot}(A)] \quad (4\text{-}3)$$

where E_{tot}(A-S), E_{tot}(S), E_{tot}(A) are the total energies of adsorbate-substrate (A-S) complex, clean substrate (S), and gas-phase adsorbate (A), respectively. E_{ads} can be composed into

interaction energy (E_{int}) and deformation energies (E_{def}), as calculated by following the equation [28]:

$$E_{ads} = E_{int}(\text{A-S}) + E_{def}(\text{A}) + E_{def}(\text{S}) \quad (4\text{-}4)$$

$$E_{int}(\text{A-S}) = E_{tot}(\text{A-S}) - [E_{tot}(\text{S-ads}) + E_{tot}(\text{A-ads})] \quad (4\text{-}5)$$

$$E_{def}(\text{A}) = E_{tot}(\text{A-ads}) - E_{tot}(\text{A}) \quad (4\text{-}6)$$

$$E_{def}(\text{S}) = E_{tot}(\text{S-ads}) - E_{tot}(\text{S}) \quad (4\text{-}7)$$

where E_{int}(A-S) is the interaction energy between adsorbate and substrate, while deformation energy (E_{def}) is defined as the energy necessary to deform the adsorbate and substrate upon adsorption. E_{tot}(S-ads) and E_{tot}(A-ads) are the total energies of substrate and adsorbate at their adsorption geometry in the A-S complex, respectively.

The band structure and absorption spectra were simulated using plane-wave ultrasoft (PWUS) pseudopotential method and Heyd-Scuseria-Ernzerhof (HSE06) [33-34] hybrid functional as implemented in the Cambridge Sequential Total Energy Package (CASTEP) code [35-36]. HSE06 functional can provide accurate band gaps for CN materials [37-40]. In my previous work, the calculated band gap of g-C_3N_4 is 2.81 eV, which is closed to the experiment value (2.7 eV) [11]. The absorption spectra are simulated by imaginary part of the dielectric function $\varepsilon(\omega)$ which is defined as, $\varepsilon(\omega) = \varepsilon_1(\omega) + i\varepsilon_2(\omega)$. The imaginary part $\varepsilon_2(\omega)$ is obtained from the momentum matrix elements between the occupied and the unoccupied electronic states and equation as shown in following [41-42]:

$$\varepsilon_2(\omega) = \frac{2e^2\pi}{\Omega\varepsilon_0}|\langle\psi_k^c|u\cdot r|\psi_k^v\rangle|^2\delta(E_k^c - E_k^v - \hbar\omega) \quad (4\text{-}8)$$

where, ω is the frequency of light, e is the electronic charge, ψ_k^c and ψ_k^v are the conduction and valence band wave functions at k, respectively, u is the vector indicating the polarization of the incident electric field.

4.3 Results and Discussions

4.3.1 Structure and Stability of B-doped g-C_9N_{10}

In a pure g-C_9N_{10} system, there are seven typical doping sites, including three inequivalent C atoms (C1, C2, and C3), three inequivalent N atoms (N1, N2, and N3), and anchored sites (A) as shown in Figure 4.1 (a). And seven optimized structures are shown in Figure 4.1(b)-(h). To determine the thermodynamic stability and the relative energy cost of B_{C1}, B_{C2}, B_{C3}, B_{N1}, B_{N2}, B_{N3}, and B_A-doped C_9N_{10}, the formation energies should be calculated using [43]:

$$E_f = E(B_N/\text{g-}C_9N_{10}) - E(\text{g-}C_9N_{10}) - \mu(B) + \mu(N) \quad (4\text{-}9)$$

$$E_f = E(B_C/\text{g-}C_9N_{10}) - E(\text{g-}C_9N_{10}) - \mu(B) + \mu(C) \quad (4\text{-}10)$$

$$E_f = E(B_A/\text{g-}C_9N_{10}) - E(\text{g-}C_9N_{10}) - \mu(B) \quad (4\text{-}11)$$

where $E(B_N/\text{g-}C_9N_{10})$ $E(B_C/\text{g-}C_9N_{10})$, and $E(B_A/\text{g-}C_9N_{10})$ are the total energy of $B_{N1, N2, N3}$-doped g-C_9N_{10}, $B_{C1, C2, C3}$-doped g-C_9N_{10}, and B_A-doped g-C_9N_{10}, respectively. $E(\text{g-}C_9N_{10})$ is the total energy of g-C_9N_{10}. $\mu(B)$, $\mu(C)$, and $\mu(N)$ are the chemical potential of the B, C, and N atoms, respectively. The chemical potential of B is derived from B_{12}. The calculation of $\mu(N)$ and $\mu(C)$ depends on different synthesis conditions. I assume that the doped structures are in equilibrium with g-C_9N_{10}, which implies:

$$10\mu(N) + 9\mu(C) = \mu(\text{g-}C_9N_{10}) \quad (4\text{-}12)$$

where $\mu(N)$ is determined as $\mu(N) = 0.5\,\mu(N_2)$. In Figure 4.2, it is found that at N-rich condition ($\Delta\mu_N > -0.8$ eV), B atom favorably substitutes C1 atom because of lower formation energy, whereas B atom prefers B_A site at $-1.2 < \Delta\mu_N < -0.8$ eV or substitutes N1 atom at N-poor condition, namely $\Delta\mu_N < -1.2$ eV which is consistent with other experiment of B-doped g-C_3N_4 [45].

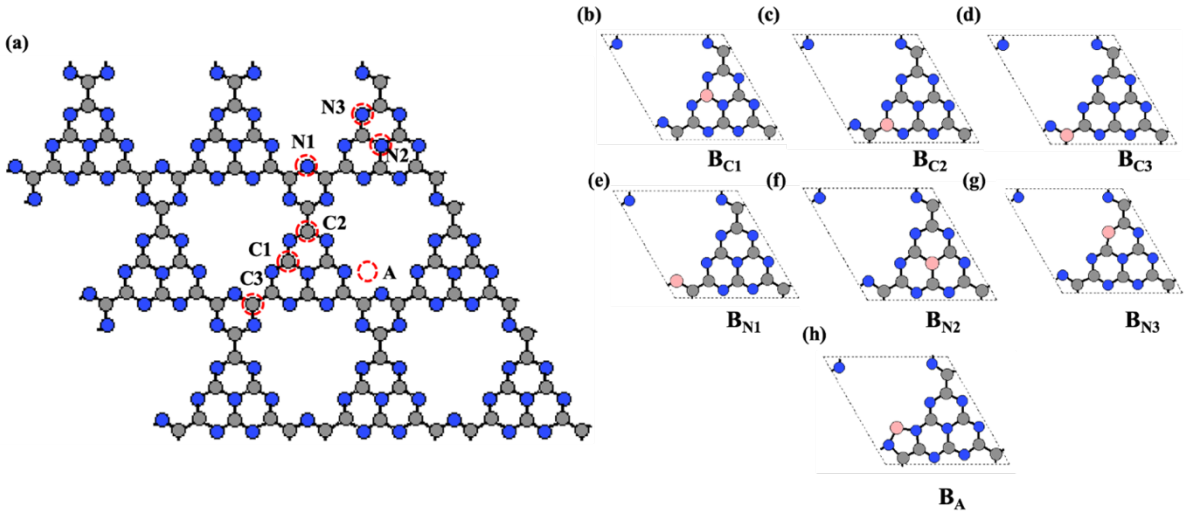

Figure 4.1: The possible site of B-doped g-C_9N_{10} (a). The optimal structure of B_{C1}-doped g-C_9N_{10} (b), B_{C2}-doped g-C_9N_{10} (c), B_{C3}-doped g-C_9N_{10} (d), B_{N1}-doped g-C_9N_{10} (e), B_{N2}-doped g-C_9N_{10} (f), B_{N3}-doped g-C_9N_{10} (g), and B_A-doped g-C_9N_{10} (h).

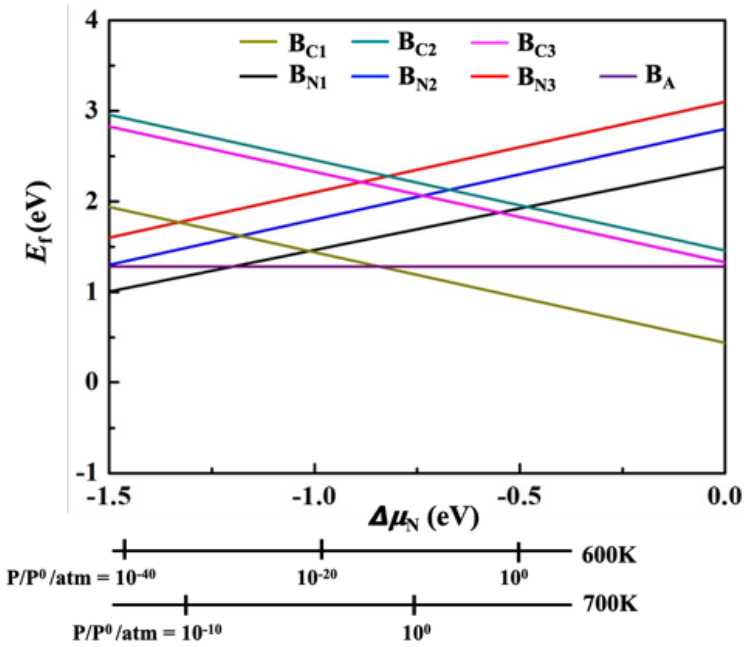

Figure 4.2: The formation energy of seven B-doped g-C_9N_{10} structures as a function of N chemical potential. $\Delta\mu_N = 1/2(\mu_{N2} - E_{N2})$ where E_{N2} is the total energy of a gas-phase N_2 molecule at 0 K. The bottom axes show the corresponding N_2 chemical potentials at the absolute temperature T and partial pressure P (with $P° = 1$ atm), $\mu_{N2} = H°(T) - H°(0) - TS°(T) + k_BT\ln(P/P°)$, where the enthalpy $H°$ and the entropy $S°$ are obtained from [44].

To investigate the feasibility of experimental synthesis of g-C_9N_{10} and B_{C1}, B_{N1}, and B_A-doped g-C_9N_{10} structures, I calculated the cohesive energies (E_{coh}) of B_{C1}, B_{N1}, B_A-doped g-C_9N_{10}, g-C_9N_{10}, g-C_3N_4, C_3N_5, and g-CN, E_{coh} is defined as follows:

$$E_{\mathrm{coh}} = \frac{E_{\mathrm{total}} - \sum N_{\mathrm{Z}} \times \mu_{\mathrm{Z}}}{\sum N_{\mathrm{Z}}} \tag{4-13}$$

where E_{total} is the total energy of B-doped C_9N_{10}, g-C_9N_{10}, g-C_3N_4, and g-C_3N_5. N_Z and μ_Z are the numbers of atoms and the energy of an isolated atom for element Z species (Z = C, N, and B), respectively. I found that the E_{coh} of g-C_3N_4, C_3N_5, and g-CN, which have been synthesized experimentally [11,12,46], were calculated to -6.03 and -5.78, and -6.11 eV per atom, respectively (Table 4.1). And the E_{coh} of g-C_9N_{10} is -6.11 eV per atom, which is more stable than g-C_3N_4 and C_3N_5 and has similar stability with g-CN. For doping structures, the stable order is B_{N1} (-6.11 eV per atom) ≈ B_A (-6.11 eV per atom) > B_{C1}(-6.08 eV per atom). Zhao *et al.* assumed a feasible synthetic method for g-C_9N_{10}, in which commercially available heptazine chloride ($C_6N_7Cl_3$) and cyanuric chloride ($C_3N_3Cl_3$) serve as precursors to react with Na via a simple solvothermal process, similar to the g-CN synthetic method [47]. Therefore, it proved that the existence and synthesis of g-C_9N_{10} and three doping structures are highly possible. For AIMD simulation, when the temperature increases to 500 K, the structure remains well and no distortion (Figure 4.3). It proves that three B-doped C_9N_{10} structures are all locally stable. Therefore, I assume three B-doped structures can be synthesized in the near future.

Table 4.1: The cohesive energies of g-C_3N_4, C_3N_5, g-CN, g-C_9N_{10}, B_{C1}-doped g-C_9N_{10}, B_{N1}-doped g-C_9N_{10} and B_A-doped g-C_9N_{10}.

	E_{coh}(eV/atom)
g-C_3N_4	−6.03
C_3N_5	−5.78
g-CN	−6.11
g-C_9N_{10}	−6.11
B_{C1}-doped g-C_9N_{10}	−6.08
B_{N1}-doped g-C_9N_{10}	−6.11
B_A-doped g-C_9N_{10}	−6.11

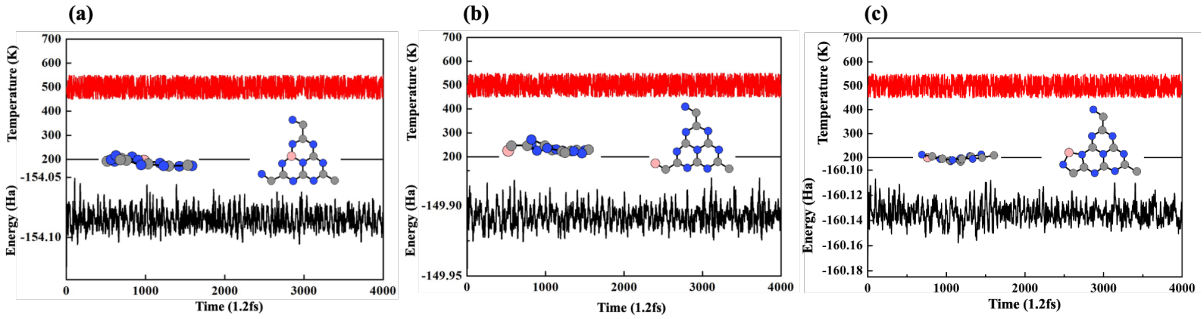

Figure 4.3: Variations of temperature and energy against time for *ab initio* molecular dynamics (AIMD) simulations of the B_{C1} (a), B_{N1} (b), and B_A-doped g-C_9N_{10} (c). The insets show top and side views of the snapshot of the atomic configuration. The simulation is run at 500 K for 4.8 ps with a time step of 1.2 fs.

4.3.2 N_2 Adsorption and N_2 Fixation

Firstly, N_2 adsorption is a prerequisite step in the whole N_2RR, the premise of N_2RR is that N_2 needs to be chemisorbed on the surface. N_2 can adsorb on the surface with two different configurations, i.e., side-on in which two N atoms interact with the surface and end-on in which

one nitrogen binds to the active site. For B_{C1}, the N_2 molecule is physisorbed at B site due to the large B–N distance (3.298 Å, Table 4.2). Therefore, B_{C1}-doped g-C_9N_{10} cannot be N_2RR catalysts. For B_{N1} and B_A-doped g-C_9N_{10}, the adsorption energies of N_2 in side-on and end-on configurations are shown in Table 4.2. N_2 adsorbed on B_{N1} only has an end-on configuration with an adsorption energy of −1.53 eV, while N_2 adsorbed on B_A has two different end-on and side-on configurations with E_{ads} values of −1.48 eV and −0.91 eV, respectively. Moreover, the strong adsorption of N_2 on the surface elongates the N≡N bond length from 1.108 Å in gas-phase N_2 to 1.127 Å (end-on configuration on B_{N1}), 1.136 Å (end-on configuration on B_A), and 1.217 Å (side-on configuration on B_A), respectively, indicating they can remarkedly activate the N≡N bond. However, in B_A cases, I found that N_2 is preferably adsorbed in the end-on configuration than the side-on one by a large energy difference of 0.57 eV and the transition from end-on to side-on N_2 requires a barrier of 1.00 eV by CI-NEB [48,49] as shown in Figure 4.4). Therefore, I only consider the N_2RR via N_2 adsorbed in the end-on configuration on B_{N1} and B_A cases. Electronic analysis of N_2 adsorption on both cases will be discussed in following section.

Table 4.2: The calculated bond length B–N and N–N, adsorption energies (E_{ads}) of end-on N_2 on B_{N1} (B_{C1})-doped g-C_9N_{10} and end-on N_2 (side-on N_2) on B_A-doped g-C_9N_{10}, respectively.

	Bond length (B–N) Å	Bond length (N–N) Å	E_{ads} (N_2/S) eV	E_{int} (N_2/S) eV	E_{def} (N_2) eV	E_{def} (S) eV
N_2 gas	—	1.108	—	—	—	—
B_{C1}	3.298	1.114	−0.05	—	—	—

B_{N1}	1.468	1.127	−1.53	−1.91	0.01	0.40
B_A	1.429	1.136	−1.48	−1.56	0.04	0.04
	(1.558)	(1.217)	(−0.91)	—	—	—

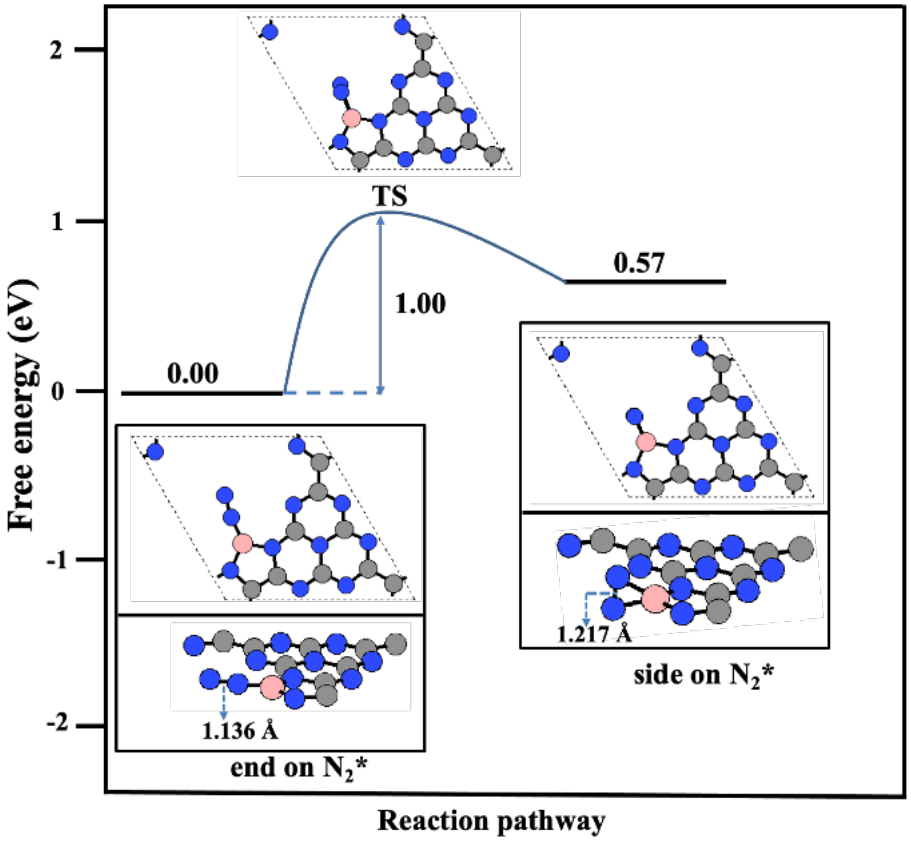

Figure 4.4: Free energy barrier diagram of N_2 rotation process on B_A-doped g-C_9N_{10} (end on N_2* → side on N_2*).

I investigated the five possible N_2RR pathways [50-52] starting by end-on N_2 adsorption, including alternating, distal, Mixed I, Mixed II, and Mixed III pathways (Figure 4.5 (a)). For B_{N1}-doped g-C_9N_{10}, the free energies of all intermediates were computed (Figure 4.5 (b), Figure B.1, and Table B.2). For all pathways, the first hydrogenation step is N_2* → NNH* with endergonicity of 0.62 eV. As for the second step, the NNH* is hydrogenated by proton-electron

pairs ($H^+ + e^-$) to NHNH* with ΔG of -0.12 eV in alternating and Mixed III pathways, while in the other three pathways, NNH* is hydrogenated to NH_2N* with ΔG of -0.75 eV. In the distal pathway, the third step is the $NH_2N^* \rightarrow N^* + NH_3$ with endergonicity of 0.37 eV. N* is hydrogenated by $2(H^+ + e^-)$ spontaneously to NH_2*. Except for the second step, alternating and Mixed I pathways have the same intermediates with all spontaneous steps. In Mixed II and Mixed III pathways, I found NH_2NH* can be also hydrogenated to NH* with the release of one NH_3 rather than NH_2NH_2* (alternating pathway and Mixed I pathway). The rate-determining step on B_{N1} doped g-C_9N_{10} is $N_2^* \rightarrow NNH^*$ with ΔG of 0.62 eV and U_L of -0.62 V in five pathways. Even though U_L of the five pathways is the same, the Mixed I pathway ($N_2^* \rightarrow NNH^* \rightarrow NH_2N^* \rightarrow NH_2NH^* \rightarrow NH_2NH_2^* \rightarrow NH_2^* \rightarrow NH_3^*$) is the most thermodynamically favorable pathway among the five paths because of the lowest free energy in each step (Figure 4.5 (b)).

Similarly, N_2RR on B_A-doped g-C_9N_{10} preferably proceeds via the Mixed I mechanism with the lowest free energy steps as shown in Figure 4.5 (c), Figure B.2, and Table B.3. The rate-determining step (RDS) of Mixed I pathway is the final step ($NH_2^* \rightarrow NH_3^*$) with endergonicity of 0.44 eV and U_L of -0.44 V. I found that the RDS of N_2RR on B_A case ($NH_2^* \rightarrow NH_3^*$) is different from that on B_{N1} case ($N_2^* \rightarrow NNH^*$) due to stronger binding of NNH*. Compared with benchmark ΔG_{RDS} of N_2RR on Ru (0001) (1.08 eV) [53], the N_2RR activity on B_{N1} and B_A-doped g-C_9N_{10} shows significant improvement.

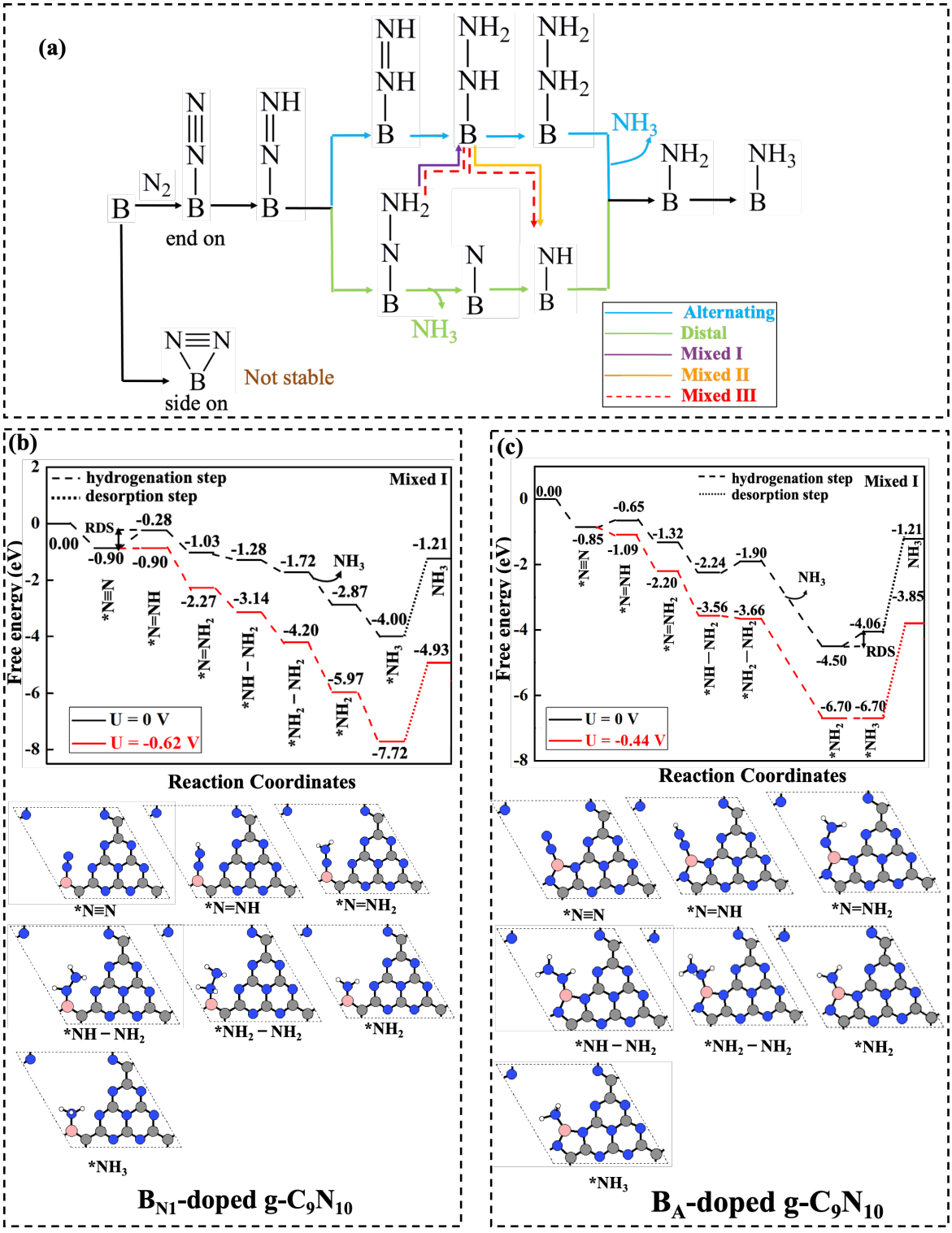

Figure 4.5: (a) Schematic depiction of distal, alternating, enzymatic, and Mixed mechanisms for N_2RR. (b) Free energy diagrams for optimal N_2 reduction pathway on B_{N1}-doped g-C_9N_{10} through Mixed I mechanisms with the optimized structure of every intermediate. (c) Free

energy diagrams for optimal N_2 reduction pathway on B_A-doped g-C_9N_{10} through enzymatic mechanism with the optimized structure of every intermediate.

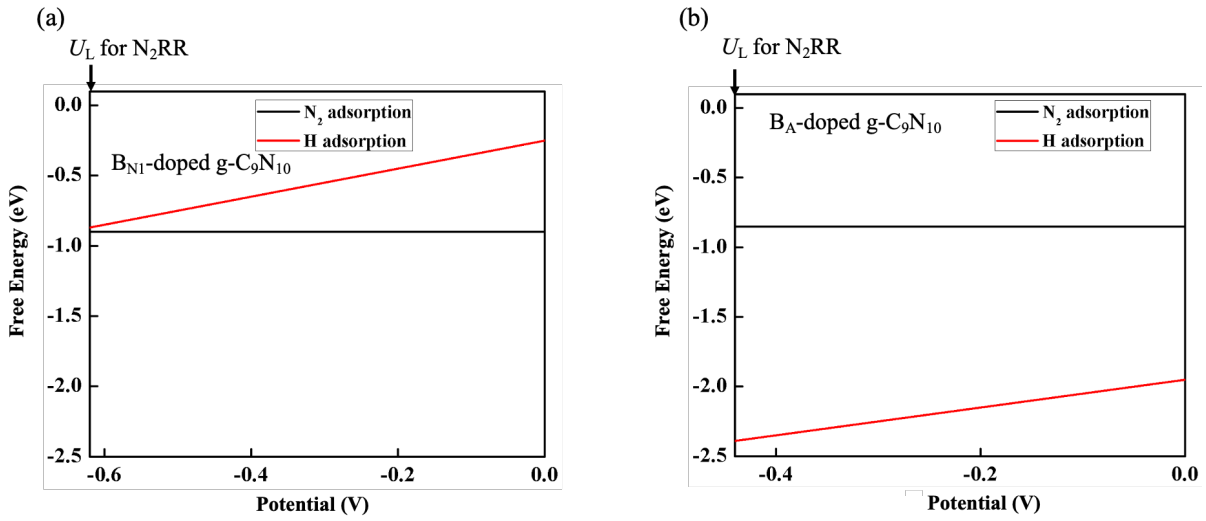

Figure 4.6: The relationship between applied potential (V) and free energy (eV) of H adsorption and N_2 adsorption at B site on B_{N1}-doped g-C_9N_{10} (a) and B_A-doped g-C_9N_{10} (b).

4.3.3 H Poisoning and Hydrogen Evolution Reaction

H poisoning by blocking the active site and competing hydrogen evolution reaction (HER) will decrease the selectivity and the Faraday efficiency of N_2RR significantly. Thus, suppressing H adsorption can be a reasonable way to increase N_2RR selectivity and to improve the N_2RR activity. ΔG of H* and N_2* on B site as a function of applied potential are shown in Figure 4.6. For B_{N1}-doped g-C_9N_{10}, under U = 0 V, the ΔG of H adsorption at the B site is -0.25 eV, which is more positive than that of N_2*(-0.9 eV), and I found that the stable adsorption sites of H and N_2 are different in the case of B_{N1} (Figure 4.7 (a)-(b)). As shown in Figure 4.6 (a), ΔG(*H) is still more positive than ΔG(*N_2) until the applied potential is set to the U_L for N_2RR on B_{N1}-doped g-C_9N_{10}. Furthermore, the U_L of HER is -0.89 V in the N_3 site (Figure 4.7 (a)) which is more negative than the U_L of N_2RR (-0.62 V). Both prove that B_{N1}-doped g-C_9N_{10} has superior N_2RR selectivity. For B_A-doped g-C_9N_{10}, under U = 0 V, the

computed free energy of H adsorption on the B site is −1.95 eV (Figure 4.6 (b)), which is more negative than that of N_2* adsorption ($\Delta G = -0.85$ eV), hence the H* adsorption at B site is more favorable than N_2 adsorption when H^+ and N_2 present together, indicating the strong poisoning effect by H.

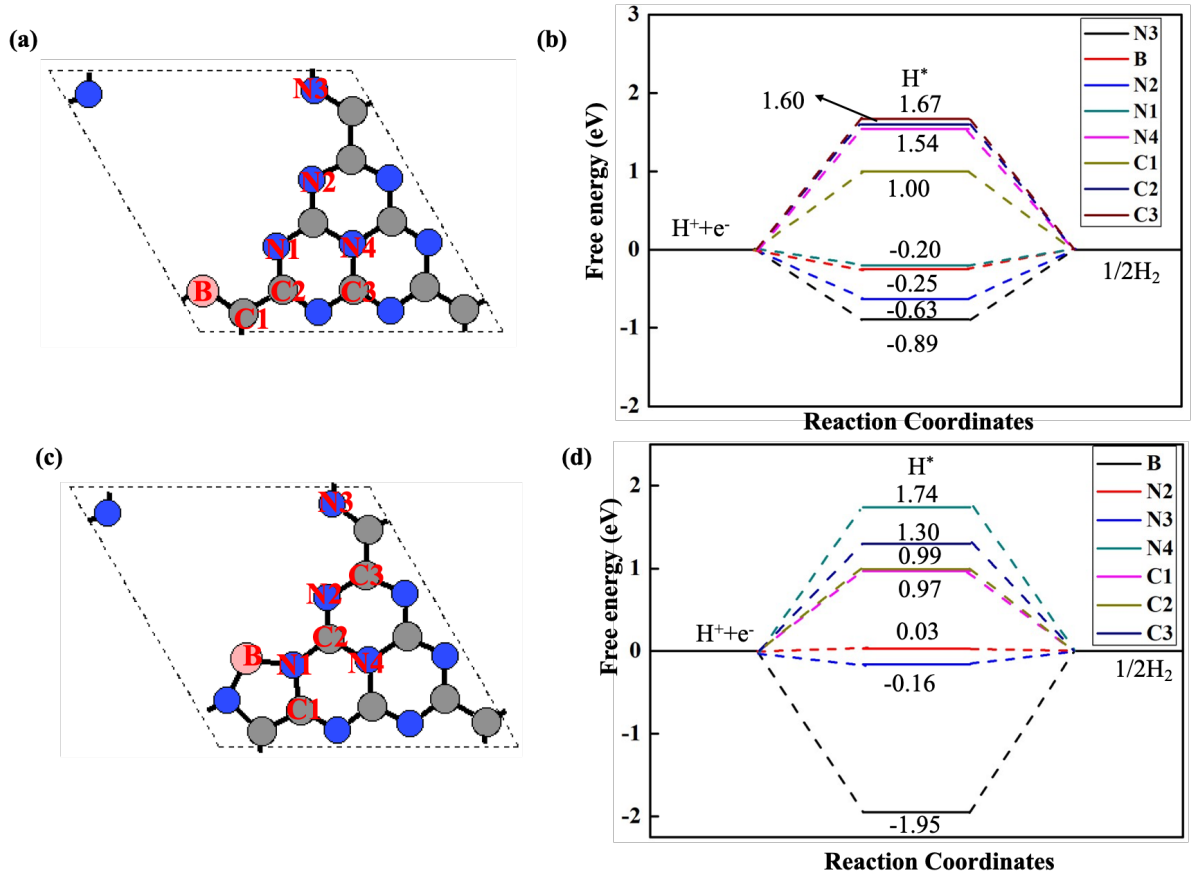

Figure 4.7: The eight possible H adsorption sites on B_{N1}-doped *g*-C_9N_{10} (a) and B_A-doped g-C_9N_{10} (c). The pink, blue, and gray balls denote boron, nitrogen, and carbon atoms, respectively. The Gibbs free energy profile of hydrogen evolution reaction (HER) of B_{N1}-doped *g*-C_9N_{10} (b) and B_A-doped g-C_9N_{10} (d). H adsorption on the N1 site of B_A-doped g-C_9N_{10} broke the structure, so it is not shown in HER diagram.

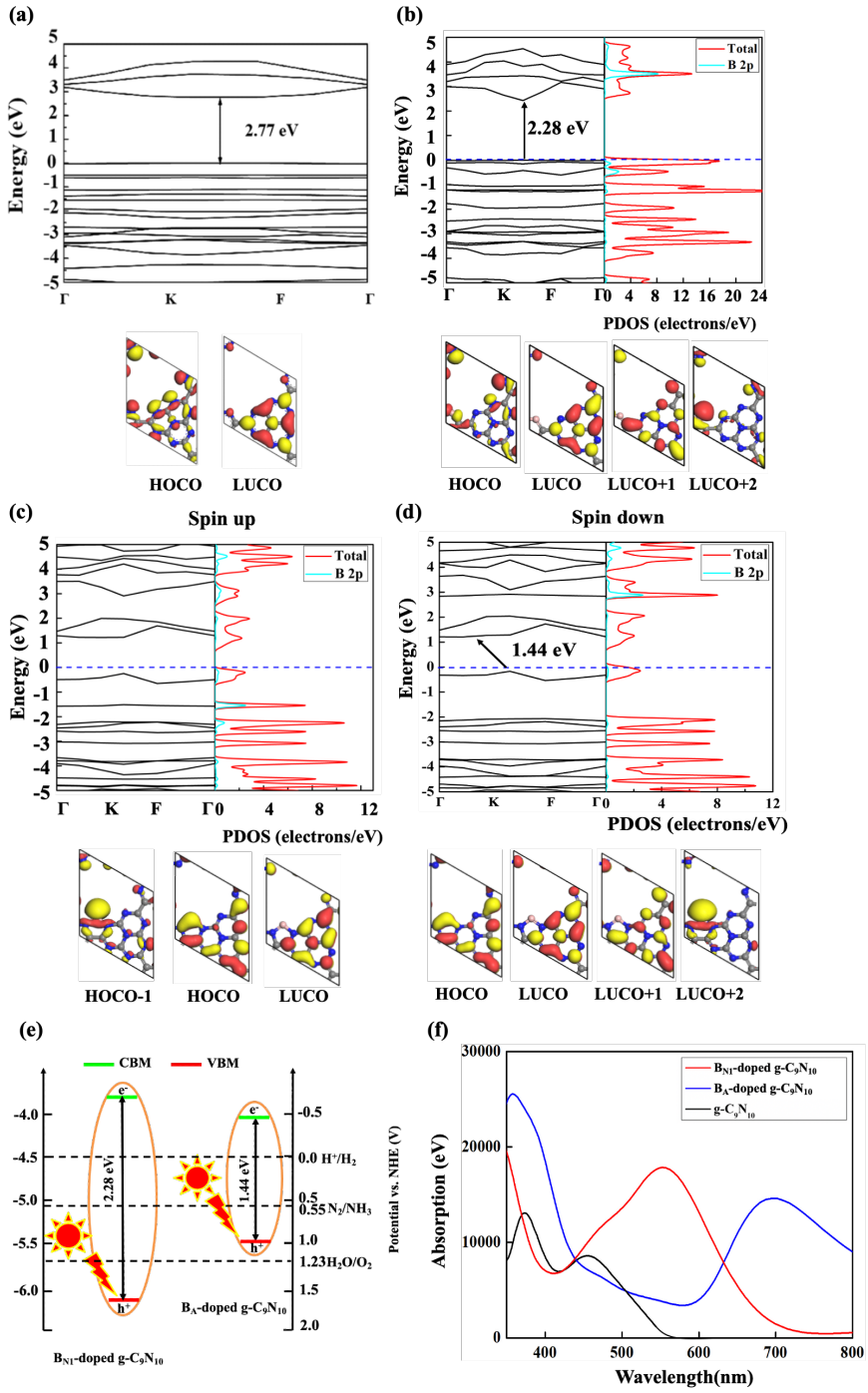

Figure 4.8: Band structure, HOCO and LUCO distributions of g-C_9N_{10} (a); the band gap, PDOS, HOCO and LUCO distributions of B_{N1}-doped g-C_9N_{10} (b); the band gap, PDOS, HOCO and LUCO distributions of B_A-doped g-C_9N_{10} on spin up channel (c) and on spin down channel (d), orbitals plots come from individual Bloch states; The theoretical energy position of conduction band minimum (CBM) and valence band maximum (VBM) on B_{N1}-doped g-C_9N_{10}

and B_A-doped g-C_9N_{10}, respectively in vacuum (e); Absorption spectra of g-C_9N_{10} and B_{N1}-doped g-C_9N_{10} and B_A-doped g-C_9N_{10} (f).

4.3.4 Photocatalytic Activity of B_{N1}-doped g-C_9N_{10} and B_A-doped g-C_9N_{10}

First, I analyze the electronic structure of B_{N1}-doped g-C_9N_{10} and B_A-doped g-C_9N_{10} via band structure, and projected density of state (PDOS) using HSE06 functional as implemented in the CASTEP package. As shown in Figure 4.8 (a), the computed band gap of g-C_9N_{10} is 2.77 eV, being consistent with previous work [15, 46, 54], and slightly smaller than that for g-C_3N_4 (2.81 eV) [40] by HSE06 functional. The band gaps of B_{N1}-doped g-C_9N_{10} decrease to 2.28 eV (Figure 4.8 (b)), which is a suitable band gap for N_2RR photocatalyst (the ideal band gap value is close to 2.0 eV [55]). For B_A-doped g-C_9N_{10}, I obtain an indirect band gap of 1.44 eV, where the system has an unpaired electron at the second highest occupied crystal orbital (HOCO−1) in the spin up channel (Figure 4.8 (c)). Wave functions plot and PDOS indicate that the unpaired electron at HOCO−1 originates from an occupied $2p_y$ orbital of B atom in spin up channel. I found that the HSE06 functional stabilizes the localized state of B 2p as HOCO−1 in the spin up channel whereas this state is shifted upward near the highest occupied crystal orbital (HOCO) state (Figure B.3 (b)) using GGA/PBE functional due to the self-interaction error [56]. In contrast, B_{N1}-doped g-C_9N_{10} exhibits no spin polarization due to stronger hybridization with neighbouring C atoms.

Under light illumination of semiconductors, electrons are generated in the conduction band (CB) while holes are generated in the valence band (VB). The generated holes can oxidize water, and conduction band electrons will reduce nitrogen [57]. In principle, the photocatalytic activity for N_2RR reactions is determined by the relative position of the N_2/NH_3 reduction potential (0.55 vs. NHE), H_2O/O_2 oxidation potential (1.23 vs. NHE), and the conduction and

valence band positions of the semiconductor [57]. To be specific, the CB minimum (CBM) of the semiconductor should be more negative than the reduction potential of N_2/NH_3, and the VB maximum (VBM) should be more positive than the H_2O/O_2 oxidation potential. In this work, the CBM and VBM relative to the normal hydrogen electrode potential (NHE) were calculated by the band gap center (BGC) calculations at the semiconductor/vacuum interface [58]. This assumes that the band edge positions of a material stay the same before and after contact with the solution. In the present work, we report the CBM and VBM of B-doped g-C_9N_{10} under vacuum conditions. It should be noted that the presence of solution will change the positions of VBM and CBM and this will be investigated in my upcoming work. The potential of CBM (U_{CBM}) and VBM (U_{VBM}) relative to the NHE are calculated using the following equations [58-59]:

$$E_{\mathrm{BGC}} = \frac{(\varepsilon_{\mathrm{VBM}} + \varepsilon_{\mathrm{CBM}})}{2} - \varepsilon_{\mathrm{Vacuum}} \tag{4-14}$$

$$E_{\mathrm{VBM}} = E_{\mathrm{BGC}} - \frac{1}{2}E_{\mathrm{g}} \tag{4-15}$$

$$E_{\mathrm{CBM}} = E_{\mathrm{BGC}} + \frac{1}{2}E_{\mathrm{g}} \tag{4-16}$$

$$U_{\mathrm{CBM/VBM}} = -E_{\mathrm{CBM/VBM}} - E_{\mathrm{e}} \tag{4-17}$$

where $\varepsilon_{\mathrm{VBM/CBM}}$ is the Kohn-sham eigenvalue of the highest occupied/the lowest unoccupied state, $\varepsilon_{\mathrm{Vacuum}}$ is the vacuum level with defined as average electrostatic potential at center of vacuum region. E_{g} is the band gap by HSE06, E_{e} is the energy of free electrons on the hydrogen scale (ca. 4.5 eV [60]).

As shown in Figure 4.8 (e), the CBM of B_{N1}-doped g-C_9N_{10} and B_A-doped g-C_9N_{10} are at -0.65 and -0.45 V, which are more negative than the N_2/NH_3 potential (0.55 V) and which are more negative than the calculated limiting potential of N_2RR on BN_1 (-0.62 V) and B_A-doped g-C_9N_{10} (-0.44 V), it indicates that at U_{CBM}, all elementary steps along the five pathways of N_2RR on two photocatalysts are exothermic, denoting the spontaneous reduction reaction

under light irradiation [61,62]. On the other hand, the VBM of B_{N1}-doped g-C_9N_{10} is at 1.63 V which is more positive than the H_2O/O_2 potential (1.23 V), while the VBM of B_A-doped g-C_9N_{10} is at 0.99 V which is below the H_2O/O_2 potential (1.23 V), indicating that B_A-doped g-C_9N_{10} as photocatalyst for N_2RR need a sacrificial agent to complete the whole reaction. However, B_{N1}-doped g-C_9N_{10} can be a photocatalyst for N_2RR without a sacrificial agent.

Finally, I explore the optical properties of B_{N1}-doped g-C_9N_{10} and B_A-doped g-C_9N_{10} by absorption spectra calculations. As shown in Figure 4.8 (f), the strong absorption peak of B_{N1}-doped g-C_9N_{10} and B_A-doped g-C_9N_{10} red-shifts and has a large overlap with visible light (about 400-780 nm) compared with pure g-C_9N_{10}, indicating that introduction of B atom can increase the absorption light ability. Moreover, I also found that the separation of photogenerated e^-/h^+ pairs are also possible as shown in the spatial distribution of the HOCO and the lowest unoccupied crystal orbital (LUCO) of g-C_9N_{10}, B_{N1}-doped g-C_9N_{10} and B_A-doped g-C_9N_{10} in Figure 4.8. The HOCO and LUCO of g-C_9N_{10} are mostly located on the same C and N atoms. For B_{N1}-doped g-C_9N_{10} and B_A-doped g-C_9N_{10}, HOCOs are mostly located at B atoms, while LUCOs are mostly located at C and N atoms, resulting in spatial separation of those states. Thus, I assume that B_{N1}-doped g-C_9N_{10} and B_A-doped g-C_9N_{10} have better ability to separate the photogenerated e^-/h^+ pairs. Together with the results that show B_{N1}-doped g-C_9N_{10} has a good catalytic activity and selectivity towards N_2RR in previous sections, I expect that B_{N1}-doped g-C_9N_{10} might be used as a photocatalyst for N_2 fixation driven by Solar light.

4.3.5 The N_2 Activation and H Adsorption on B_{N1}-doped g-C_9N_{10} and B_A-doped g-C_9N_{10} Surface: Influence of Chemical Environments on Adsorption Strength

In the previous section, I found that the adsorption energy of end-on N_2 on B_{N1}-doped g-C_9N_{10} is almost the same as that on B_A-doped g-C_9N_{10} with the energy difference of 0.05 eV

(Table 4.2), while H adsorption energy of B_{N1}-doped g-C_9N_{10} is significantly weaker than that of B_A-doped g-C_9N_{10} by 1.7 eV. To shed light on the different behavior of H and N_2 adsorption on B_{N1} and B_A, I perform the bonding analysis by a combination of energy decomposition and electronic structure using the atomic orbital local density of states (AOLDOS) [63-65] of B atom on both clean surfaces, N_2 adsorption on both surfaces and H adsorption on both surfaces; Projected density of states into crystal orbitals (PDOS) [63-65] and crystal orbital overlap population (COOP) [63-65] of adsorbed N_2 on both surfaces.

I begin with the bonding mechanism of N_2 with B atoms of B_{N1} and B_A. Energy decomposition analysis shown in Table 4.2 enables me to clarify the roles of chemical bonding between N_2 and surface, N_2 bond elongation, and surface deformation upon the adsorption via E_{int}, $E_{def}(N_2)$, and $E_{def}(S)$, respectively. As shown in Table 4.2, adsorbed N_2 has a stronger interaction with B_{N1} compared to that with B_A due to more negative E_{int} (−1.91 vs. −1.56 eV). Moreover, E_{def} (N_2) of B_A-doped g-C_9N_{10} is more positive than that of B_{N1}-doped g-C_9N_{10} (0.04 eV vs. 0.01 eV) because of the more elongation of N_2 bond length in B_A case. However, the energy required to deform the B_{N1} surface upon the N_2 adsorption is significantly higher than that to deform the B_A case upon the N_2 adsorption. The more positive energy to deform the B_{N1} surface upon the N_2 adsorption can be explained by the fact that the adsorbed N_2 molecule causes stronger repulsive interaction with neighboring N atoms of B_{N1} due to the steric hindrance as shown in the smaller distance between N_2 and neighboring N atoms (Figure 4.9 (a) and (f)) compared with that of B_A case (2.63 Å/2.65 Å vs. 2.89 Å/3.14 Å). Consequently, this deformation energy difference compensates for the stronger chemical interaction between N_2 and surfaces, leading to similar adsorption energies of N_2 in both cases.

The chemical bonding of N_2 with B_{N1} and B_A is revealed by electronic structure analysis. Firstly, from AOLDOS in Figure 4.9 (b), the $2p_y$ orbital is unoccupied in B_{N1} as shown by the wave function of LUCO+2 in Figure 4.8 (b). In contrast, from AOLDOS in Figure 4.9 (g), the

$2p_y$ orbital is singly occupied in B_A as also shown by the wave function of HOCO−1 in Figure 4.8 (c). In B_{N1}, the $2p_z$ orbital is partially occupied as shown in a localized AOLDOS peak at $E_f - 2$ eV, while the $2p_z$ orbital is delocalized arising from hybridization with $2p_z$ of N atoms shown by the wave function of HOCO in Figure 4.8 (c). N_2 chemisorption on the surface arises from "σ donation-π backdonation" process with B 2p orbitals. As shown in Figure 4.9 (c)-(e) and 4.9 (h)-(j), The σ donation arises from hybridization between bonding orbitals (σ) of N_2 and B unoccupied $2p_y$ orbital of both cases, and the backdonation arises from hybridization between the antibonding orbitals (π*) of N_2 and occupied B $2p_z$ orbital for both cases. Even though $2p_z$ orbital of B_A case is delocalized due to hybridization with $2p_z$ of N atoms, the singly occupied $2p_y$ state would induce the hybridization of $2p_z$ orbital and π* of N_2 as shown in the resonance peak at $E_f - 1$ eV. Therefore, the indirect backdonation process between the $2p_z$ orbital of B and π* of N_2 in B_A results in weaker interaction energy compared with the direct backdonation process between the $2p_z$ orbital of B and π* of N_2 in B_{N1}.

The chemical bonding of H with B_{N1} and B_A is then investigated. As shown in Figure 4.10, the interaction between H and B atoms arises from the weak hybridization between $2p_y$ of B and s orbital of H as shown by a small resonance peak at $E_f - 4.0$ eV for B_{N1}-doped g-C_9N_{10} (Figure 4.10 (b)). For B_A-doped g-C_9N_{10} (Figure 4.10 (d)), hybridization between $2p_y$ of B and s orbital of H becomes stronger as shown by resonance peak at $E_f - 5.0$ eV leading to the stronger H–B interaction. The $2p_y$ orbital of B is fully unoccupied in B_{N1} (as shown by the wave function of LUCO+2 in Figure 4.8 (b) and Figure 4.10 (a)), in contrast, it is half-filled with one unpair electron at the spin-up channel in the case of B_A (as shown by wave function of HOCO–1 in Figure 4.8 (c) and Figure 4.10 (c)). Therefore, the hybridization between $2p_y$ of

B atom and 1s of H atom is facilitated in the case of B_A, resulting in stronger H adsorption over N_2 adsorption.

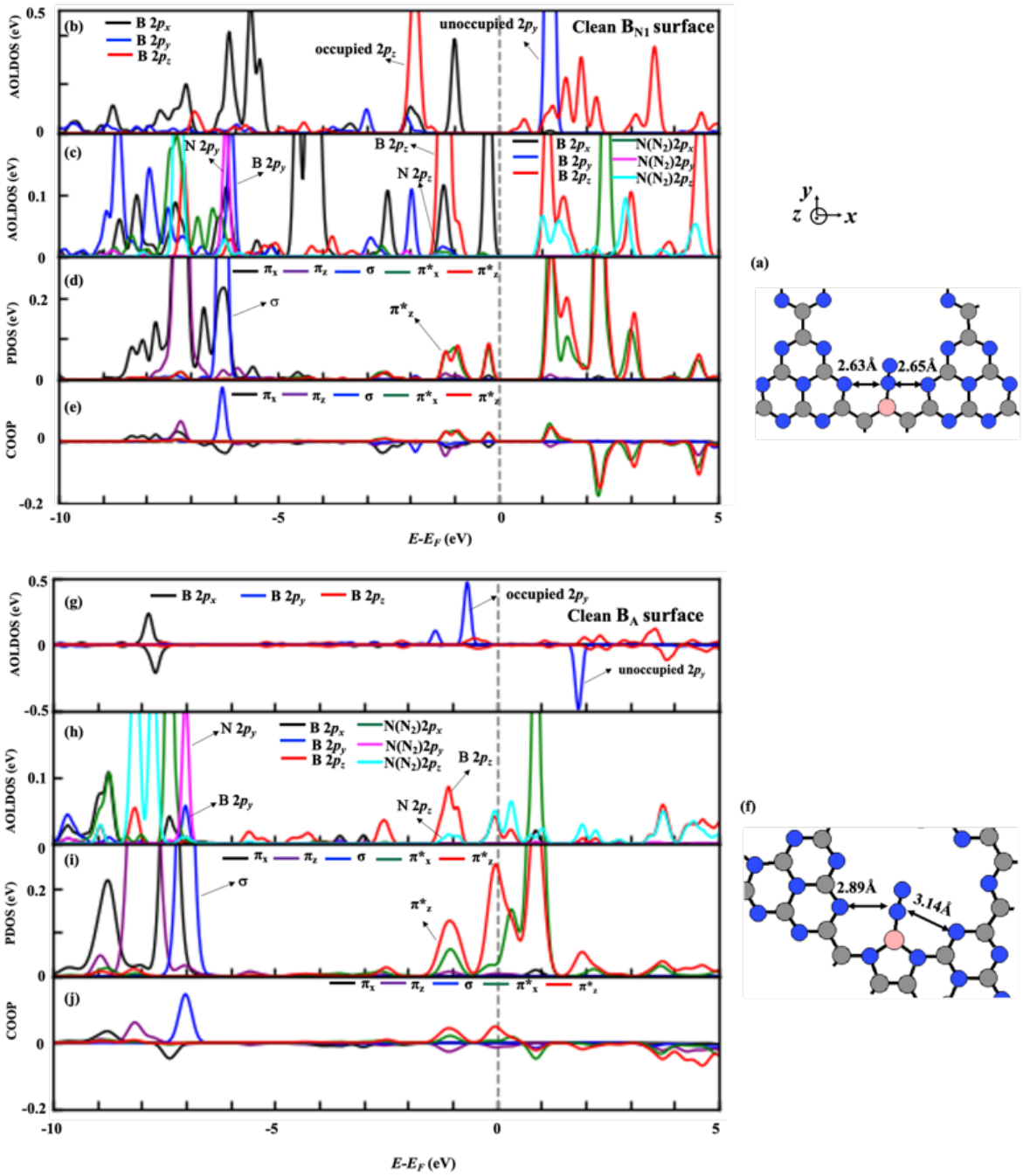

Figure 4.9: (a) The structure of N_2 adsorption on B_{N1}-doped g-C_9N_{10}; (b)AOLDOS of B atom in B_{N1}-doped g-C_9N_{10}, (c) AOLDOS of B atom in end on N_2 adsorption on B_{N1}-doped g-C_9N_{10}, (d) PDOS and (e) COOP of end on N_2 on B_{N1}-doped g-C_9N_{10}; (f) The structure of N_2 adsorption on B_A-doped g-C_9N_{10}; (g) AOLDOS of B atom in B_A-doped g-C_9N_{10} in spin up and spin down;

(h) AOLDOS of B atom in end on N_2 adsorption on B_A-doped g-C_9N_{10}; (i) PDOS and (j) COOP of end on N_2 on B_A-doped g-C_9N_{10}.

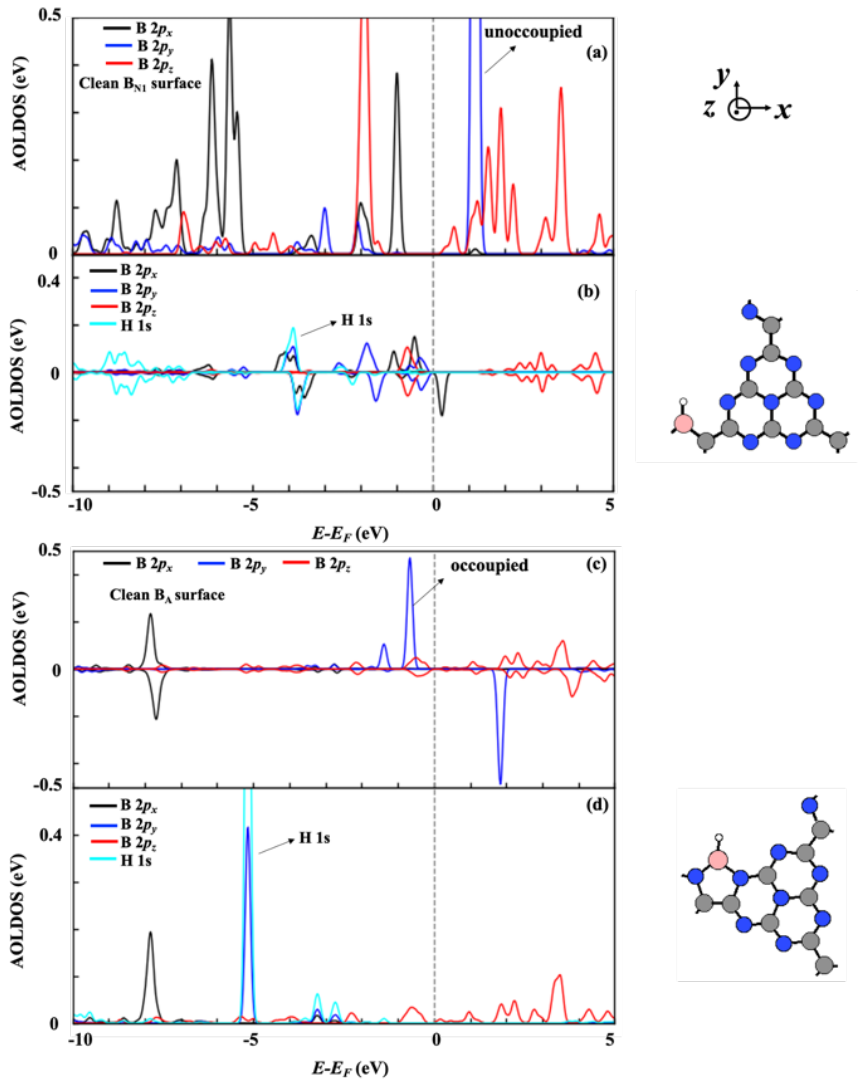

Figure 4.10: (a) AOLDOS of B atom in B_{N1}-doped g-C_9N_{10}, (b) AOLDOS of B atom in H adsorption on B_{N1}-doped g-C_9N_{10} in spin up and spin down; (c) AOLDOS of B atom in B_A-doped g-C_9N_{10} in spin up and spin down, (d) AOLDOS of B atom in H adsorption on B_A-doped g-C_9N_{10}.

4.3.6 Comparison with Other Reported B-based Catalysts

From previous sections, by using three screening aspects, i.e., N_2 adsorption ability; U_L of N_2RR; and HER and H poisoning; I found that B_{N1}-doped g-C_9N_{10} exhibits good N_2RR activity and selectivity due to lower U_L of N_2RR and weaker H adsorption over N_2 adsorption.

However, NH_3 poisoning may be a problem on some catalysts. In general, NH_3* should be desorbed or hydronated to NH_4^+ in the solvent before the next N_2 adsorption. I found that although B_{N1}-doped g-C_9N_{10} exhibits quite high N_2RR catalytic activity and selectivity, the second NH_3* desorption on B_{N1} or B_A-doped g-C_9N_{10} surface is difficult because of large free energies (Table B.2 and B.3). From my literature review for N_2 fixation on B-based materials (Table 4.3), I found that NH_3 poisoning is a common problem for N_2 fixation on B-doped CN materials. It was found that the increase in the N_2 adsorption strength results in an increase in the NH_3 adsorption, thus reducing the NH_3 desorption ability. It was also found that Boron nanosheet and B_4C (110) also suffer from NH_3 poisoning as shown in DFT calculation, however, experimental data shows these catalysts can have quite high N_2 fixation ability [70-71]. In addition, B-doped g-C_3N_4 faces a similar NH_3 poisoning problem, but experimentally it was shown that it can be a good N_2 fixation catalyst [72]. These observations indicated that we have not yet fully clarified the NH_3* desorption process theoretically. It was proposed that by increasing the NH_3 coverage, NH_3 poisoning problem is mitigated, namely, the desorption energy of NH_3* is decreased from 2.54 eV to 1.11 eV on the B nanosheet [70]. Note that, the desorption of NH_3* is not an electron transfer process, and therefore it does not affect the limiting potential.

Aside from NH_3 poisoning, I would like to mention that the H poisoning of B-doped CN materials. From Table 4.3, it was found that most of B anchored CN catalysts have stronger H poisoning effect [66-68], while by changing the B-doped configuration to B replacement at N site, i.e., B_{N1}-doped g-C_9N_{10}, can effectively inhibit the H poisoning.

Table 4.3: Comparison of ΔG (N_2*), ΔG (H*) and desorption free energy (ΔG_{des}) of NH_3*on B site, U_L, RDS step and program (functional) for our work with other reported B-based catalysts.

System	ΔG (N_2*)/eV	ΔG (H*)/eV	ΔG_{des} (*NH_3*)/eV	U_L/V	RDS step	Program (Functional)	Refs
B_{N1}-doped g-C_9N_{10}	−0.90	−0.25	2.79 eV	−0.62 (mix I)	N_2* → NNH*	STATE (GGA/PBE+D2)	This work
B_A-doped g-C_9N_{10}	−0.85	−1.95	2.85 eV	−0.44 (mix I)	NH_2* → NH_3*	STATE (GGA/PBE+D2)	This work
B_A-doped g-C_3N_4	−0.76	—	1.80 eV	−0.87 (distal)	NH_2* → NH_3*	VASP (GGA/PBE)	[23]
B_A-doped g-C_9N_{10}	−0.95	−2.28	3.00 eV	−0.38 (alternating)	NH_2* → NH_3*	VASP (GGA/PBE+D3)	[46]
B_A-doped g-C_3N_4	−0.41	−0.64	—	−0.89 (alternating)	NH_2* → NH_3	VASP (GGA/PBE+D3)	[66]
B@N doped g-C_3N_4	0.06	−0.37	—	−1.34 (alternating)	N_2* → NNH*	VASP (GGA/PBE+D3)	[66]
B_A-doped g-C_6N_6	−0.78	−2.54 (E_{ads})	2.20 eV	−0.38 (alternating)	N_2* → NNH*	VASP (GGA/PBE)	[67]
B_A-doped g-C_2N	−0.99	−2.40 (E_{ads})	3.72 eV	−0.80 (alternating)	N_2* → NNH*	$Dmol^3$ (GGA/PBE+D2)	[68]
B_A-doped C_9N_4	−0.73	−0.21	3.22 eV	−0.72 (alternating)	N_2* → NNH*	VASP (GGA/PBE+D3)	[69]
Boron Nanosheet[a]	−0.66	0.23	2.54 eV	−0.80 (distal)	NH_2* → NH_3*	VASP (GGA/PBE+D3)	[70]
B_4C (110)[a]	−0.41	—	1.73 eV	−0.34 (alternating)	NH_2NH_2* → NH_2NH_3*	$Dmol^3$ (GGA/PBE+D2)	[71]

[a] This catalyst has been synthesized and proved that it can become a better N_2 fixation catalyst by experiment.

4.4 Summary

In summary, I have systematically investigated N_2RR on B-doped C_9N_{10} with three doping configurations, i.e., B substituted N (B_{N1}), B substituted C (B_{C1}), and B anchored (B_A) on g-C_9N_{10}. The stability of different doping sites is evaluated and B_{N1} (B_{C1}) is stable at N-poor (rich) conditions. I found that N_2 is chemisorbed on B_{N1} and B_A sites by "σ donation-π back donation" processes. The free energy calculations show that B_{N1} and B_A-doped g-C_9N_{10} proceed via Mixed I mechanism starting from the stable end-on N_2 with low limiting potentials of -0.62 V and -0.44 V, respectively. Importantly, H blocks active site in the case of B_A-doped g-C_9N_{10}, resulting in lower N_2RR selectivity, while B_{N1}-doped g-C_9N_{10} can effectively prevent the H poisoning due to the weaker H adsorption relative to N_2 adsorption, thus improving the N_2RR activity and selectivity. Moreover, the electronic structure analysis showed that fully unoccupied $2p_y$ orbital of B_{N1} case effectively inhibits H adsorption, while singly occupied $2p_y$ of B_A case causes stronger binging with H, resulting in H poisoning on B_A sites. The band structures and absorption spectra indicate that introducing B atoms can decrease the band gap and enhance the light absorption ability in the visible range. I believe that our present work would motivate experimental work to prove and explore more carbon nitride materials for N_2RR. Moreover, I also aware upcoming works should not only consider N_2 adsorption and fixation ability but also need to consider NH_3 desorption ability.

References

[1] J. N. Galloway, A. R. Townsend, J. W. Erisman, M. Bekunda, Z. Cai, J. R. Freney, L. A. Martinelli, S. P. Seitzinger, M. A. Sutton, Science, **320**, 889 (2008).

[2] V. Rosca, M. Duca, M. T. de Groot, M. T. Koper, Chem. Rev., **109**, 2209-2244 (2009).

[3] R. Schlögl, Angew. Chem. Int. Ed., **42**, 2004-2008 (2003).

[4] J. Zhao, Z. Chen, J. Am. Chem. Soc., **139**, 12480-12487 (2017).

[5] Z. W. Seh, J. Kibsgaard, C. F. Dickens, I. Chorkendorff, J. K. Nørskov, T. F. Jaramillo, Science, **355**, 6321 (2017).

[6] C. J. M. Van der Ham, M. T. M. Koper, D. G. H. Hetterscheid, Chem. Soc. Rev., **43**, 5183-191 (2014).

[7] J. Wang, L. Yu, L. Hu, G. Chen, H. Xin, X. Feng, Nat. Commun., **9**, 1-7 (2018).

[8] S. Licht, B. Cui, B. Wang, F. Li, J. Lau, S. Liu, Science, **345**, 637-640 (2014).

[9] X. Liu, L. Dai, Nat. Rev. Mater., **1**, 1-12 (2016).

[10] C. Hu, Y. Lin, J. W. Connell, H. Cheng, Y. Gogotsi, M. Titirici, L. Dai, Adv. Mater., **31**, 1806128 (2019).

[11] X. Wang, K. Maeda, A. Thomas, K. Takanabe, G. Xin, J. M. Carlsson, K. Domen, M. Antonietti, Nat. Mater., **8**, 76 (2008).

[12] P. Kumar, E. Vahidzadeh, U. K. Thakur, P. Kar, K. M. Alam, A. Goswami, N. Mahdi, K. Cui, G. M. Bernard, V. K. Michaelis, K. Shankar, J. Am. Chem. Soc., **141**, 5415-5436 (2019).

[13] Y. Wang, T. N. Pham, Y. Tian, Y. Morikawa, L. Yan, J. Colloid Interface Sci., **585**, 740-749 (2021).

[14] A. Schwarzer, T. Saplinova, E. Kroke, Coord. Chem. Rev., **257**, 2032-2062 (2013).

[15] H. Li, H. Hu, C. Bao, F. Guo, X. Zhang, X. Liu, J. Hua, J. Tan, A. Wang, H. Zhou, B. Yang, Y. Qu, X. Liu, Sci. Rep., **6**, 1-10 (2016).

[16] M. A. Légaré, G. Bélanger-Chabot, R. D. Dewhurst, E. Welz, I. Krummenacher, B. Engels, H. Braunschweig, Science, **359**, 896-900 (2018).

[17] X. Zhao, Z. Yang, A. V. Kuklin, G. V. Baryshnikov, H. Ågren, W. Liu, H. Zhang, X. Zhou, ACS Appl. Mater. Interfaces, **12**, 31419-31430 (2020).

[18] X. Zhao, Z. Yang, A. V. Kuklin**,** G. V. Baryshnikov, H. Ågren, X. Zhou, H. Zhang**,** ACS Appl. Mater. Interfaces, **12**, 42821-42831 (2020).

[19] X. Zhao, Z. Yang, A. V. Kuklin, G. V. Baryshnikov, H. Ågren, W. Wang, X. Zhou, H. Zhang, J. Mater. Chem. A, **8**, 13086-13094 (2020).

[20] X. Zhao, Z. Yang, H. Chen, Z. Wang, X. Zhou, H. Zhang, Coord. Chem. Rev.*,* **444**, 214042 (2021).

[21] X. Zhao, G. Hu, G. Chen, H. Zhang, S. Zhang, H. Wang, Adv. Mater., **33**, 2007650 (2021).

[22] C. Chen, D. Yan, Y. Wang, Y. Zhou, Y. Zou, Y. Li, S. Wang, Small, **15**, 1805029 (2019).

[23] C. Ling, X. Niu, Q. Li, A. Du, J. Wang, J. Am. Chem. Soc., **43**, 14161-14168 (2018).

[24] Y. Morikawa, Phys. Rev. B, **51**, 14802 (1995).

[25] Y. Hamamoto, I. Hamada, K. Inagaki, Y. Morikawa, Phys. Rev. B, **93**, 245440 (2016)

[26] F. Muttaqien, Y. Hamamoto, I. Hamada, K. Inagaki, Y. Shiozawa, K. Mukai, T. Koitaya, S. Yoshimoto, J. Yoshinobu, Y. Morikawa, J. Chem. Phys., **147**, 094702 (2017).

[27] F. Muttaqien, H. Oshima, Y. Hamamoto, K. Inagaki, I. Hamada, Y. Morikawa, Chem. Commun., **53**, 9222-9225 (2017).

[28] J. P. Perdew, K. Burke, M. Ernzerhof, Phys. Rev. Lett., **77**, 3865-3868 (1996).

[29] S. Grimme, J. Comput. Chem., **27**,1787-1799 (2006).

[30] D. Vanderbilt, Phys. Rev. B, **41**, 7892-7895 (1990).

[31] J. Rossmeisl, A. Logadottir, J. K. Nørskov, Chem. Phys., **319**, 178-184 (2005).

[32] A. A. Peterson, F. Abild-Pedersen, F. Studt, J. Rossmeisl, J. K. Norskov, Energy Environ. Sci., **3**, 1311-1315 (2010).

[33] J. Heyd, G. E. Scuseria, J. Chem. Phys., **121**, 1187-1192 (2004).

[34] J. Heyd, G. E. Scuseria, M. Ernzerhof, J. Chem. Phys., **118**, 8207-8215 (2003).

[35] S. J. Clark, M. D. Segall, C. J. Pickard, P. J. Hasnip, M. I. J. Probert, K. Refson, M. C. Payne, Z. Kristallogr., **220**, 567-570 (2005).

[36] M. D. Segall, P. L. D. Lindan, M. J. Probert, C. J. Pickard, P. J. Hasnip, S. J. Clark, M. C. Payne, J. Phys. Condens. Matter, **14**, 2717-2744 (2002).

[37] B. Zhu, B. Cheng, L. Zhang, J. Yu, Carbon Energy, **1**, 32-56 (2019).

[38] J. Liu, J. Phys. Chem. C, **119**, 28417-28423 (2015).

[39] Y. L. Wang, Y. Tian, Z. L. Lang, W. Guan, L. K. Yan, J. Mater. Chem. A, **6**, 21056-21063 (2018).

[40] A. Du, S. Sanvito, Z. Li, D. Wang, Y. Jiao, T. Liao, Q. Sun, Y. H. Ng, Z. Zhu, R. Amal, S. C. Smith, J. Am. Chem. Soc., **134**, 4393-4397 (2012).

[41] M. Gajdoš, K. Hummer, G. Kresse, Phys. Rev. B, **73**, 045112 (2006).

[42] Materials Studio CASTEP manual_Accelrys, 2010.

[43] B. Wei, W. Wang, J, Sun, Q. Mei, Z. An, H. Cao, D. Han, J. Xie, J. Zhan, M. He, Appl. Surf. Sci., **511**, 145549 (2020).

[44] M. W. Chase Jr, C. A. Davies, J. R. Downey Jr, D. J. Frurip, R. A. McDonaldand, A. N. Syverud, *NIST-JANAF Thermochemical Tables,* 1-1951 (1998).

[45] S. Baqi, B. Deng, Y. Guo, R. Zhang, J. Phys. Chem. C, **125**, 25207-25216 (2021).

[46] C. Cao, F. Huang, C. Cao, J. Li, H. Zhu, Diamond Relat. Mater., **15**, 1593-1600 (2006).

[47] L. Xia, H. Wang, Y. Zhao, J. Mater. Chem. A, **9**, 20615-20625 (2021).

[48] G. Henkelman, H. Jonsson, J. Chem. Phys., **113**, 9978-9985 (2000).

[49] G. Henkelman, B. P. Uberuaga, H. Jónsson, J. Chem. Phys., **113**, 9901-9904 (2000).

[50] W. Guo, K. Zhang, Z. Liang,R. Zou, Q. Xu , Chem, Soc. Rev., **48**, 5658-5716 (2019).

[51] X. F. Li, Q. K. Li, J. Cheng, L. Liu, Q. Yan, Y. Wu, X. H. Zhang, Z. Y. Wang, Q. Qiu and Y. Luo, J. Am. Chem. Soc., **138**, 8706-8709 (2016).

[52] C. Wang, Y. Zhao, C. Y. Zhu, M. Zhang, Y. Geng, Y. G. Li, Z. M. Su, J. Mater. Chem. A, **8**, 23599-23606 (2020).

[53] E. S. lason, T. Bligaard, S. G. Gudmundsdóttir, F. Studt, J. Rossmeisl, F. A. Pedersen, T. Vegge, H. J. nsso, J. K. Nørskov, Phys. Chem. Chem. Phys., **14**, 1235-1245 (2012).

[54] Y. L. Wang, C. X. Wu, Y. Tian, L. K. Yan, H. Q. Tan, Z. M. Su, Appl. Surf. Sci., **453**, 442-448 (2018).

[55] R. Huang, X. Li, W. Gao, X. Zhang, S. Liang, M. Luo, RSC Adv., **11**, 14844-14861 (2021).

[56] A. Patra, H. Peng, J. Sun, Jo. P. Perdew, Phys. Rev. B, **100**, 035442 (2019).

[57] J. Lee, L. Tan, S. Chai, Nanoscale, **13**, 7011-7033 (2021).

[58] K. K. Dalal, A. C. Emily, J. Phys. Chem. C., **116**, 9876-9887 (2012).

[59] J. P. Perdew, R. G. Parr, M. Levy, J. L. Balduz, Jr., Phys. Rev. Lett., **49**, 1691 (1982).

[60] J. O. M. Bockris, S. U. M. Khan, Springer: New York, 1993.

[61] M. Qiao, J. Liu, Y. Wang, Y. Li, Z. Chen, J. Am. Chem. Soc., **140**, 12256-12262 (2018).

[62] X. Lv, W. Wei, F. Li, B. Huang, Y. Dai, Nano Lett., **19**, 6391-6399 (2019).

[63] I. Hamada, Y. Morikawa, J. Phys. Chem. C, **112**, 10889-10898 (2008).

[64] I. Hamada, Y. Morikawa, J. Chem. Phys., **134**, 154701 (2011).

[65] T. N. Pham, Y. Hamamoto, K. Inagaki, D.N. Son, I. Hamada, Y. Morikawa, J. Phys. Chem. C, **124**, 2968-2977 (2020).

[66] C. Liu, Q. Li, C. Wu, J. Zhang, Y. Jin, D. R. MacFarlane, C. Sun, J. Am. Chem. Soc., **141**, 2884-2888 (2019).

[67] Z. Q. Chu, C. Stampfl, X. M. Duan, J. Phys. Chem. C, 2019, **123**, 28739-28743.

[68] S. Ji, Z. Wang, J. Zhao, J. Mater. Chem. A, **7**, 2392-2399 (2019).

[69] J. Zhang, Y. Zhao, Z. Wang, G. Yang, J. Tian, D. Ma, Y. Wang, New J. Chem., **44**, 422-427 (2020).

[70] X. Zhang, T. Wu, H. Wang, R. Zhao, H. Chen, T. Wang, P. Wei, Y. Luo, Y. Zhang, X. Sun, ACS Catal., **9**, 4609-4615 (2019).

[71] W. Qiu, X. Y. Xie, J. Qiu, W. Fang, R. Liang, X. Ren, X. Ji, G. Cui, A. M. Asiri, G. Cui, B. Tang, X. Sun, Nat. Commun., **9**, 1-8 (2018).

[72] C. Liang, H. Niu, H. Guo, C. Niu, D. Huang, Y. Yang, H. Liu, B. Shao, H. Feng, Chem. Eng. J., **396**, 125395 (2020).

Chapter 5

DFT Investigation on Oxygen Reduction Reaction over Nitrogen (N) doped Graphdiyne as an Electrocatalyst: The Importance of Pre-adsorbed OH* and Solvation Effect

5.1 Introduction

Fuel cells are an innovative and efficient energy conversion technology that operates with electrochemical reactions. The uses of clean and renewable fuels such as hydrogen, methanol, and biomass reduce dependence on fossil fuels and associated environmental impacts [1-3]. The oxygen reduction reaction (ORR) is a key electrochemical reaction that takes place at the cathode of fuel cells [4]. Traditionally, platinum (Pt) and Pt-based materials have been widely used as electrocatalysts for ORR due to their excellent electrocatalytic activity, durability, and stability [5], however, the high cost and scarcity of Pt have led to significant research efforts to find alternative electrocatalysts that can perform as effectively as Pt-based materials while being more cost-effective and environmentally sustainable [4,6]. In 2009, Dai *et al.* reported that N-doped carbon nanotube arrays possessed high electrocatalytic activity for the ORR in alkaline media, even superior to Pt [7]. This finding led to an interesting field of metal-free carbon-based ORR electrocatalysts because of their advantages, including relatively abundant raw materials, economic feasibility, adjustable surface chemistry, easy processing, large specific surface area, high chemical stability, fast transfer kinetics, and a wide operating

temperature range [6]. Based on many findings [8-11], N doping is a particularly advantageous method to modify carbon materials for the energy conversion such as hydrogen evolution reaction (HER), oxygen evolution reaction (OER), ORR, nitrogen reduction reaction (N_2RR), and carbon dioxide reduction reaction (CO_2RR).

Recently, a new-type carbon material named graphdiyne (GDY), a rising star of 2D carbon allotropes with one-atom thick planar layers, has achieved the coexistence of sp and sp^2 hybridized carbon atoms in a 2D planar structure [12-14]. GDY with unique chemical and physical properties has attracted more attention in energy conversion [15-17]. However, pure GDY has low ORR electrocatalytic activity, and structural modification including doping metal or nonmetal atoms is a good way to improve the activity. Gao *et al.* [18] reported Fe-doped GDY (Fe@GDY) had achieved a high catalytic activity towards ORR like or even better than the benchmark commercial Pt/C (20 wt%). Dai *et al.* [19] predicted that Ni@GDY and Pt@GDY catalysts possessed comparable electrocatalytic activity for ORR and OER in alkaline media by DFT. Li *et al.* [20] reported that N-doped GDY, especially sp-N doping shows much better ORR electrocatalytic performance than that of the commercial Pt-based catalyst in alkaline media and comparable activity in acidic media. On the other hand, Huang *et al.* [21] reported that pyridinic (Pyri)-NGDY is mainly produced by N doping and Pyri-NDGY exhibits excellent ORR and OER catalytic activity. Despite experimental evidence demonstrating the excellent ORR electrocatalytic activity of N-doped GDY, the nature of the active sites and the dopants involved are still controversial. Recently, a few theoretical works of ORR on N-doped GDY with sp-N configurations were reported [22-24]. Li *et al.* [22] found that ORR proceeds on sp-N(II)GDY with the associative mechanism. The highest ORR electrocatalytic activity has a theoretical onset potential of 0.76 V with metastable adsorption of all ORR intermediates. Lee *et al.* [23] found that double N-doped GDY has better ORR activity. In the above works, it turns out that the metastable adsorption sites of ORR

intermediates govern the ORR performance. However, the role of the most stable adsorption sites in the ORR mechanism on N-doped GDY remains ambiguous.

Density functional theory (DFT) calculation is a powerful tool to explore the ORR mechanism using the computational hydrogen electrode (CHE) model [25], however, to elucidate the ORR activity accurately, it is important to incorporate solvation effect. There are two approaches: (1) the explicit model and (2) the implicit model. The former approach involves adding water molecules around the reactant or above the surface to represent solvation effect [26-29], and the latter approach replaces the liquid environment with a polarizable continuous medium (PCM) [30-31]. Previous theoretical studies on metal-free catalysts mostly applied the implicit model, which tends to underestimate solvation effect during the ORR process. Boresch *et al.* [32] reported that PCM cannot describe any direct solvent effects and might be inaccurate for specific hydrogen bonds. Wang *et al.* [33] reported that the explicit model can give a correct estimation for the ORR overpotential on MnN_4-graphene catalyst than the gas-phase model. Hansen *et al.* [34] investigated the solvation energy of ORR intermediates on N-doped graphene using explicit and implicit models, and they found including explicit H_2O molecules is essential for a correct description of ORR intermediates adsorption energy on carbon materials, while continuum solvation models are unable to describe solvation energy correctly.

In this work, I systemically investigated the ORR activity on sp-N1 and Pyri-N doped GDY with graphene (G) support. DFT calculations and *ab initio* molecular dynamics (AIMD) simulations were carried out to investigate the ORR mechanism as well as solvation effect for ORR in both cases. Free energy diagrams showed that the active sites of sp-N1 doped GDY surfaces are easily terminated by OH* and neighboring C sites of –COH–N moiety become real active sites for ORR to proceed with low overpotentials compared with Pyri-N. Moreover,

the explicit solvation model can give a more consistent overpotential (0.46 V) with experimental value (0.36 V) compared with that in vacuum conditions (0.72 V).

5.2 Computational Details

Most of DFT calculations were performed with the Simulation Tool for the Atom Technology (STATE) program package [35-38]. Ionic cores were described by using the ultrasoft pseudopotentials [39], and valence electron states were expanded by a plane wave basis set with the kinetic energy cutoffs of 36 and 400 Ry for wave functions and augmented charge density, respectively. A 2 × 4 × 1 Monkhorst-Pack k-point sampling was used for the N-doped GDY 2 × 1 × 1 supercell. The revised PBE (RPBE) functional [40] with the Grimme's van der Waals (vdW) correction (D2) [41] was employed to describe the weak dispersion interactions between various intermediates and surfaces as well as to describe water-water interaction more accurately [29].

Spin-polarized calculations were performed whenever triplet O_2 is simulated. I considered the intersystem crossing (ISC) upon O_2 adsorption on the substrate. The isolated O_2 in the triplet state ($^3\sum_g^-$) as its ground electronic state, which is relatively unreactive due to its low energy. However, when O_2 approaches surfaces such as carbon nanotubes and diamond (100) surface [42-43], it can undergo the intersystem crossing (ISC) to a more reactive singlet state ($^1\Delta_g$). In my calculations, the adsorbed O_2 in $^3\sum_g^-$ was modeled by fixing the difference between the number of spin-up and spin-down electrons to two, while the adsorbed O_2 in $^1\Delta_g$ was modeled by a spin-restricted calculation to obtain a closed-shell configuration, which was necessary to prevent spin contamination. Activation reaction barriers (E_a) were calculated using the climbing image nudge elastic band method (CI-NEB) [44-45].

According to the experimental condition [20], the overall reaction of O_2 reduction to H_2O on N-doped GDY in the alkaline condition is $O_2(g) + 2H_2O(l) + 4e^- \rightarrow 4OH^-$. The ORR

mechanism is divided into dissociative mechanism and associative mechanism. For the dissociative mechanism, ORR proceeds with the following elementary steps [46-47]:

$$O_2(g) + * \rightarrow 2O* \quad (5\text{-}1)$$

$$2O* + H_2O(l) + e^- \rightarrow O* + OH* + OH^- \quad (5\text{-}2)$$

$$O* + OH* + e^- \rightarrow O* + OH^- \quad (5\text{-}3)$$

$$O* + H_2O(l) + e^- \rightarrow OH* + OH^- \quad (5\text{-}4)$$

$$OH* + e^- \rightarrow OH^- + * \quad (5\text{-}5)$$

The ET-OHP associative mechanism proceeds as follows [46-47]:

$$O_2(g) + H_2O(l) + e^- + * \rightarrow OOH* + OH^- \quad (5\text{-}6)$$

$$OOH* + e^- \rightarrow O* + OH^- \quad (5\text{-}7)$$

$$O* + H_2O(l) + e^- \rightarrow OH* + OH^- \quad (5\text{-}4)$$

$$OH* + e^- \rightarrow OH^- + * \quad (5\text{-}5)$$

The reaction Gibbs free energies (ΔG) of the reactions (5-1)-(5-7) can be expressed as:

$$\Delta G_1 = \mu_{2O*} - \mu_{O_2} - \mu_* \quad (5\text{-}8)$$

$$\Delta G_2 = \mu_{O*+OH*} + \mu_{OH^-} - (\mu_{2O*} + \mu_{H_2O(l)} + \mu_{e^-}) \quad (5\text{-}9)$$

$$\Delta G_3 = \mu_{O*} + \mu_{OH^-} - (\mu_{O*+OH*} + \mu_{e^-}) \quad (5\text{-}10)$$

$$\Delta G_4 = \mu_{OH*} + \mu_{OH^-} - (\mu_{O*} + \mu_{H_2O(l)} + \mu_{e^-}) \quad (5\text{-}11)$$

$$\Delta G_5 = \mu_* + \mu_{OH^-} - (\mu_{OH*} + \mu_{e^-}) \quad (5\text{-}12)$$

$$\Delta G_6 = \mu_{OOH*} + \mu_{OH^-} - (\mu_{O_2} + \mu_* + \mu_{H_2O(l)} + \mu_{e^-}) \quad (5\text{-}13)$$

$$\Delta G_7 = \mu_{O*} + \mu_{OH^-} - (\mu_{OOH*} + \mu_{e^-}) \quad (5\text{-}14)$$

where μ denotes the (electro)chemical potential of the indicated species. These chemical potentials of the reaction intermediates can be obtained from [48]:

$$\mu_* = E_* \quad (5\text{-}15)$$

$$\mu_{X*} = E_{X*} + H_{X*} - TS_{X*} \quad (5\text{-}16)$$

$$\mu_{H_2O(l)} = E_{H_2O(l)} + H_{H_2O(l)} - TS_{H_2O(l)}$$
$$= E_{H_2O(g)} + H_{H_2O(g)} - TS_{H_2O(g)} + RT \times \ln\left(\frac{P}{P_0}\right) \quad (5\text{-}17)$$

$$H = E_{elec} + E_{ZPE} + \int_0^T C_P dT \quad (5\text{-}18)$$

where E_* and E_{X*} are the (DFT) total energies of the clean surface (∗) and of surfaces with a single adsorbed species X, respectively. H_{X*} and S_{X*} are the corresponding enthalpies and entropies, respectively. T is the temperature (298.15 K). $E_{H_2O(g)}$, $H_{H_2O(g)}$, and $S_{H_2O(g)}$ are the DFT total energy, enthalpy, and entropy of gas H_2O, respectively. Enthalpies and entropies for gas phase molecules have been determined in the ideal gas limit [49], for adsorbates, the harmonic limit was used [50]. The chemical potential for H_2O (g) is calculated at 0.035 bar [6] because this is the equilibrium pressure of H_2O (l) at 298.15 K. R is gas constant, P_0 with = 1 bar, and P = 0.035 bar. For O_2, the chemical potential is obtained from the experimental formation energy of O_2 with respect to water, because DFT tends to underestimate the O_2 atomization energy. According to the thermodynamic energy (4.92 eV) released by the reaction of $2H_2(g) + O_2(g) \rightarrow 2H_2O(l)$ can be written as [51]:

$$\mu_{O_2(g)} = 2\mu_{H_2O(l)} + 4.92 - 2\mu_{H_2(g)} \quad (5\text{-}19)$$

For μ_{OH^-} and μ_{e^-}, I only need the difference $\mu_{OH^-} - \mu_{e^-}$. To calculate this difference, I assume the equilibrium H_2O (l) ↔ $H^+ + OH^-$, which relates the chemical potentials as:

$$\mu_{OH^-} + \mu_{H^+} = \mu_{H_2O(l)} \quad (5\text{-}20)$$

rewritten as：

$$\mu_{OH^-} - \mu_{e^-} + \mu_{H^+} + \mu_{e^-} = \mu_{H_2O(l)} \quad (5\text{-}21)$$

$$\mu_{OH^-} - \mu_{e^-} = \mu_{H_2O(l)} - (\mu_{H^+} + \mu_{e^-}) \quad (5\text{-}22)$$

where, $(\mu_{H^+} + \mu_{e^-})$ can be calculated using the CHE approach ($H^+ + e^- \leftrightarrow$ ½H_2(g)), so the chemical potential of $\mu_{H^+} + \mu_{e^-}$ can be calculated using:

$$\mu_{H^+} + \mu_{e^-} = 1/2\mu_{H_2} \quad (5\text{-}23)$$

I describe this equilibrium using the reversible hydrogen electrode (RHE) [52] as the reference electrode, which it equals the chemical potential of $H^+ + e^-$ to the chemical potential of $1/2H_2$ at arbitrary pH (pH_2 = 1 bar and T = 298.15 K), so μ_{H^+} and μ_{e^-} can be expressed as:

$$\mu_{H^+} = \mu_{H^+}^{RHE} \quad (5\text{-}24)$$

$$\mu_{e^-} = \mu_{e^-}^{RHE} - eU_{RHE} \quad (5\text{-}25)$$

where U_{RHE} is the potential of the electrode relative to the RHE.

Combining equations (5-23)-(5-25), the equilibrium can be expressed as:

$$\mu_{H^+} + \mu_{e^-} = \mu_{H^+}^{RHE} + \mu_{e^-}^{RHE} - eU_{RHE} = 1/2\mu_{H_2} - eU_{RHE} \quad (5\text{-}26)$$

Substituting the equation (5-26) into equation (5-22) to obtain the following equation:

$$\mu_{OH^-} - \mu_{e^-} = \mu_{H_2O(l)} - (1/2\mu_{H_2} - eU_{RHE}) \quad (5\text{-}27)$$

Using equation (5-27) to replace the term ($\mu_{OH^-} - \mu_{e^-}$) in equations, I finally get the reaction Gibbs free energies:

$$\Delta G_1 = \mu_{2O*} - 2\mu_{H_2O(l)} - 4.92 + 2\mu_{H_2} - E_* \quad (5\text{-}28)$$

$$\Delta G_2 = \mu_{O*+OH*} - \mu_{2O*} - 1/2\mu_{H_2} + eU_{RHE} \quad (5\text{-}29)$$

$$\Delta G_3 = \mu_{O*} - \mu_{O*+OH*} + \mu_{H_2O(l)} - 1/2\mu_{H_2} + eU_{RHE} \quad (5\text{-}30)$$

$$\Delta G_4 = \mu_{OH*} - \mu_{O*} - 1/2\mu_{H_2} + eU_{RHE} \quad (5\text{-}31)$$

$$\Delta G_5 = \mu_{*} - \mu_{OH*} + \mu_{H_2O(l)} - 1/2\mu_{H_2} + eU_{RHE} \quad (5\text{-}32)$$

$$\Delta G_6 = \mu_{OOH*} - E_* - 2\mu_{H_2O(l)} - 4.92 + 3/2\mu_{H_2} + eU_{RHE} \quad (5\text{-}33)$$

$$\Delta G_7 = \mu_{O*} - \mu_{OOH*} + \mu_{H_2O(l)} - 1/2\mu_{H_2} + eU_{RHE} \quad (5\text{-}34)$$

The overpotential is given by:

$$\eta = \frac{1}{e}\Delta G_{max} + 1.23 \quad (5\text{-}35)$$

In this work, I also consider solvation energy ΔSol(X*) defined by the energy difference between the ΔE of 2O*, O*+OH*, OOH, O*, and *OH on the surface with and without water and the equation as follow:

$$\Delta\mathrm{Sol(X^*)} = \Delta E_{\mathrm{X^*+mH_2O^*}} - \Delta E_{\mathrm{X^*}} \tag{5-36}$$

where $\Delta E_{\mathrm{X^*+m}H_2O}$ and $\Delta E_{\mathrm{X^*}}$ are the adsorption energies change of each intermediate on surface with and without water, defined as follows [53]:

$$\Delta E_{\mathrm{2O^*+mH_2O^*}} = E_{\mathrm{2O^*+mH_2O^*}} - E_* - \mathrm{m}\Delta E_{\mathrm{nH_2O^*}} - \mathrm{m}E_{\mathrm{H_2O(g)}} - [2E_{\mathrm{H_2O(g)}} - 2E_{\mathrm{H_2}}] \tag{5-37}$$

$$\Delta E_{\mathrm{O^*+OH^*+mH_2O^*}} = E_{\mathrm{O^*+OH^*+mH_2O^*}} - E_* - \mathrm{m}\Delta E_{\mathrm{nH_2O^*}} - \mathrm{m}E_{\mathrm{H_2O(g)}} - [2E_{\mathrm{H_2O(g)}} - 3/2E_{\mathrm{H_2}}] \tag{5-38}$$

$$\Delta E_{\mathrm{OOH^*+mH_2O^*}} = E_{\mathrm{OOH^*+mH_2O^*}} - E_* - \mathrm{m}\Delta E_{\mathrm{nH_2O^*}} - \mathrm{m}E_{\mathrm{H_2O(g)}} - [2E_{\mathrm{H_2O(g)}} - 3/2E_{\mathrm{H_2}}] \tag{5-39}$$

$$\Delta E_{\mathrm{O^*+mH_2O^*}} = E_{\mathrm{O^*+mH_2O^*}} - E_* - \mathrm{m}\Delta E_{\mathrm{nH_2O^*}} - \mathrm{m}E_{\mathrm{H_2O(g)}} - [E_{\mathrm{H_2O(g)}} - E_{\mathrm{H_2}}] \tag{5-40}$$

$$\Delta E_{\mathrm{OH^*+mH_2O^*}} = E_{\mathrm{OH^*+mH_2O^*}} - E_* - \mathrm{m}\Delta E_{\mathrm{nH_2O^*}} - \mathrm{m}E_{\mathrm{H_2O(g)}} - [E_{\mathrm{H_2O(g)}} - 1/2E_{\mathrm{H_2}}] \tag{5-41}$$

$$\Delta E_{\mathrm{2O^*}} = E_{\mathrm{2O^*}} - E_* - [2E_{\mathrm{H_2O(g)}} - 2E_{\mathrm{H_2}}] \tag{5-42}$$

$$\Delta E_{\mathrm{O^*+OH^*}} = E_{\mathrm{O^*+OH^*}} - E_* - [2E_{\mathrm{H_2O(g)}} - 3/2E_{\mathrm{H_2}}] \tag{5-43}$$

$$\Delta E_{\mathrm{OOH^*}} = E_{\mathrm{OOH^*}} - E_* - [2E_{\mathrm{H_2O(g)}} - 3/2E_{\mathrm{H_2}}] \tag{5-44}$$

$$\Delta E_{\mathrm{O^*}} = E_{\mathrm{O^*}} - E_* - [E_{\mathrm{H_2O(g)}} - E_{H_2}] \tag{5-45}$$

$$\Delta E_{\mathrm{OH^*}} = E_{\mathrm{OH^*}} - E_* - [E_{\mathrm{H_2O(g)}} - 1/2E_{H_2}] \tag{5-46}$$

where $E_{\mathrm{2O^*+mH_2O^*}}$, $E_{\mathrm{O^*+OH^*+mH_2O^*}}$, $E_{\mathrm{OOH^*+mH_2O^*}}$, $E_{\mathrm{O^*+mH_2O^*}}$, $E_{\mathrm{OH^*+mH_2O^*}}$, $E_{\mathrm{2O^*}}$, $E_{\mathrm{O^*+OH^*}}$, $E_{\mathrm{OOH^*}}$, $E_{\mathrm{O^*}}$, and $E_{\mathrm{OH^*}}$ are total energy of 2O*, O*+OH*, OOH, O*, and *OH on surface with and without water, respectively. n is the number of water molecules in water layer, m = n−1, $\Delta E_{\mathrm{nH_2O^*}}$ is [53]:

$$\Delta E_{\mathrm{nH_2O^*}} = (E_{\mathrm{nH_2O^*}} - E_* - \mathrm{n}E_{\mathrm{H_2O(g)}})/\mathrm{n} \tag{5-47}$$

Finally, the adsorption free energy of each ORR intermediates including solvation effect was defined as:

$$\Delta G_{\text{ads}}(\text{X*}) = \Delta E_{\text{X*}} + (\Delta H_{\text{X*}} - T\Delta \text{S}_{\text{X*}}) - \text{ne}U_{\text{RHE}} + \Delta\text{Sol}(\text{X*}) \qquad (5\text{-}48)$$

where$\Delta E_{\text{X*}}$, $\Delta H_{\text{X*}}$, and $\Delta \text{S}_{\text{X*}}$ are the adsorption energies change, enthalpies, and entropies of each intermediate on surface in vacuum condition, respectively. T is the temperature (298.15 K). ne is the number of electrons transferred, ne is the number of electrons transferred, the number of electrons transferred in 2O*, O*+OH*, OOH*, O* and OH* are $4e^-$, $3e^-$, $3e^-$, $2e^-$, and $1e^-$, respectively.

To elucidate the effect of solvents on the ORR mechanism, I calculated the *ab inito* molecular dynamics (AIMD) [54] employing the "effective screening medium" method [55] by using STATE. Representative of the configurational simulation cells is shown in Scheme 5.1. A semi-infinite continuum with an infinite dielectric constant, i.e., a classical conductor, was located beyond $Z = Z_1$, while another region was characterized by the dielectric constant of unity, i.e., the vacuum medium. The neutral charge is introduced in this work. An artificial boundary ($Z_2 = 9.3$ Å) was placed above the surface and water molecules, restricting their movement, and maintaining the density at ~1 g·cm^{-3}. In Scheme 5.1, $Z_3<Z<Z_2$ region is the contact region of water with vacuum, $Z_4<Z<Z_3$ is the "bulk" water region where it corresponds to regions ~1 g·cm^{-3} of the experimental bulk water density, and $Z_5<Z<Z_4$ is water contact region with the surface. The AIMD simulations were sampled by the canonical (NVT) ensemble employing Nose-Hoover thermostats with a time step of 1.0 fs at a finite temperature of 400 K. I chose 400K which is higher than the experiment condition (~300K), this is due to overestimation of the melting point of ice predicted by DFT [56]. Moreover, higher temperature also helps us explore more local minimum structures of water/NGDY interfaces. Upon these systems, I performed 18 ps long AIMD simulations with the last 15 ps used for analysis. Then, we chose the five snapshots with the most hydrogen bond (H bond) networks in the contact region with the surface ($Z_5<Z<Z_4$) at the last 15 ps. Finally, I replace one water

that is near the active site to the ORR intermediate and use equation (5-35)-(5-45) to get the average solvation energy (ΔSol) of each ORR intermediate.

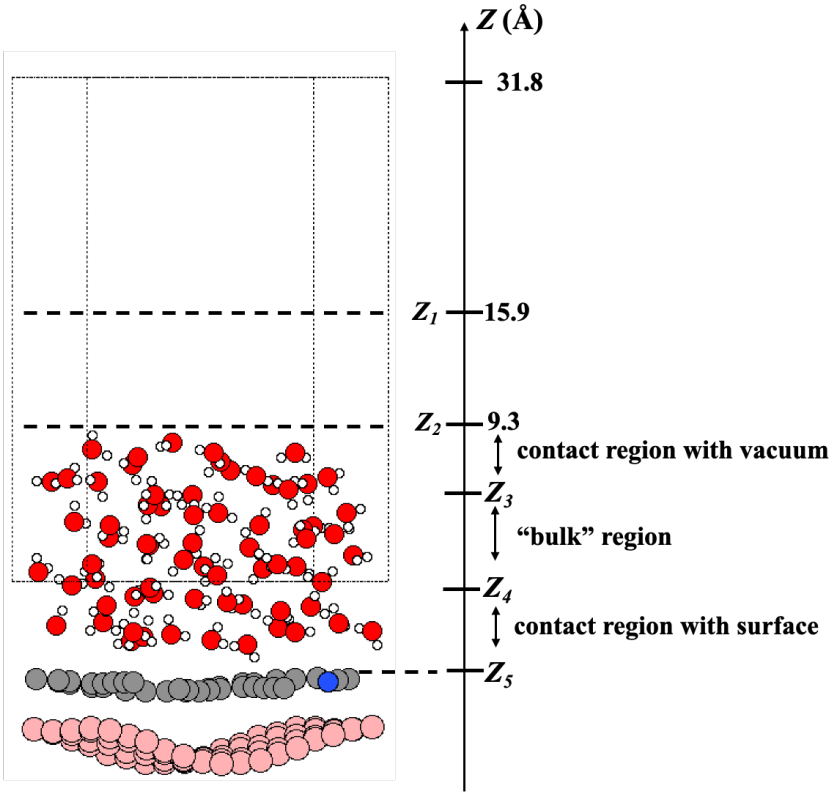

Scheme 5.1: Computational set-up of the simulation (e.g., one snapshot of sp-N1GDY/G). Red, white, gray, pink and blue balls are O atoms, H atoms, C atoms in N-doped GDY, C atoms in G, and N atoms, respectively.

5.3 Results and Discussions

5.3.1 Atomic and Electronic Structures of N-doped GDY Catalysts

Based on the experimental results [20-21], I constructed the two types of N-doped GDY (NGDY), namely sp-NGDY and Pyri-NGDY. As shown in Figure 5.1, the carbon atom in diacetylene linkage (sp hybridized C) is replaced by N to generate two types of sp-N (Figure 5.1(b)-(c)), i.e., sp-N1GDY, sp-N2GDY. Pyri-NGDY is the sp^2 hybridized N atom bonded with two sp^2 hybridized carbon (C) neighbors in the carbon ring and with H-terminated C atoms

(Figure 5.1 (d)). In experiment [20], N-doped GDY has been supported onto glassy carbon, herein to simply the model, graphene (G) is applied as a support underneath the N-doped GDY. The optimized lattice constants of the N-doped GDY (9.46 Å), and graphene (2.46 Å) unit cells were obtained consistently with the previous results [57-58]. Considering the lattice matching between the two components, the $p(8 \times 4)$ supercell of G and the $p(2 \times 1)$ supercell of N-doped GDY are employed to create the interface model (Figure 5.1 (e)-(g)) with applying mixed tensile/compressive strain (4%) to the graphene phase, resulting in the corrugated graphene. The calculated minimum distances between sp-NGDY or Pyri-NGDY, and the top of graphene are 2.27 and 2.17 Å, which are close to those of other heterostructures [59]. The band gap (E_g) of the isolated G, NGDY in three N configurations (sp-N1, sp-N2, Pyri-N) and their interface models (sp-N1GDY/G, sp-N2GDY/G, and pyri-NGDY/G) were calculated by the PBE [60] and HSE06 functional [61-62] using VASP code [63-64] as shown in Table C.1. I find that Pyri-NGDY is a semiconductor with a band gap of 0.60 eV by PBE and 0.97 eV by HSE06, while sp-N1GDY and sp-N2GDY are metallic as predicted by both functionals. After introducing the G substrate as the support, all sp-N1GDY, sp-N2GDY, and Pyri-NGDY have metallicity.

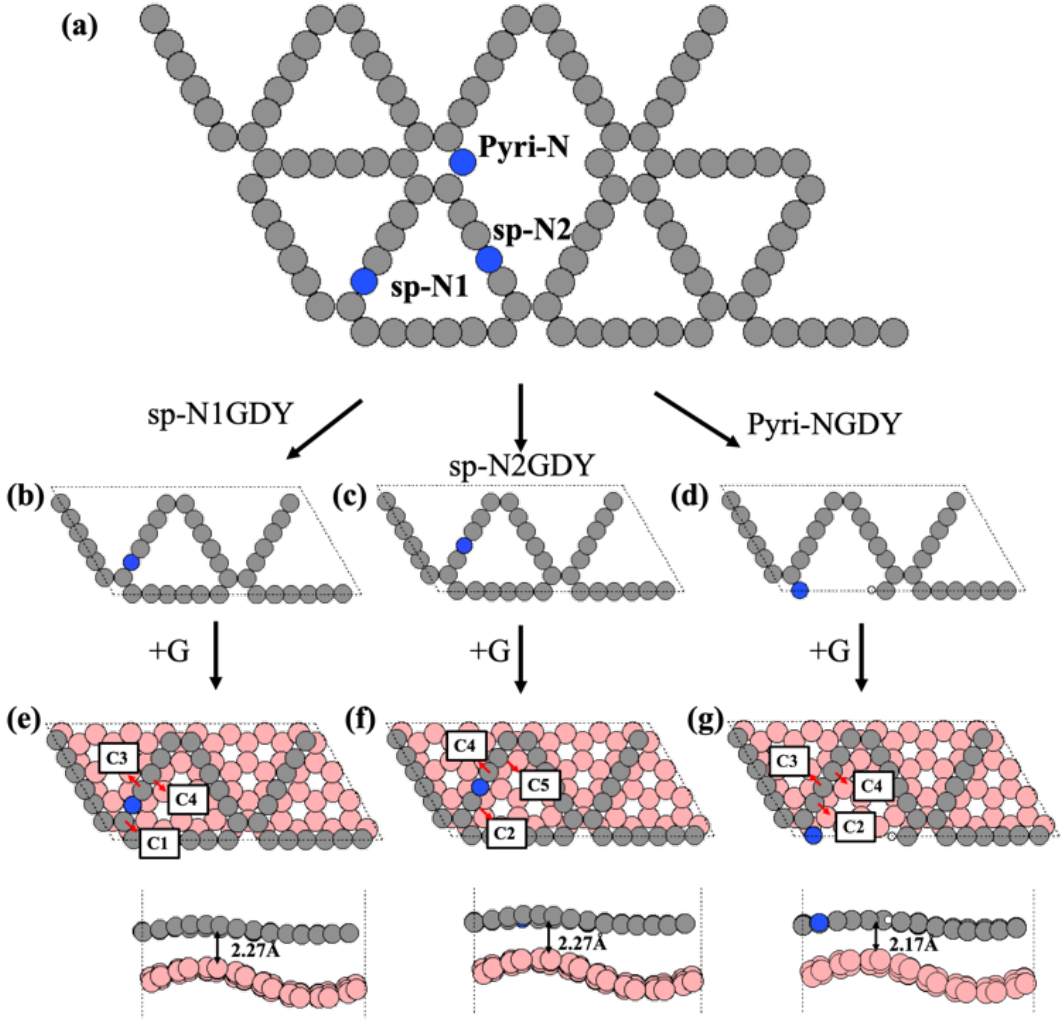

Figure 5.1: (a) Schematic representation of different types of N doping configurations (sp-N1, sp-N2, and Pyri-N) in GDY. Optimized structure of sp-N1GDY (b), sp-N2GDY(c), Pyri-NGDY (d), sp-N1GDY/G (e), sp-N2GDY/G (f) and pyri-NGDY/G (g). Red, white, gray, pink and blue are O atoms, H atoms, C atoms in N-doped GDY, C atoms in G, and N atoms, respectively.

To explore the charge transfer of three N-doped GDY/G interfaces, I calculated the projected density of states (PDOS) (Figure 5.2), charge density difference (CDD), and Bader charge of three cases (Figure C.1). The PDOS results showed that after the introduction of G, the Dirac point of G in sp-N1GDY/G, sp-N2GDY/G, and Pyri-NGDY/G is upshifted above the Fermi level, on the other hand, the C 2p of sp-N1GDY, sp-N2GDY, and Pyri-NGDY in sp-N1GDY/G, sp-N2GDY/G and Pyri-NGDY/G are downshifted below the Fermi level. The C

p-band centers in three N-doped GDY are shifted to a lower energy region upon the introduction of G (Figure 5.2). The above results indicated that the use of G can increase the conductivity of N-doped GDY and induce the charge transfer from G to N-doped GDY. The CDD (Figure C.1) results also reveal that the charge densities are redistributed by forming electron-rich and hole-rich regions within the three N-doped GDY/G interfaces. The charge depletion occurs on the G surfaces, resulting in hole-rich sites. However, strong charge accumulation occurs on the three N-doped GDY surfaces, forming electron-rich sites. Therefore, the electrons are mainly transferred from G to the three N-doped GDY surfaces. To confirm this, the Bader charge analysis (Figure C.1) and work function change (Table C.2) are also conducted. From the Bader charge analysis, 0.11 e^- are transferred from the G substrate to sp-N1GDY or sp-N2GDY, and 0.13 e^- are transferred from the G substrate to Pyri-NGDY. As shown in Table C.2, the work functions of planar G (4.20 eV) and corrugated G (4.10 eV) are smaller than the work functions of pure GDY (5.10 eV), sp-NGDY (4.53 eV) and Pyri-NGDY (4.93 eV), which is the fundamental cause for charge transfer from G to GDY and NGDY.

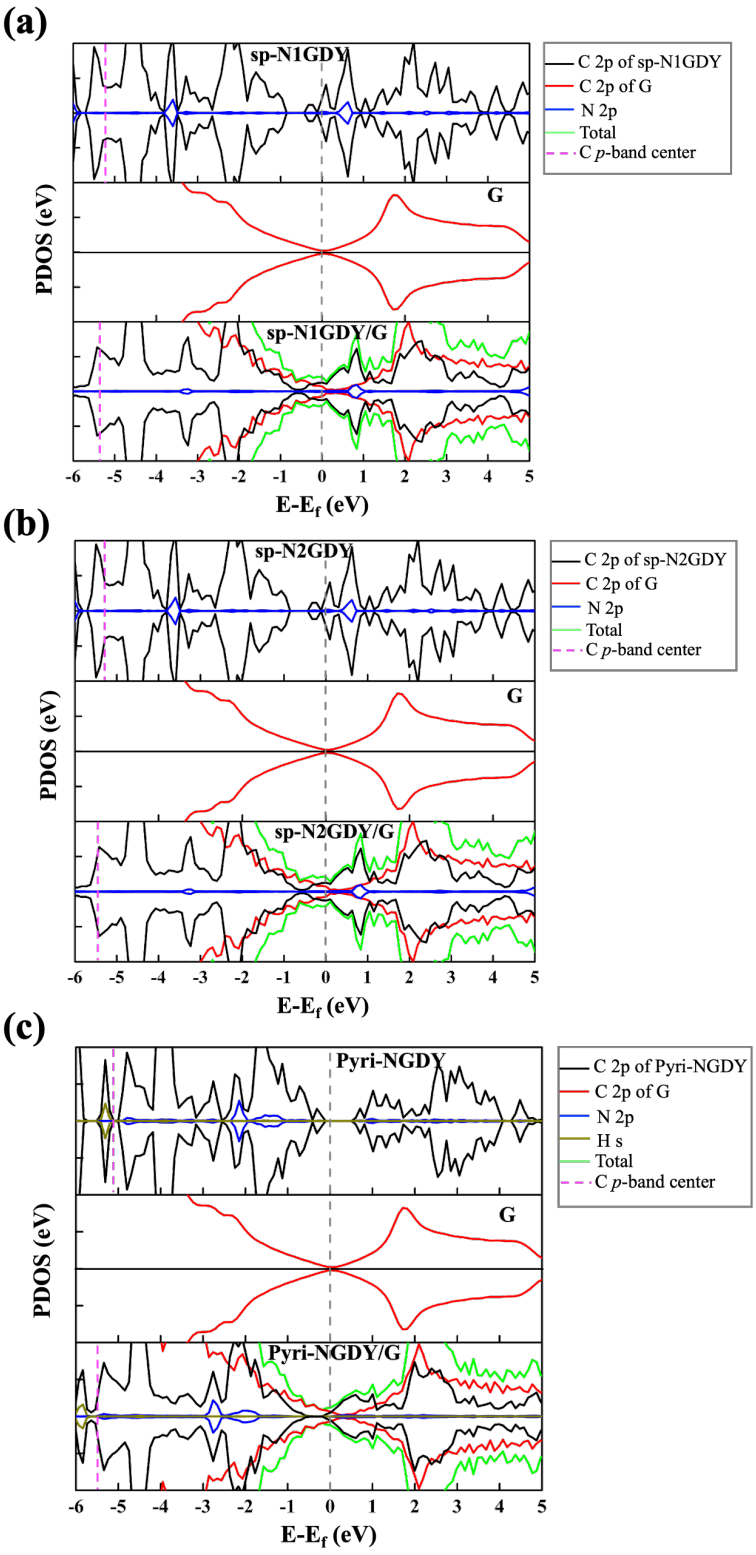

Figure 5.2: (a) The projected density of states (PDOS) on atomic orbitals of sp-N1GDY, G, and sp-N1GDY/G; (b) PDOS of sp-N2GDY, G and sp-N2GDY/G; (c) Pyri-NGDY, G and Pyri-NGDY/G. The C p energy window of integration is [-10.00 0.00].

5.3.2 The ORR Mechanism and Free Energy Analysis on sp-N1GDY/G, sp-N2GDY/G, and Pyri-NGDY/G in Vacuum Conditions

ORR mechanisms on clean surface. O_2 adsorption and dissociation are two important steps that govern the ORR pathway. Thus, I first evaluate O_2 adsorption and dissociation on N doped GDY models. I investigate all possible adsorption sites (C1-C5) of single O_2 on sp-N1GDY/G, sp-N2GDY/G, Pyri-NGDY/G in two different geometries, namely end-on and side-on (Figure C.2). I find that O_2 preferably adsorbs on top sites of the C atoms near the N dopants with different strengths between sp-N and Pyri-N configurations. O_2 is chemisorbed at the C3C4 site (Table 5.1 and Figure C.2 (b)) and the C2C4 site (Table C.3 and Figure C.2 (c)) on sp-N1GDY/G and sp-N2GDY/G, respectively. In contrast, O_2 is physisorbed on Pyri-NGDY/G (Table 5.1 and Figure C.2 (e)).

Table 5.1: The adsorption energy of O_2 and OOH, and the activation energy (E_a) of O_2 dissociation and O_2 protonation to OOH on sp-N1GDY/G, sp-N1GDY(OH)/G and Pyri-NGDY/G.

Structure	$\Delta E_{ads}(O_2)$ eV	$\Delta E_{ads}(OOH)$ eV	E_a eV			
			O_2 dissociation			O_2 protonation
			$O_2 \rightarrow O_2^* \rightarrow 2O^*$	$O_2 \rightarrow 2O^*$	$O_2 \rightarrow 2O^*$ with one H_2O	$O_2 + H_2O \rightarrow OOH^* + OH^*$
sp-N1GDY/G	−0.60	—	0.25	0.22	0.09	0.88
sp-N1GDY(OH)/G	−0.15	−1.23	—	1.86	1.64	1.40
Pyri-NGDY/G	−0.10	−0.93	—	1.52	1.35	1.17

Next, I examine the reaction barriers for an O_2 dissociation to 2O* and O_2 protonation to OOH* using the CI-NEB method with the consideration of the ISC. I consider two probable pathways on O_2 dissociation cases, namely (1) gas-phase O_2 adsorption on the surface followed by O_2* dissociation to 2O* ($O_2 \rightarrow O_2^* \rightarrow 2O^*$); (2) direct dissociative adsorption of gas-phase

O_2 to 2O* ($O_2 \rightarrow 2O^*$). Both the triplet and singlet potential energy surfaces (PES) are shown in Figure C.3. For all reaction processes, O_2 starts with a triplet state, reaches to ISC state, and changes to a singlet state. The activation reaction energies (E_a) of O_2 dissociation and protonation on the three N-doped GDY/G are shown in Table 5.1 and Figure C.3. I find that on two sp-NGDY/G systems (sp-N1GDY/G and sp-N2GDY/G), the direct $O_2 \rightarrow 2O^*$ path is kinetically the most preferable with relatively low E_a (~0.22 eV on sp-N1GDY/G and ~0.08 eV on sp-N2GDY/G). Moreover, water induces the O_2 dissociation by lowering the activation barrier by ~0.2 eV on all substrates due to the H bond effect between water and O_2 [65-66]. In contrast, the O_2 protonation to OOH* exhibits higher activation energy (~0.88 eV on sp-N1GDY/G and ~1.41 eV on sp-N2GDY/G) compared with that of O_2 dissociation. Consequently, I assume the ORR mechanism on sp-N doped catalysts will follow the dissociative mechanism ($O_2 \rightarrow 2O^* \rightarrow O^*+OH^* \rightarrow O^* \rightarrow OH^* \rightarrow H_2O$). On the Pyri-NGDY/G surface, the O–O bond of O_2 does not activate upon the adsorption due to its physisorption state. From Table 5.1, protonation to OOH* has lower activation energy than its dissociation with one water (1.17 eV vs. 1.35 eV), however, this protonation barrier (1.17 eV) is still rather high, thus protonation process is kinetically unfavorable due to physisorption O_2.

It is noted that even though O_2 is weakly adsorbed and the activation barrier for the direct protonation of the adsorbed O_2 is high, ORR can still proceed with high activities on carbon materials via different reaction pathway, namely, a process of long-range electron-transfer (ET) to nonadsorbed O_2 in the outer Helmholtz plane (ET-OHP) [67-68]. Choi *et al.* [68] recently revealed that the first proton-coupled electron transfer (PCET) step (O_2(aq) + ($H^+ + e^-$) → •OOH (aq)) can occur via the ET-OHP, where O_2 directly form •OOH (aq). Then •OOH (aq) subsequently adsorbs on the catalytic site as OOH* (i.e., ET-OHP mechanism). This well explains the problem of not finding suitable sites for O_2 binding on N-doped graphene and shows that the O_2 chemisorption is not essential for ORR occurring on carbon-based catalysts.

I find that O_2 could not chemisorb and the O_2 protonation barrier (1.17 eV) is high on Pyri-NGDY/G. But OOH* can chemisorb on the surface with an ΔE_{ads} of -0.93 eV (Table 5.1). Therefore, I assume the ORR on Pyri-NGDY/G follows the ET-OHP associative mechanism ($O_2 \rightarrow OOH^* \rightarrow O^* \rightarrow OH^* \rightarrow OH^-$).

Next, the reaction and adsorption Gibbs free energies of ORR intermediates on three N-doped models, ie., sp-N1GDY/G, sp-N2GDY/G, and Pyri-NGDY/G were calculated and shown in Figure 5.3, Figure C.4 and Table C.4-C.6 for all considered systems. I find that ORR proceeds with rather high η on three substrates. For Pyri-NGDY/G (Figure 5.3 (e)), the η is 1.01 V, and the potential-determining step (PDS) is the $O_2 \rightarrow OOH^*(\Delta G_6)$. And high η of ORR on sp-N1GDY/G (Figure 5.3 (a)) and sp-N2GDY/G (Figure S5.4 (a)) arises from the strong interactions of ORR intermediates with substrate. The PDS for ORR on N doped catalyst in sp-N configurations is found to be the last step $OH^* \rightarrow OH^-$ (ΔG_5). The third ORR steps ($O^*+OH^* \rightarrow O^*$) are exergonic and become endergonic upon applying a potential of 1.23 V. The last steps ($OH^* \rightarrow OH^-$) are endergonic reactions even at $U_{RHE} = 0$ V (0.13 eV on sp-N1GDY/G and 0.38 eV on sp-N2GDY/G), showing that OH* has strong binding energy with the surface and hard to further hydrogenation. As a result, the first ORR could not be completed and some ORR intermediates like O* or OH* remain adsorbed on sp-NGDY/G.

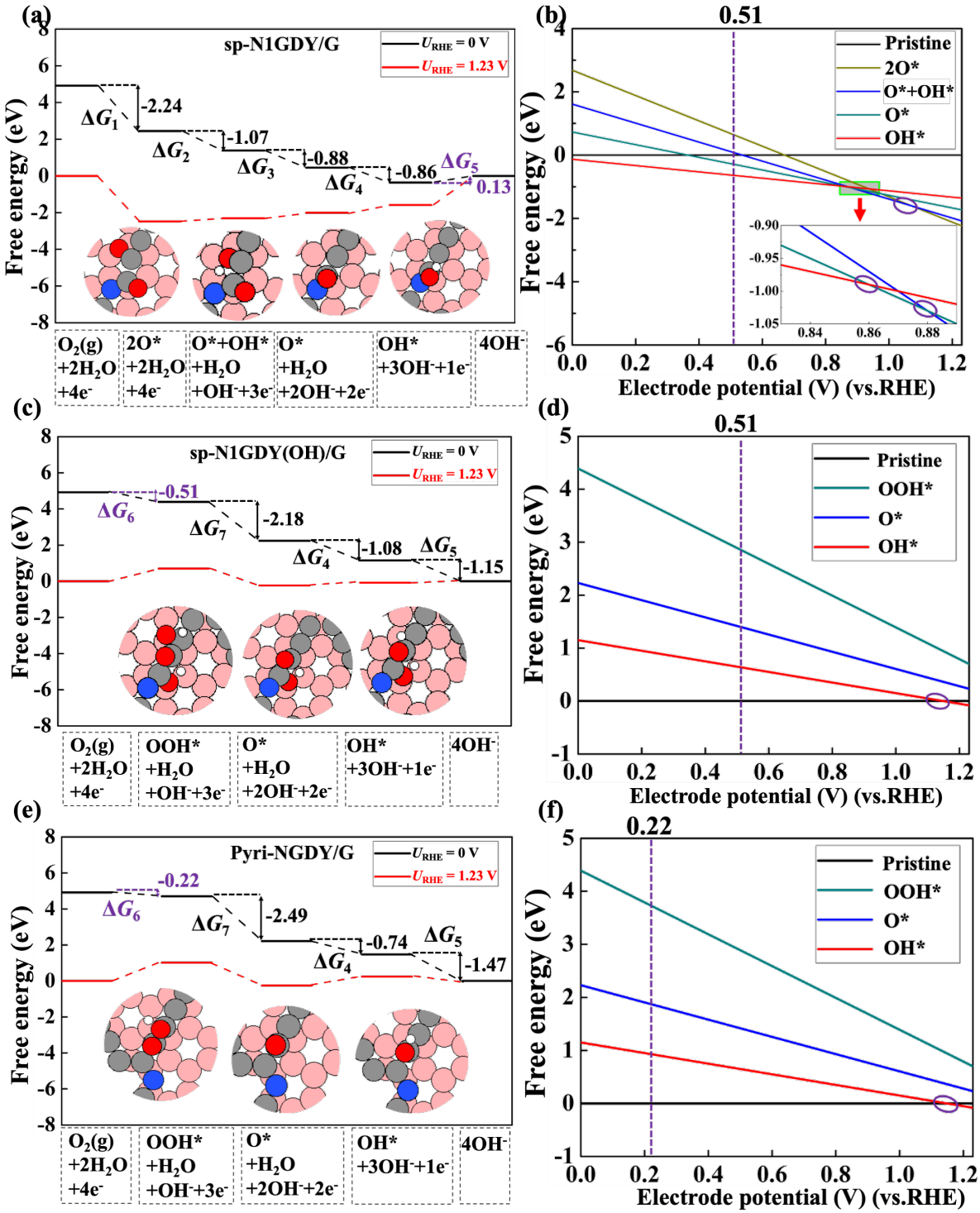

Figure 5.3: (a) Free energy diagram and structures of each ORR intermediate on sp-N1GDY/G and (b) free energy of each ORR intermediate versus electrode potential (vs. RHE) on sp-N1GDY/G. (c) Free energy diagram and structures of each ORR on sp-N1GDY(OH)/G and (d) free energy of each ORR intermediate versus electrode potential (vs. RHE) on sp-N1GDY(OH)/G. (e) Free energy diagram and structures of each ORR intermediate on Pyri-

NGDY/G and (f) free energy of each ORR intermediate versus electrode potential (vs. RHE) on Pyri-NGDY/G. The purple circles are representing the lowest lines crossed at different potentials. Pristine in (b), (d) and (f) represents sp-N1GDY/G, sp-N1GDY(OH), and Pyri-NGDY/G, respectively. Red, white, gray, pink, and blue balls are O atoms, H atoms, C atoms in N-doped GDY, C atoms in G, and N atoms, respectively. U_{RHE} is the potential of the electrode relative to the RHE.

To confirm this, the adsorption Gibbs free energy of each ORR intermediate as a function of the U_{RHE} is evaluated. From Figure 5.3 (b), sp-N1GDY/G is terminated by OH* at 0 V < U_{RHE} < 0.86 V, by O* at 0.86 V < U_{RHE} < 0.88 V, by O*+OH* at 0.88 V < U_{RHE} < 1.07 V, and by 2O* at 1.07 V < U_{RHE} < 1.23 V. Similarly, for sp-N2GDY/G (Figure S5.6(b)), sp-N2GDY/G is terminated by OH* at 0 V< U_{RHE} < 0.49 V, by O* at 0.49 V < U_{RHE} < 0.73 V, and by 2O*at 0.73 V < U_{RHE} < 1.23 V. In contrast, on the Pyri-NGDY/G surface, the most stable structure will be Pyri-NGDY/G pristine surface under 0 V < U_{RHE} <1.11 V (Figure 5.3 (f)). It should be noted that in this work, I only consider single ORR intermediates as a function of potential, the coverage [69] of ORR intermediates may or may not affect the results, this subject will be investigated in the next project.

Consequently, upon applying a limiting potential of 0.22 V, the complete ORR process occurs on Pyri-NGDY/G, and ORR species will never be terminated on the surface. In contrast, OH* will be terminated on sp-N1GDY/G and sp-N2GDY/G surfaces without any potential applied (sp-N1GDY(OH)/G and sp-N2GDY/G hereafter). Therefore, I explore the ORR mechanism on sp-N1GDY(OH)/G and sp-N2GDY(OH)/G in the next subsection.

ORR mechanisms on OH pre-adsorbed surface. I find that the strengths of O_2 adsorption are decreased upon the adsorptions on sp-N1GDY(OH)/G and sp-N2GDY(OH)/G compared with that on clean surfaces. As shown in Table 5.1 and Table C.3, the vdW attractions dominate the interaction between O_2 and sp-N1GDY(OH)/G, resulting the ΔE_{ads} of

O_2 and distance between O_2 and sp-N1GDY(OH)/G is −0.15 eV and 3.0 Å, respectively. While, on sp-N2GDY(OH)/G, O_2 is weakly chemisorbed with ΔE_{ads} of −0.58 eV and adsorption distance of 1.426 Å. Then, the E_a of the O_2 dissociation and protonation on sp-N1GDY(OH)/G and sp-N2GDY(OH)/G using the CI-NEB method was shown in Table 5.1 and Figure C.5. I obtain a high activation energy of O_2 dissociation and protonation of 1.40 eV on sp-N1GDY(OH)/G, thus the ET-OHP associative mechanism is assigned for ORR on this surface. On the other hand, for sp-N2GDY(OH)/G, O_2 dissociation is more favorable than O_2 protonation, thus I assume ORR will proceed based on the dissociative mechanism.

The free energy diagram, reaction, and adsorption Gibbs free energy of ORR intermediates on sp-N1GDY(OH)/G and sp-N2GDY(OH)/G was shown in Figure 5.3(c), Figure C.4 (c), and Table C.4-C.6. For sp-N1GDY(OH)/G, the stability of three ORR intermediates, i.e., OOH*, O*, and OH* are estimated. I find that all ORR intermediates preferably adsorb on top sites of the neighboring C atom of the –COH–N moiety. The interactions between sp-N1GDY(OH) and intermediates become weak after involving OH* pre-adsorbed. The ΔG_{OH*} of sp-N1GDY(OH)/G is 1.15 eV larger than that of sp-N1GDY/G (−0.13 eV), indicating that pre-adsorbed OH* is improving rather than poisoning. Moreover, the PDS is $O_2 \rightarrow$ OOH* with a limiting potential of 0.51 eV and η of 0.72 V (Table 5.2). In Figure 5.3(b) and Figure 5.3(d), I also can prove that under $U_{RHE} = 0.51$ V, sp-N1GDY(OH) is the most stable structure. For sp-N2GDY(OH)/G, we found 2O* → O*+OH* is a strongly endergonic reaction with ΔG_2 of 1.06 eV (Figure C.4 (c) and Table C.5), which will cause possible active sites poisoned by 2O*. Therefore, sp-N2GDY/G cannot be an ORR electrocatalyst.

In vacuum conditions, I identify that sp-N1GDY(OH)/G can create a conceivable active site for ORR with low overpotential. The clean sp-N1GDY/G surfaces are easily terminated

by OH* intermediate and the neighboring C site of –COH–N moiety of sp-N1GDY(OH)/G is the real active sites for ORR to proceed with low η compared with Pyri-NGDY/G.

Electronic structure of active site relates to O_2 activation. In general, the interactions between C 2p of active sites and O_2 π^* orbitals govern the adsorption strength of O_2 and the elongation of O_2 upon adsorption on substrate. Hybridizations between C 2p and O_2 π^* orbitals facilitate the back donation to π^* orbitals, thus increasing the occupations of this orbitals upon adsorption (Figure C.6). As the results, the PDOS of C 2p near Fermi level is quite important to determine O_2 adsorption and O_2 dissociation barrier.

I plotted the PDOS of C 2p of the active site in sp-N1GDY/G, sp-N2GDY/G, sp-N1GDY(OH)/G, sp-N2GDY(OH)/G, and Pyri-NGDY/G. In Figure 5.4 (a), at the Fermi level, there is almost no partially occupied state of C 2p in sp-N1GDY(OH)/G and Pyri-NGDY/G, while for sp-N1GDY/G, sp-N2GDY/G, and sp-N2GDY(OH)/G, there exists partially occupied state of C 2p. In Figure 5.4 (b), I also find there is linear relationship between PDOS height value at the Fermi level and adsorption energy of O_2. The results can also prove that the presence of partially occupied state of C 2p of active site can induce the O_2 adsorption. Therefore, upon adsorption of O_2, there is almost no hybridization in sp-N1GDY(OH)/G and Pyri-NGDY/G, thus the adsorption energies are weak (-0.15 eV and -0.10 eV) and O_2 dissociation barrier is high (1.86 eV and 1.52 eV). On the other hand, O_2 has strong hybridizations with C on sp-N1GDY/G, sp-N2GDY/G and sp-N2GDY(OH)/G due to the presence of partially occupied state. The adsorption energy (-0.6 eV, -1.37 eV and -0.58 eV) and NEB barrier (0.22 eV, 0.08 eV and 0.81 eV) results show that O_2 is chemisorbed and easy to dissociate on sp-N1GDY/G, sp-N2GDY/G, and sp-N2GDY(OH)/G, respectively.

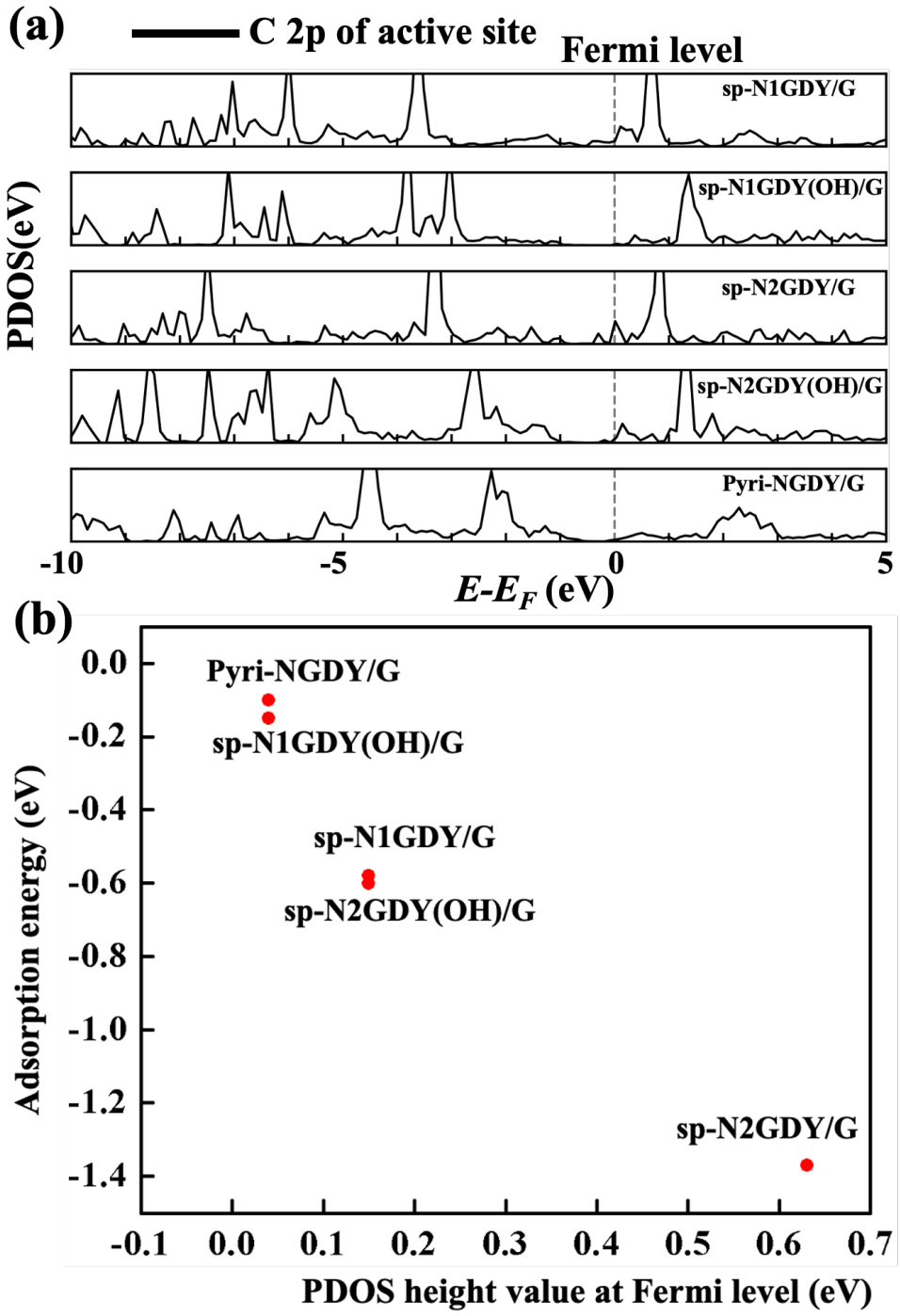

Figure 5.4: (a) PDOS of C 2p of active site in sp-N1GDY/G, sp-N1GDY(OH)/G, sp-N2GDY/G, sp-N2GDY(OH)/G, and Pyri-NGDY/G. (b)The relationship between PDOS height value at Fermi level and adsorption energy of O_2.

Table 5.2: The overpotential (η) and potential-determining step (PDS) of ORR on sp-N1GDY(OH), sp-N1GDY(OH)/G, Pyri-NGDY, and Pyri-NGDY/G with/without water using RPBE+D2 and PBE+D2, respectively.

	RPBE+D2		PBE+D2	
	η	PDS	η	PDS
sp-N1GDY(OH)	0.75	$O_2 \rightarrow OOH^*$	—	—
sp-N1GDY(OH)/G	0.72	$O_2 \rightarrow OOH^*$	0.54	$O_2 \rightarrow OOH^*$
sp-N1GDY(OH)/G with water	0.46	$O_2 \rightarrow OOH^*$	0.54	$OH^* \rightarrow OH^-$
Pyri-NDGY	1.17	$O_2 \rightarrow OOH^*$	—	—
Pyri-NDGY/G	1.01	$O_2 \rightarrow OOH^*$	0.89	$O_2 \rightarrow OOH^*$
Pyri-NDGY/G with water	0.75	$O_2 \rightarrow OOH^*$	0.65	$O^* \rightarrow OH^*$
experiment [20]		η =0.36		

5.3.3 The ORR Mechanism and Free Energy Analysis on sp-N1GDY/G and Pyri-NGDY/G in Water Conditions

Experimentally, electrochemical reactions occur at solid/liquid interfaces, thus it is necessary to incorporate solvation effects in an explicit water environment when investigating the ORR using the CHE model. The solvation energy of the ORR intermediate can estimate from the AIMD simulation of the adsorbed systems with water solvents explicitly. However, this approach requires a huge computational cost. To this end, I first simulate the interfaces of NGDY's, namely sp-N1GDY/G and Pyri-NGDY/G with water to elucidate the H bond networks. Next, I only keep the water configurations in the contact region with the surface of the five most stable AIMD snapshots of clean systems and replace one nearest water molecule above the active site by each ORR intermediate to construct the H bond networks of ORR intermediate and water. The ΔSol of each ORR intermediate is then elucidated from an average of five AIMD snapshots. Moreover, I also construct an H bond networks by the ice-like bilayer model.

To distinguish the water region, the average density profiles of H_2O (ρ) as a function of Z position on the sp-N1GDY/G (Figure 5.5 (a)) and Pyri-NGDY/G (Figure 5.5 (b)) are shown in Figure 5.5. In both cases, the first sharply density peak of ρ is located at c.a. -3 Å

(surface is located at c.a. −6 Å) and extends up to -1 Å. Therefore, the region with −6.0 Å < Z <−1.0 Å is defined as the contact region between N-doped GDY and water solvents. The water density of the contact region is estimated to be around 1.4 g·cm^{-3}, which is similar to that of the water/graphene interface surfaces [70]. Within the region of −1.0 Å < Z < 7.0 Å, water density oscillated and gradually decreased the bulk water density (~1.0 g·cm^{-3}). Thus, I defined this region as the "bulk" water region. Above 7.0 Å until 9.3 Å (artificial boundary) appears another peak, called the water contact region with the vacuum. I mainly focus on the contact region with the surface (−6.0 Å < Z < −1.0 Å) to investigate the H bond networks.

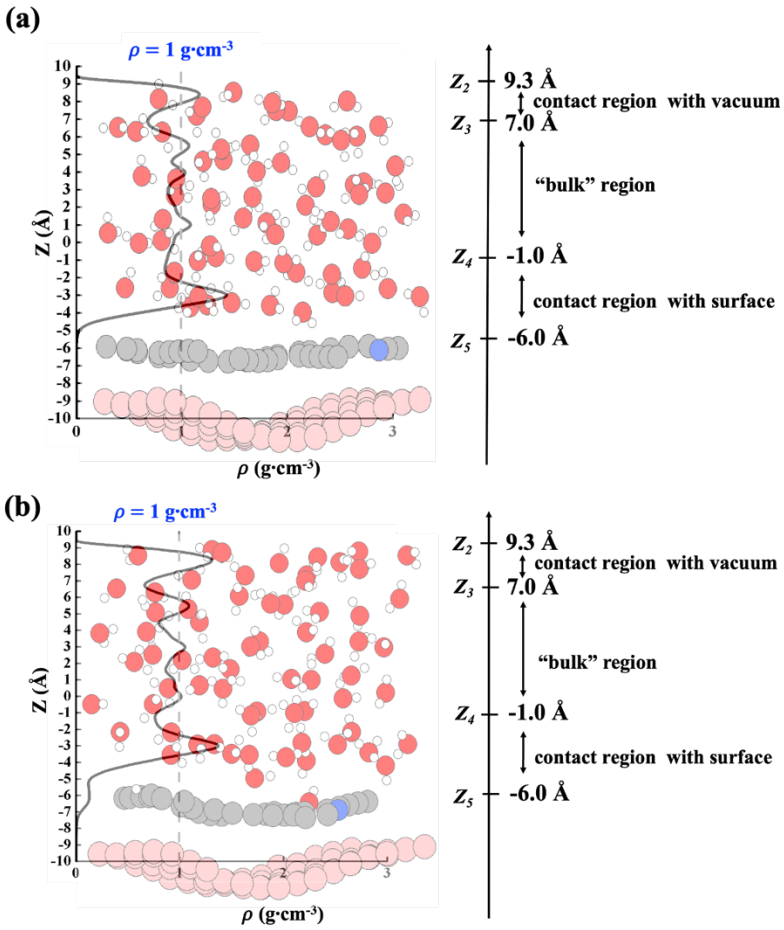

Figure 5.5: Calculated average density profile for the sp-N1GDY/G with water (a) and Pyri-NGDY/G with water (b) at 400 K. The gray solid line indicates the average atomic density, and the gray dashed line indicates the density of bulk water (1 g·cm^{-3}). Red, white, gray, pink,

and blue balls are O atoms, H atoms, C atoms in N-doped GDY, C atoms in G, and N atoms, respectively.

Structural properties of water/N doped GDY are evaluated by RDF and average coordination number (N_{OO}) of H_2O. I calculate and plot the radial distribution functions (RDFs) between oxygen atoms, R(r) and N_{OO} of the "bulk" region and the contact layer with the surface on sp-N1GDY/G and Pyri-NGDY/G are shown in Figure 5.6 and Table 5.3. The RDF(s) curve and N_{OO} of the "bulk" region in both cases are similar to that obtained from the experiment at around 400 K [71-72]. The higher temperatures result in an overall softening of the structure, with diminishment of the first and second peaks, and a rise in the first minimum (r_{min} = 3.6 Å) compared with that at room temperature (r_{min} = 3.3 Å). I performed the average coordination number (N_{OO}) of H_2O in the contact region with the surface (-6.0 Å < Z < -1.0 Å) on both cases averaged over 5 ps (Figure 5.7). The results suggest that in 15 ps, the coordination number of water molecules is basically unchanged.

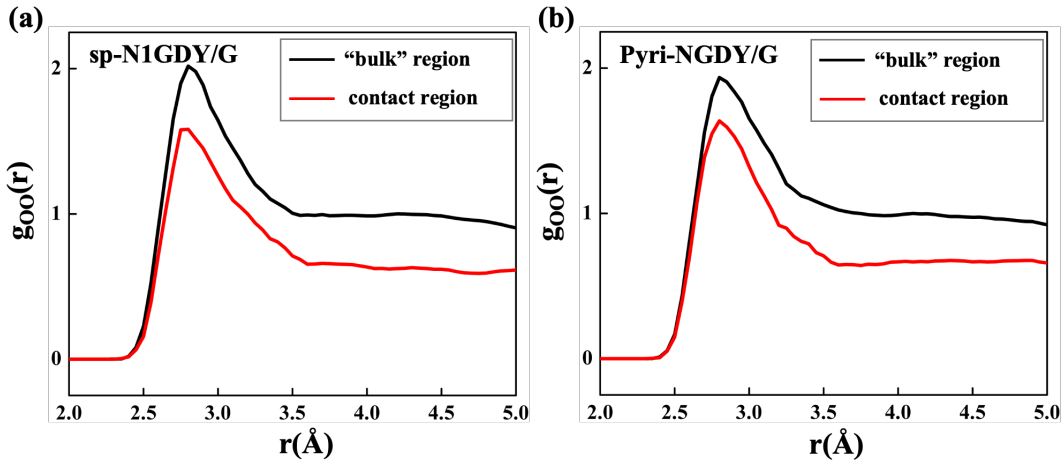

Figure 5.6: Oxygen-oxygen radial distribution function ($g_{OO}(r)$) for the "bulk" region (black line) and for the contact region with the surface (red line) on sp-N1GDY/G (a) and Pyri-NGDY/G (b).

Table 5.3: Coordination number N_{oo} of the contact layer and the "bulk" region, Temperature (T), the value of first minimum r_{min} in the $g_{OO}(r)$ of N-doped GDY/G compared with that of experiment values for bulk water.

	bulk water				contact region water			
	r_{max}	r_{min}	N_{OO}	T	r_{max}	r_{min}	N_{OO}	T
sp-N1GDY/G	2.8	3.6	5.30	400	2.8	3.6	4.06	400
Pyri-NGDY/G	2.8	3.6	5.27	400	2.8	3.6	4.08	400
Experiment [71]	2.8	3.6	5.20	423	—	—	—	—

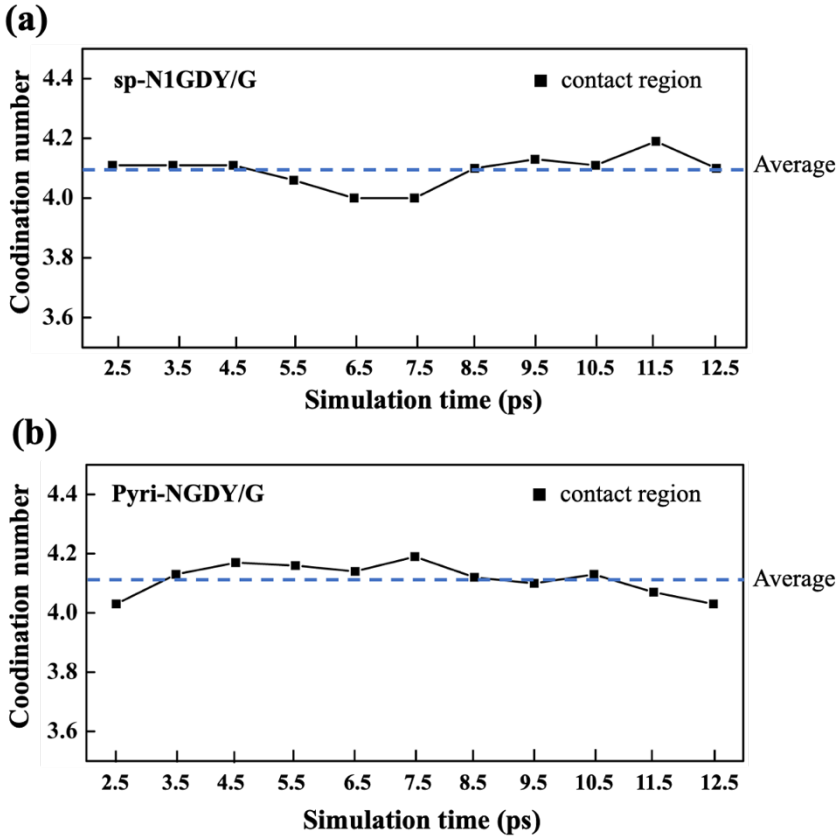

Figure 5.7: The average coordination number of H_2O in contact region with the surface (-6.0 Å $< Z < -1.0$ Å) on sp-N1GDY/G (a) and Pyri-NGDY/G (b) over a varying length of 5 ps.

The H bond networks of water on sp-N1GDY/G and Pri-NGDY/G surfaces are shown in Figure C.7. On both substrates, the water layer of the H bond networks at the contact region with N-doped GDY is mainly composed of the six-membered ring component after

optimization, i.e., one H_2O has three H bonds with neighbor three H_2O. This is similar to the ice-like bilayer that is often observed for water/flat metal interfaces [28,73]. The ΔSol of 2O*, O*+OH*, O*, and OH* on sp-N1GDY/G and the ΔSol of OOH*, O*, and OH* on sp-N1GDY(OH)/G or Pyri-NGDY/G are shown in Table C.7-C.8. I find water stabilizes all ORR intermediates, which arise from H bonds with water. Moreover, I also calculate the ΔSol of each ORR intermediate using ice-like bilayer (Table C.7-C.8). The results showed that the difference in the ΔSol‘s between the H bond network model from AIMD and the ice-like bilayer model varies by only ~0.1 eV. I find that the ΔSol of these surfaces is independent of the water model, which arises from similar H bonds between adsorbates and water in the ice-like bilayer and AIMD H bond networks.

The free energy diagram of ORR with water on sp-N1GDY/G, sp-N1GDY(OH)/G, and Pyri-NGDY/G is shown in Figure 5.8. Because of the stabilization driven by solvation effect, reaction Gibbs free energies of all ORR intermediates are more stable than that in vacuum conditions. Thus, OH* is more easily terminated on sp-N1GDY/G surface (Figure 5.8 (a) and 5.8 (b)) and further ORR steps are considered on sp-N1GDY(OH)/G (Figure 5.8 (c) and 5.8 (d)). The PDS of ORR on sp-N1GDY(OH)/G in water remains the same as that in vacuum conditions ($O_2 \rightarrow$ OOH*), while the limiting potential is changed from 0.51 V in the vacuum condition to 0.77 V in water conditions. At $U_{\mathrm{RHE}} = 0.77$ V (Figure 5.8 (b) and 5.8 (d)), sp-N1GDY(OH) is the most stable structure in water conditions. Therefore, introducing the ΔSol, the η of sp-N1GDY(OH)/G is 0.46 V (Table 5.2) which is close to the experimentally reported value (0.36 V). Similarly, On Pyri-NGDY/G, even though solvation effect is included, the PDS of ORR on Pyri-NGDY/G in water conditions does not change compared with that in vacuum conditions ($O_2 \rightarrow$ OOH*). I obtain a limiting-potential increase to 0.48 eV (Figure 5.8 (e) and

5.8 (f)) and an η decrease to 0.75 V (Table 5.2), which is higher than that of sp-N1GDY(OH)/G. Finally, I conclude that ORR easily proceeds on sp-N1 doping with OH* pre-adsorbed.

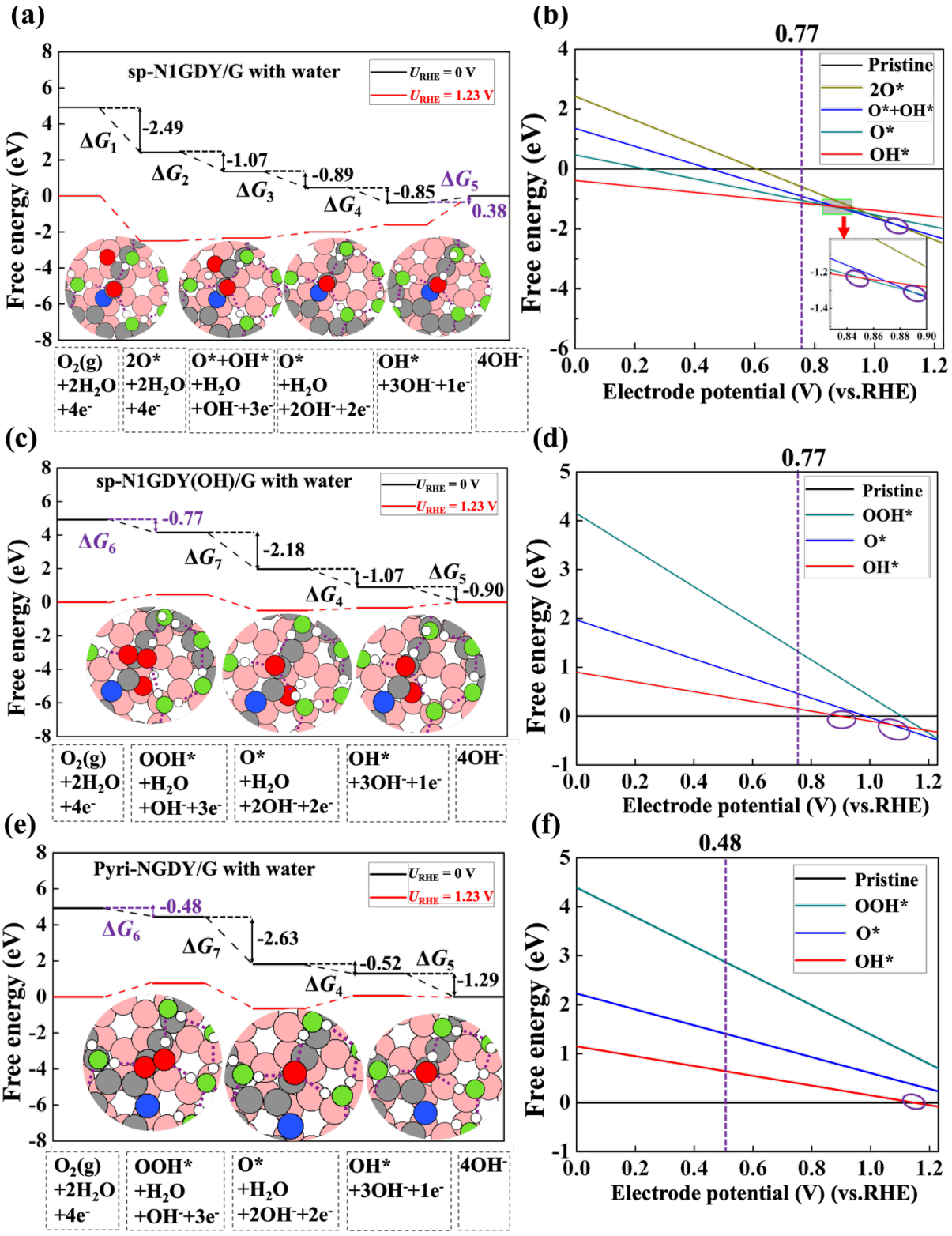

Figure 5.8: (a) Free energy diagram and structures of each ORR intermediate with water on sp-N1GDY/G. (b) Free energy of each ORR intermediate with water versus electrode potential

(vs. RHE) on sp-N1GDY/G. (c) Free energy diagram and structures of each ORR intermediate with water on sp-N1GDY(OH)/G. (d) Free energy of each ORR intermediate with water versus electrode potential (vs. RHE) on sp-N1GDY(OH)/G. (e) Free energy diagram and structures of each ORR intermediate with water on Pyri-NGDY/G. (f) Free energy of each ORR intermediate versus electrode potential (vs. RHE) on Pyri-NGDY/G. Pristine in (b), (d) and (f) represents sp-N1GDY/G, sp-N1GDY(OH) and Pyri-NGDY/G, respectively. U_{RHE} is the potential of the electrode relative to the RHE. Red, green, white, gray, pink, and blue balls are O atoms in ORR intermediates, O atoms in water, H atoms, C atoms in N-doped GDY, C atoms in G, and N atoms, respectively. The purple dashed lines in structures represent the H bond networks. I regard an H bond as being formed when the O–O distance of adjacent water molecules is smaller than 3.5 Å and the angle between the O–H vector of one molecule and the O–O vector is smaller than 30° in [74].

5.3.4 Effects of Exchange-Correlation Energy Functionals and Graphene Support on ORR

I here discuss the effect of exchange correlation energy functionals on the adsorption free energy of ORR. I employ the PBE+D2 energy functional to perform the adsorption Gibbs free energy of ORR on sp-N1GDY/G, sp-N1GDY(OH)/G, and Pyri-NGDY/G with and without water. As shown in Table C.9, I find that PBE tends to overestimate the binding energy of chemisorption species. This is due to the overestimation of attractive interactions in molecular systems. In vacuum conditions, the adsorption Gibbs free energies of ORR intermediates on sp-N1GDY/G, sp-N1GDY(OH)/G, and Pyri-NGDY/G are more stable using PBE+D2 compared with using RPBE+D2. Thus, the η of ORR on sp-N1GDY(OH)/G and Pyri-NGDY/G is slightly decreased using PBE+D2 compared with RPBE+D2. However, the trend of ORR activity remains the same, which is sp-N1GDY(OH)/G > Pyri-NGDY/G. In water

conditions, here, I only use the ice-like bilayer water to simulate the ΔSol because I already proved that the ΔSol using the H bond networks from AIMD is not much different from that using the ice-like bilayer water based on RPBE+D2 energy functional. Table C.10 showed that the ΔSol of each ORR intermediate is more negative using PBE+D2 energy functional compared with that using RPBE+D2 energy functional. For Pyri-NGDY/G with water, the η is decreased to 0.65 V (Table 5.2) and PDS is changed from $O_2 \rightarrow$ OOH* (vacuum conditions) to O → OH* (water conditions). For sp-N1GDY(OH)/G, PDS is changed from $O_2 \rightarrow$ OOH* (vacuum conditions) to OH* → OH^- (water conditions) but η is coincidentally not changed (0.54 V) (Table 5.2). Although the trend of ORR activity in water is unchanged, the η of sp-N1GDY(OH)/G using RPBE+D2 (0.46 V) is closer to the experimental result (0.36 V) compared with that using PBE+D2 (0.54 V). Therefore, RPBE+D2 energy functional gives more reasonable binding energies and solvation energies of adsorbates.

In the 5.3.1 section, I find G support on NGDY enhances the metallic property and causes charge transfer from G to NGDY. To investigate the G support effect for ORR electrocatalytic activity, calculated adsorption free energies of ORR with G support and without G support are shown in Table C.5 and C.6. The results reveal that the G support stabilizes all ORR intermediates in these cases, especially on Pyri-NGDY, which stabilizes ~0.2 eV on OOH*, O*, and OH* (Table C.6). Higher charge transfer from G to substrate as indicated by work function change upon graphene support (0.31 eV for Pyri-NGDY/G vs. 0.13 eV for sp-N1GDY/G) results in a strong interaction of ORR intermediates with N-doped GDY. In a word, introducing G support enhances the ORR electrocatalytic activity of N-doped GDY.

5.4 Summary

In summary, I performed the DFT calculations and AIMD simulations to investigate the ORR mechanism on the sp-N1GDY/G and Pyri-NGDY/G with and without solvation effect. ORR firstly proceeds on sp-N1GDY/G via the dissociative mechanism because O_2 can be chemisorbed on a clean surface and easily dissociated rather than protonated to OOH*. However, OH* is strongly adsorbed on the sp-N1GDY/G surface, resulting in the weakening of the second O_2 adsorption, and ORR takes place via the ET-OHP associative mechanism. Pyri-NGDY/G also prefers the ET-OHP associative mechanism. The H bond networks from AIMD simulation at the interface are mainly composed of six-membered rings H bond networks. H bond with water stabilizes each ORR intermediate and the free energy diagram with solvation effect agrees well with experimental data. OH* pre-adsorbed on sp-N1GDY/G surface possesses highest ORR electrocatalytic activity and the neighboring C site of –COH–N moiety is the active site for ORR. Incorporation of solvation effect is of importance because η with solvation effect (0.46 V) is much closer to the experimental one (0.36 V). My work highlights the importance of considering solvation effect in designing and optimizing catalysts for ORR and other chemical reactions.

References

[1] Br. C. H. Steele, H. Angelika, Nature, **414**, 345-352 (2001).

[2] J. Kui, J. Xuan, Q. Du, Z. Bao, B. Xie, B. Wang, Y. Zhao, L. Fan, H. Wang, Z. Hou, S. Hu, N. P. Brandon, Y. Yin, M. D. Guiver, Nature, **595**, 361-369 (2021).

[3] D. Larcher, J. M. Tarascon, Nat. Chem., **7**, 19-29 (2015).

[4] R. Ma, G. Lin, Y. Zhou, Q. Liu, T. Zhang, G. Shan, M. Yang, J. Wang, Npj Comput. Mater., **5**, 78 (2019).

[5] S. Sui, X. Wang, X. Zhou, Y. Su, S. Riffat, C. J. Liu, J. Mater. Chem. A., **5**, 1808-1825 (2017).

[6] L. Dai, Y. Xue, L. Qu, H. J. Choi, J. B. Baek, Chem. Rev., **115**, 4823-4892 (2015).

[7] K. Gong, F. Du, Z. Xia, M. Durstock, L. Dai, Science, **323**, 760-764 (2009).

[8] D. Guo, R. Shibuya, C. Akiba, S. Saji, T. Kondo, J. Nakamura, Science, **351**, 361-365 (2016).

[9] S. Tang, X. Zhou, T. Liu, S. Zhang, T. Yang, Y. Luo, E. Sharman, J. Jiang, J. Mater. Chem. A, **7**, 26261-26265 (2019).

[10] S. Tang, Q. Dang, T. Liu, S. Zhang, Z. Zhou, X. Li, X. Wang, E. Sharman, Y. Luo, J. Jiang, J. Am. Chem. Soc., **142**, 19308-19315 (2020).

[11] C. Z. Yuan, H. B. Li, Y. F. Jiang, K. Liang, S. J. Zhao, X. X. Fang, L. B. Ma, T. Zhao, C. Lin, A. W. Xu, J. Mater. Chem. A, **7**, 6894-6900 (2019).

[12] L. Jian, X. Gao, B. Liu, Q. Feng, X. B. Li, M. Y. Huang, Z. Liu, J. Zhang, C. H. Tung, L. Z. Wu, J. Am. Chem. Soc., **138**, 3954-3957 (2016).

[13] G. Xin, H. Liu, D. Wang, J. Zhang, Chem. Soc. Rev., **48**, 908-936 (2019).

[14] Y. Fang, Y. Liu, L. Qi, Y. Xue, Y. Li, Chem. Soc. Rev., **51**, 2681-2709 (2022).

[15] Y. Li, L. Xu, H. Liu, Y. Li, Chem. Soc. Rev., **43**, 2572-2586 (2014).

[16] C. Huang, Y. Li, N. Wang, Y. Xue, Z. Zuo, H. Liu, Y. Li, Chem. Rev., **118**, 7744-7803 (2018).

[17] Z. Zuo, Y. Li, Joule, **3**, 899-903 (2019).

[18] Y. Gao, Z. Cai, X. Wu, Z. Lv, P. Wu, C. Cai, ACS Catal., **8**, 10364-10374 (2018).

[19] Z. Feng, R. Li, Y. Ma, Y. Li, D. Wei, Y. Tang, X. Dai, Phys. Chem. Chem. Phys., **21**, 19651-19659 (2019).

[20] Y. Zhao, J. Wan, H. Yao, L. Zhang, K. Lin, L. Wang, N. Yang, D. Liu, L. Song, J. Zhu, L. Gu, L. Liu, H. Zhao, Y. Li, D. Wang, Nat. Chem., **10**, 924-931 (2018).

[21] T. Lu, X. Hu, J. He, R. Li, J. Gao, Q. Lv, Z. Yang, S. Cui, C. Huang, Nano Energy, **85**, 106024 (2021).

[22] X. Chen, W. J. Ong, Z. Kong, X. Zhao, N. Li, Sci. Bull., **65**, 45-54 (2020).

[23] B. Kang, S. Wu, J. Ma, H. Ai, J. Y. Lee, Nanoscale, **11**, 16599-16605 (2019).

[24] J. Gu, S. Magagula, J. Zhao, Z. Chen, Small Methods, **3**, 1800550 (2019).

[25] J. K. Nørskov, J. Rossmeisl, A. Logadottir, L. Lindqvist, J. R. Kitchin, T. Bligaar, H. Jónsson, J. Phys. Chem. B, **108**, 17886-17892 (2004).

[26] L. Yu, X. Pan, X. Cao, P. Hu, X. Bao, J. Catal., **282**, 183-190 (2011).

[27] P. S. Rice, Y. Mao, C. Guo, P. Hu, Phys. Chem. Chem. Phys., 21, 5932-5940 (2019).

[28] S. Schnur, A. Groß, New J. Phys., **11**, 125003 (2009).

[29] Groß, S. Sung, Chem. Rev., **122**, 10746-10776 (2022).

[30] S. N. Steinmann, P. Sautet, C. Michel, Phys. Chem. Chem. Phys., **18**, 31850-31861 (2016).

[31] J. Ho, M. Z. Ertem, J. Phys. Chem. B, **120**, 1319-1329 (2016).

[32] G. König, B. Stefan, J. Phys. Chem. B, **113**, 8967-8974 (2009).

[33] H. Cao, G. J. Xia, J. W. Chen, H. M. Yan, Z. Huang, Y. G. Wang, J. Phys. Chem. C, **124**, 7287-7294 (2020).

[34] M. Reda, H. A. Hansen, T. Vegge, Catal. Today, **312**, 118-125 (2018).

[35] Y. Morikawa, Phys. Rev. B: Condens. Matter Mater. Phys., **51**, 14802-14805 (1995).

[36] Y. Hamamoto, I. Hamada, K. Inagaki, Y. Morikawa, Phys. Rev. B: Condens. Matter Mater. Phys., **93**, 245440 (2016).

[37] Y. Morikawa, K. Iwata, K. Terakura, Appl. Surf. Sci., **11**, 169-170 (2000).

[38] S. A. Wella, Y. Hamamoto, F. Iskandar, Suprijadi, Y. Morikawa, I. Hamada, J. Chem. Phys., **152**, 104707 (2020).

[39] D. Vanderbilt, Phys. Rev. B, **41**, 7892-7895 (1990).

[40] B. Hammer, L. B. Hansen, J. K. Nørskov, Phys. Rev. B, **59**, 7413 (1999).

[41] S. Grimme, J. Comput. Chem., **27**, 1787-1799 (2006).

[42] G. Henkelman, H. Jonsson, J. Chem. Phys., **113**, 9978-9985 (2000).

[43] G. Henkelman, B. P. Uberuaga, H. Jónsson, J. Chem. Phys., **113**, 9901-9904 (2000).

[44] S. P. Chan, G. Chen, X. G. Gong, Z. F. Liu, Phys. Rev. Lett., **90**, 086403 (2003).

[45] J. I. Enriquez, F. Muttaqien, M. Michiuchi, K. Inagaki, M. Geshi, I. Hamada, Y. Morikawa, Carbon, **174**, 36-51 (2021).

[46] C. Man, H. Y. Su, F. C. Vallejo, H. A. Hansen, J. I. Martinez, N. G. Inoglu, J. Kitchin, T. F. Jaramillo, J. K. Nørskov. J. Rossmeisl, ChemCatChem, **3**, 1159-1165 (2011).

[47] Q. Liang, G. Brocks, A. B. Hütter, J. Phys. Energy, **3**, 026001 (2021).

[48] C. J. Cramer. Essentials of Computational Chemistry, Second Edition. Wiley, 2004.

[49] D. R. Lide, CRC handbook of physics and chemistry, CRC Press, Boca Raton, USA, **76**, 1995-1996 (2001).

[50] R. C. Weast, Handbook of chemistry and physics, Chemical Rubber Co., Cleveland, OH, C528-C529 (1971).

[51] Rossmeisl, A. Logadottir, and J. K. Nørskov, Chem. Phys., **319**, 178 (2005).

[52] K. Nørskov, F. Studt, F. Abild-Pedersen, T. Bligaard, Fundamental Concepts in Heterogeneous Catalysis (New York, NY: Wiley), 2014.

[53] J. Li, H. M. Yin, X. B. Li, E. Okunishi, Y. L. Shen, J. He, Z. K. Tang, W. X. Wang, E. Yücelen, C. Li, Y. Gong, L. Gu, S. Miao, L. M. Liu, J. Luo, Y. Ding, Nat. Energy, **2**, 17111 (2017).

[54] R. Iftimie, P. Minary, M. E. Tuckerman, PNAS, **102**, 6654-6659 (2005).

[55] Otani, O. Sugino, Phys. Rev. B: Condens. Matter Mater. Phys., **73**, 115407 (2006).

[56] S. Yoo, Z. C. Xiao, S. X. Sotiris, J. Chem. Phys., **130**, 221102-221104 (2009).

[57] X. Chen, Y. Zhang, Y. Ren, D. Wang, J. Yun, Mater. Res. Express, **6**, 095610 (2019).

[58] V. M. Karpan, G. Giovannetti, P. A. Khomyakov, M. Talanana, A. A. Starikov, M. Zwierzycki, J. V. D. Brink, G. Brocks, P. J. Kelly, Phys. Rev. Lett., **99**, 176602 (2007).

[59] S. Haile, H. A. Hansen, W. Yohannes, Y. S. Mekonnen, J. Phys. Chem. Lett., **12**, 3552-3559 (2021).

[60] J. P. Perdew, K. Burke, M. Ernzerhof, Phys. Rev. Lett., **77**, 3865-3868 (1996).

[61] J. Heyd, G. E. Scuseria, J. Chem. Phys., **121**, 1187-1192 (2004).

[62] J. Heyd, G. E. Scuseria, M. Ernzerhof, J. Chem. Phys., **118**, 8207-8215 (2003).

[63] G. Kresse, J. Furthmüller, Comput Mater Sci., **6**, 15-50 (1996).

[64] G. Kresse, J. Furthmüller, Phys. Rev. B, **54**, 11169 (1996).

[65] Yan, Z. Q. Huang, Y. Zhang, C. R Chang, Phys. Chem. Chem. Phys., **19**, 2364-2371 (2017).

[66] T. N. Pham, M. Sugiyama, F. Muttaqien, S. E. M. Putra, K. Inagaki, D. N. Son, Y. Hamamoto, I. Hamada, Y. Morikawa, J. Phys. Chem. C, **122**, 11814-11824 (2018).

[67] Ramaswamy, S. Mukerjee, J. Phys. Chem. C, **115**, 18015-18026 (2011).

[68] C. H. Choi, H. K. Lim, M. W. Chung, J. C. Park, H. Shin, H. Kim, S. I. Woo, J. Am. Chem. Soc., **136**, 9070-9077 (2014).

[69] Y. Wang, Y. J. Tang, K. Zhou, J. Am. Chem. Soc., 141, 14115-14119 (2019).

[70] S. Pezzotti, A. Serva, F. Sebastiani, F. S. Brigiano, D. R. Galimberti, L. Potier, S. Alfarano, G. Schwaab, M. Havenith, M. P. Gaigeot, J. Phys. Chem. Lett., **12**, 3827-3836 (2021).

[71] K. Soper, F. Bruni, M. A. Ricci, J. Chem. Phys., **106**, 247-254 (1997).

[72] H. Narten, H. A. Levy, J. Chem. Phys., **55**, 2263-1971 (1971).

[73] Groß, F. Gossenberger, X. Lin, M. Naderian, S. Sakong, T. Roman, J. Electrochem. Soc., **161**, E3015 (2014).

[74] Luzar, D. Chandler, Nature, **379**, 55-57 (1996).

Chapter 6

Conclusion and Outlook

6.1 Conclusion

In this dissertation, I have studied the CO_2RR, N_2RR, and ORR on three CN_x-based surfaces by DFT. The aim of this dissertation is to understand the following objectives:

1. The electronic structure of new-type CN_X, namely C_3N_5, CO_2RR catalytic mechanism pathway and activity on C_3N_5.

2. The electronic structure of B-doped g-C_9N_{10}, the N_2RR catalytic activity, mechanism pathways and selectivity of B-doped g-C_9N_{10}.

3. The electronic structure of N-doped GDY with G support, ORR catalytic mechanism pathway, and activity with solvation effect on N-doped GDY with G support.

First objective. I performed DFT calculations to systematically study the catalytic mechanism of the CO_2RR on C_3N_5. I obtained several important results:

1. The electronic structure analysis showed that due to the introduction of N=N bonds, C_3N_5 possesses a more suitable bandgap (2.0 eV) compared to g-C_3N_4 and extends the π-network, resulting in more efficient electron transfer and effective separation of photogenerated e^-/h^+ pairs.

2. Thermodynamic calculations suggest that C_3N_5 holds great promise as a CO_2RR photocatalyst with excellent photocatalytic activity, capable of reducing CO_2 to CH_4 and CH_3CH_2OH with limiting potentials of −0.54 V and −0.61 V, respectively, driven by solar energy.

Second objective. I investigated the N_2RR catalytic mechanism on three different doping B sites on g-C_9N_{10}. I obtained several important results:

1. B substituted N (B_{N1}) on g-C_9N_{10} may be synthesized in N-poor condition, while B substituted C (B_{C1}) may be synthesized in N-rich condition.

2. The N_2RR optimal mechanism pathway on B_{N1}-doped g-C_9N_{10} is Mixed I, namely N_2* → NNH* → NH_2N* → NH_2NH* → NH_2NH_2* → NH_2* → NH_3*.

3. B_{N1}-doped g-C_9N_{10} possesses efficient N_2RR catalytic activity and selectivity, while H blocks the active site in the case of B_A-doped g-C_9N_{10}, resulting in lower N_2RR selectivity.

4. The electronic structure analysis indicates that in the B_{N1} case, the fully unoccupied $2p_y$ orbital effectively hinders H adsorption, whereas in the B_A case, the singly occupied $2p_y$ orbital leads to stronger binding with H, resulting in H poisoning on B_A sites.

Third objective. DFT calculations and AIMD simulations to investigate the ORR mechanism on sp-N1GDY/G and Pyri-NGDY/G. I got the following key points:

1. Under both vacuum and water conditions, ORR firstly proceeds on sp-N1GDY/G via the dissociative mechanism because O_2 can be chemisorbed on a clean surface and easily dissociated rather than protonated to OOH*. However, OH* is strongly adsorbed on the sp-N1GDY/G surface, resulting in the weakening of the second O_2 adsorption, and ORR takes place via the ET-OHP associative mechanism. Pyri-NGDY/G also prefers the ET-OHP associative mechanism.

2. From AIMD simulation, the H bond networks at the contact region of water and NGDY are mainly composed of six-membered rings H bond networks. H bond with water stabilizes each ORR intermediate and the free energy diagram with solvation effect agrees well with experimental data. Moreover, we found that using the ice-like bilayer model to construct the H bond networks can also give a reasonable estimation of ΔSol. Therefore, the ΔSol of these

surfaces is independent of the water model, which arises from similar H bonds between adsorbates and water in the ice-like bilayer and AIMD H bond networks.

3. The sp-N1GDY/G with OH* pre-adsorbed surface has the highest ORR electrocatalytic activity and the neighboring C site of –COH–N moiety is the active site for ORR. Incorporation of solvation effect is of importance because η with solvation effect (0.46 V) is much closer to the experimental one (0.36 V).

6.2 Outlook

I should mention that the current study has its limitations. Therefore, there is a need for future research to enhance the results and uncover new insights into related issues.

Design the new-type CN_x as catalysts. I plan to design new CN_x materials using ML (such as GOFFEE by Bjørk Hammer). I want to predict the catalytic activity for CO_2RR, N_2RR, and ORR. This project should collaborate with the experiment groups.

Increase the computational efficiency and accuracy to perform AIMD simulation in solid/water interface. I plan to use machine learning (ML) technology to decrease the AIMD computation time and increase the model accuracy.

Double metal-free atoms doped on GDY for ORR. In the previous study, I have already investigated the ORR electrocatalytic activity on single N-doped GDY and the overpotential is 0.46 V. To increase the ORR electrocatalytic activity, I plan to investigate the ORR mechanism on double atoms doped GDY, such as sulfur (S)/N codoped GDY in the future.

Appendix A

Supporting Information in Chapter 3

Table A.1: Calculated free energy of the reaction path followed by CO_2 reduction to C1 products on g-C_3N_4 and C_3N_5.

		C_3N_5 ΔG (eV)	g-C_3N_4 ΔG (eV)
$1e^-$	$CO_2 + e^- + H^+ + * \rightarrow COOH*$	0.54	1.41
	$CO_2 + e^- + H^+ + * \rightarrow HCOO*$	2.42	—
$2e^-$	$COOH* + e^- + H^+ \rightarrow CO* + H_2O$	−0.48	−0.81
$3e^-$	$CO* + e^- + H^+ \rightarrow HCO*$	0.79	0.49
	$CO* + e^- + H^+ \rightarrow COH*$	−0.17	—
$4e^-$	$HCO* + e^- + H^+ \rightarrow HCHO + *$	—	−0.48
	$COH* + e^- + H^+ \rightarrow CHOH*$	−0.10	—
	$COH* + e^- + H^+ \rightarrow C* + H_2O$	1.55	—
$5e^-$	$HCHO + * + e^- + H^+ \rightarrow CH_3O*$	—	1.43
	$CHOH* + e^- + H^+ \rightarrow CH_2OH*$	0.41	—
	$CHOH* + e^- + H^+ \rightarrow CH*+ H_2O$	−0.30	—
$6e^-$	$CH *+ e^- + H^+ \rightarrow CH_2*$	−0.30	—
	$CH_3O* + e^- + H^+ \rightarrow CH_3OH + *$	—	−2.07
$7e^-$	$CH_2* + e^- + H^+ \rightarrow CH_3*$	0.12	—
$8e^-$	$CH_3* + e^- + H^+ \rightarrow CH_4$	−0.14	—

Table A.2: The calculated adsorption energies (E_{ads}) of various CO_2RR species with C_3N_5 and g-C_3N_4 using DMol^3 code with solvation model.

	CO_2	COOH	CO	CH_3OH	CH_4	CH_3CH_2OH
	E_{ads} (eV)	E_{ads} (eV)	E_{ads} (eV)	E_{ads} (eV)	E_{ads} (eV)	E_{ads} (eV)
C_3N_5	−0.09	−2.48	−1.80	—	−0.06	−0.16
g-C_3N_4	−0.09	−1.61	−0.23	−0.41	—	—

Table A.3: Calculated free energy of the reaction path followed by CO_2 reduction to C2 products on C_3N_5.

		C_3N_5
		ΔG (eV)
$1e^-$	$CO_2 + e^- + H^+ + * \rightarrow COOH*$	0.54
$2e^-$	$COOH* + e^- + H^+ \rightarrow CO* + H_2O$	−0.48
$3e^-$	$CO* + e^- + H^+ \rightarrow COH*$	−0.17
	$CO* + e^- + H^+ \rightarrow HCO*$	0.79
C–C coupling	$CO* + CO \rightarrow COCO*$	−0.02
$4e^-$	$COH* + e^- + H^+ \rightarrow CHOH*$	−0.10
	$COCO* + e^- + H^+ \rightarrow COCOH*$	−0.63
C–C coupling	$COH* + CO \rightarrow COHCO*$	−0.48
$5e^-$	$CHOH* + e^- + H^+ \rightarrow CH* + H_2O$	−0.30
	$COHCO* + e^- + H^+ \rightarrow CCO* + H_2O$	1.51
	$COHCO* + e^- + H^+ \rightarrow HOCCOH*$	0.26
C–C coupling	$CH* + CO \rightarrow CHCO*$	0.11
$6e^-$	$CH* + e^- + H^+ \rightarrow CH_2*$	−0.30

	$HOCCOH^* + e^- + H^+ \rightarrow CCOH^* + H_2O$	1.60
C–C coupling	$CH_2^* + CO \rightarrow CH_2CO^*$	−0.64
$7e^-$	$CH_2CO^* + e^- + H^+ \rightarrow CH_2COH^*$	0.33
	$CH_2CO^* + e^- + H^+ \rightarrow CH_2CHO^*$	1.03
	$CH_2CO^* + e^- + H^+ \rightarrow CH_3CO^*$	0.58
$8e^-$	$CH_2COH^* + e^- + H^+ \rightarrow CH_3COH^*$	−0.59
	$CH_2COH^* + e^- + H^+ \rightarrow CH_2CHOH^*$	−0.66
$9e^-$	$CH_3COH^* + e^- + H^+ \rightarrow CH_3CHOH^*$	0.61
	$CH_2CHOH^* + e^- + H^+ \rightarrow CH_3CHOH^*$	0.68
$10e^-$	$CH_3CHOH^* + e^- + H^+ \rightarrow CH_3CH_2OH$	−0.11

Appendix B

Supporting Information in Chapter 4

In our work, the phonon contribution of solids to free energy is negligible. To verify this point, we estimated the $\Delta E_{ZPE} - T\Delta S$ term of $N_2 + * \rightarrow N_2*$ process on B_A-doped g-C_9N_{10} with and without phonon contribution using harmonic approximation [1], the equation is as shown in following [2]:

$$E_{ZPE} = \frac{1}{2}\sum_i h\upsilon_i \quad \text{(B-1)}$$

$$-TS = k_B T \sum_i \ln\left(1 - e^{-\frac{h\upsilon_i}{K_B T}}\right) - \sum_i h\upsilon_i \left(\frac{1}{e^{\frac{h\upsilon_i}{k_B T}} - 1}\right) \quad \text{(B-2)}$$

where h, υ_i, and k_B are Planck constant, vibrational frequencies, and Boltzmann constant, respectively. Vibrational analyses were performed using the finite difference method at the Γ point only.

As shown in Table B.1, we found that $\Delta E_{ZPE} - T\Delta S$ values with and without phonon contribution differ by only 40 meV. Therefore, only the calculation of E_{ZPE} and S of reaction intermediates are needed as the contribution of substrate can be offset.

Table B.1: Calculated E_{ZPE} and TS values (in eV) of N_2 adsorbed B_A-doped g-C_9N_{10}, B_A-doped g-C_9N_{10}, and N_2 gas with and without phonon contribution. Calculated $\Delta E_{ZPE} - T\Delta S$ *of* $N_2 + * \rightarrow N_2*$ process on B_A doped g-C_9N_{10} with and without phonon contribution.

	with phonon contribution			**without phonon contribution**		
system	N_2 adsorbed B_A-doped g-C_9N_{10}	B_A-doped g-C_9N_{10}	N_2 gas	N_2 adsorbed B_A-doped g-C_9N_{10}	B_A-doped g-C_9N_{10}	N_2 gas
E_{ZPE}	3.02	2.87	0.148	0.22	0	0.148

TS	0.64	0.74	0.593	0	0	0.593
process	$N_2 + * \rightarrow N_2*$			$N_2 + * \rightarrow N_2*$		
ΔE_{ZPE}	0.002			0.072		
$T\Delta S$	−0.703			−0.593		
$\Delta E_{ZPE} - T\Delta S$	0.705			0.665		

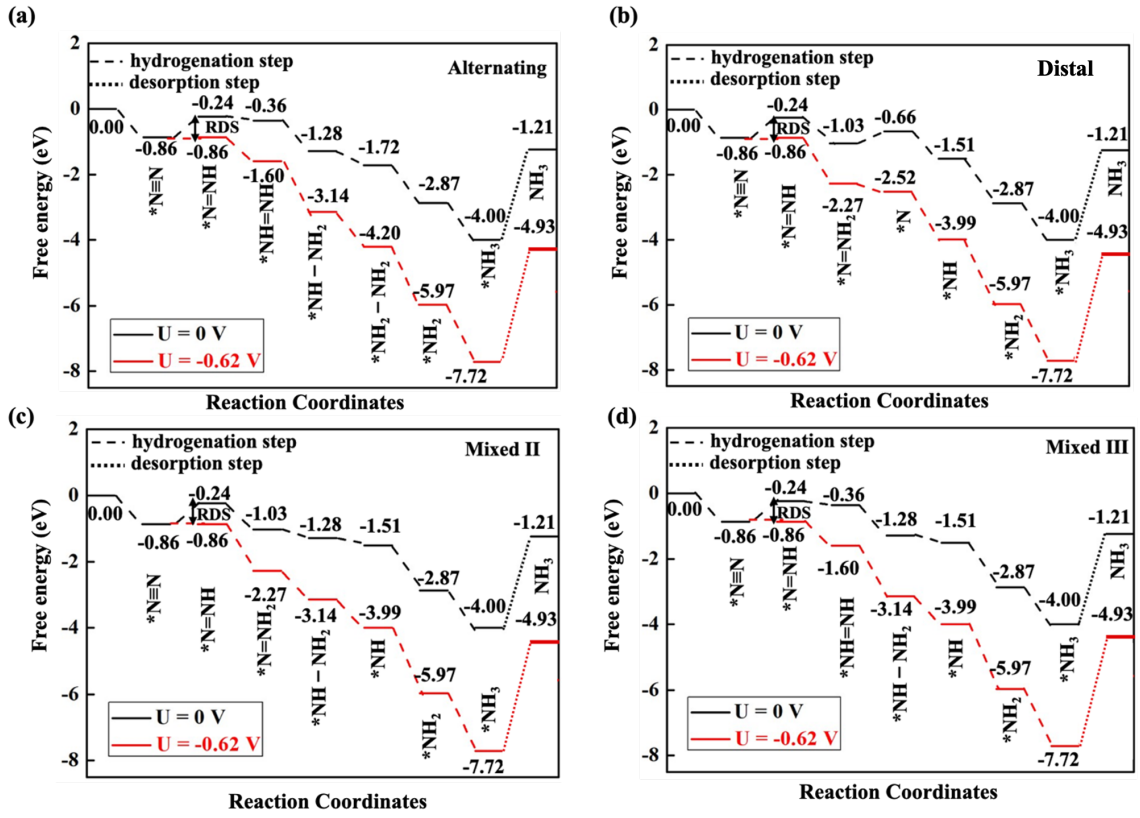

Figure B.1: Free energy diagrams for N_2 reduction on B_{N1}-doped g-C_9N_{10} through (a) alternating, (b) distal, (c) Mixed II, and (d) Mixed III mechanisms at different applied potentials.

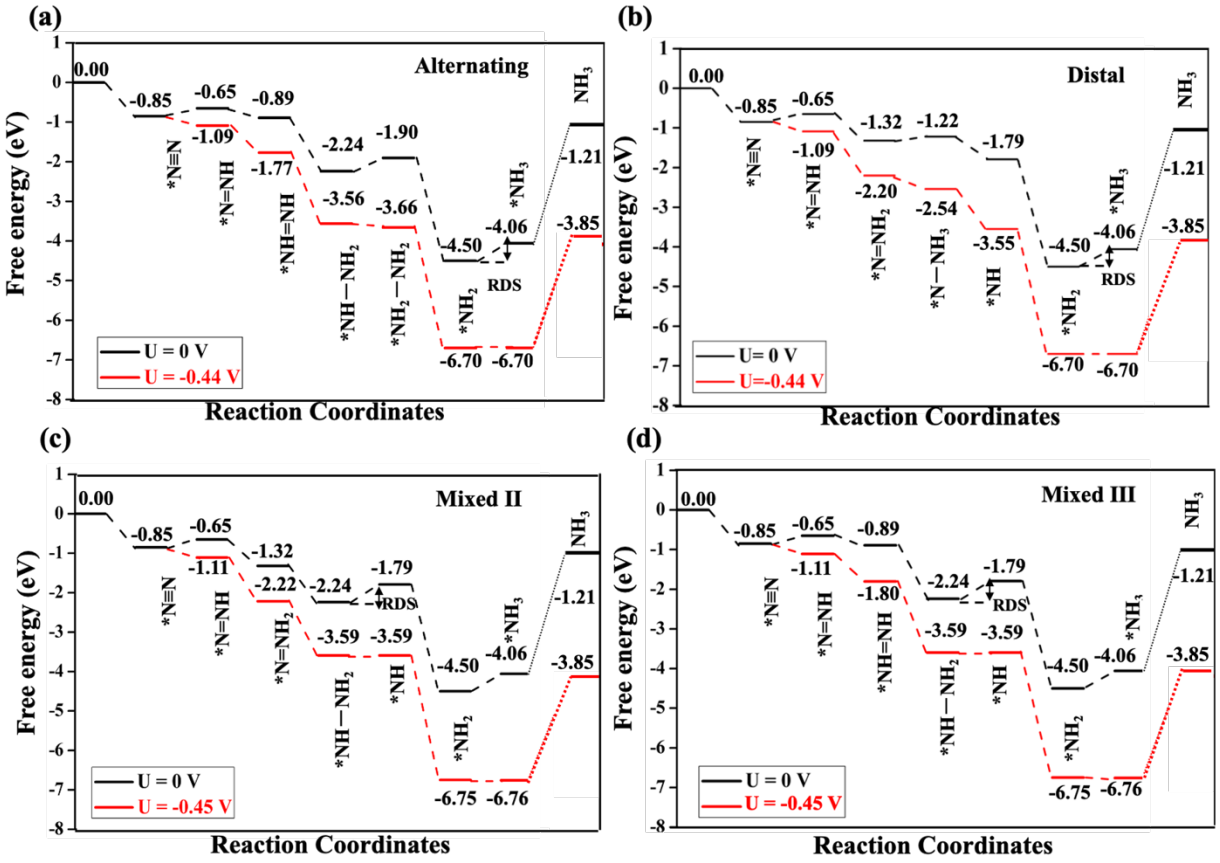

Figure B.2: Free energy diagrams for N_2 reduction on B_A-doped g-C_9N_{10} through (a) alternating, (b) distal, (c) Mixed II, and (d) Mixed III mechanisms at different applied potentials.

Table B.2: Calculated free energy of the reaction path followed by N_2RR on B_{N1}-doped g-C_9N_{10}.

process		B_{N1} case
		ΔG (eV)
adsorption	$N_2 + * \rightarrow NN*$	−0.90
1e⁻	$NN* + e^- + H^+ \rightarrow NNH*$	0.62
2e⁻	$NNH* + e^- + H^+ \rightarrow NH_2N*$	−0.75
	$NNH* + e^- + H^{+}{}^{+} \rightarrow NHNH*$	−0.08
3e⁻	$NH_2N* + e^- + H^+ \rightarrow NH_2NH*$	−0.25

	$NH_2N^* + e^- + H^+ \rightarrow N^* + NH_3$	0.37
	$NHNH^* + e^- + H^+ \rightarrow NH_2NH^*$	−1.44
4e⁻	$NH_2NH^* + e^- + H^+ \rightarrow NH_2NH_2^*$	−0.44
	$N^* + e^- + H^+ \rightarrow NH^*$	−0.85
	$NH_2NH^* + e^- + H^+ \rightarrow NH^* + NH_3$	−0.13
5e⁻	$NH_2NH_2^* + e^- + H^+ \rightarrow NH_2^* + NH_3$	−1.15
	$NH^* + e^- + H^+ \rightarrow NH_2^*$	−1.36
6e⁻	$NH_2^* + e^- + H^+ \rightarrow NH_3^*$	−1.13
desorption	$NH_3^* \rightarrow NH_3 + *$	2.79

Table B.3: Calculated free energy of the reaction path followed by N_2RR on B_A-doped g-C_9N_{10}.

process		B_A case
		ΔG (eV)
adsorption	$N_2 + * \rightarrow NN^*$	−0.85
1e⁻	$NN^* + e^- + H^+ \rightarrow NNH^*$	0.20
2e⁻	$NNH^* + e^- + H^+ \rightarrow NH_2N^*$	−0.67
	$NNH^* + e^- + H^+ \rightarrow NHNH^*$	−0.24
3e⁻	$NH_2N^* + e^- + H^+ \rightarrow NH_2NH^*$	−0.92
	$NH_2N^* + e^- + H^{+\,+} \rightarrow NNH_3^*$	0.1
	$NHNH^* + e^- + H^+ \rightarrow NH_2NH^*$	−1.35
4e⁻	$NH_2NH^* + e^- + H^+ \rightarrow NH_2NH_2^*$	0.34
	$NNH_3 + e^- + H^+ \rightarrow NH^* + NH_3$	−0.57
	$NH_2NH^* + e^- + H^+ \rightarrow NH^* + NH_3$	0.45
5e⁻	$NH_2NH_2^* + e^- + H^+ \rightarrow NH_2^* + NH_3$	−2.60

	$NH^* + e^- + H^+ \rightarrow NH_2^*$	−2.71
$6e^-$	$NH_2^* + e^- + H^+ \rightarrow NH_3^*$	0.44
desorption	$NH_3^* \rightarrow NH_3 + *$	2.85

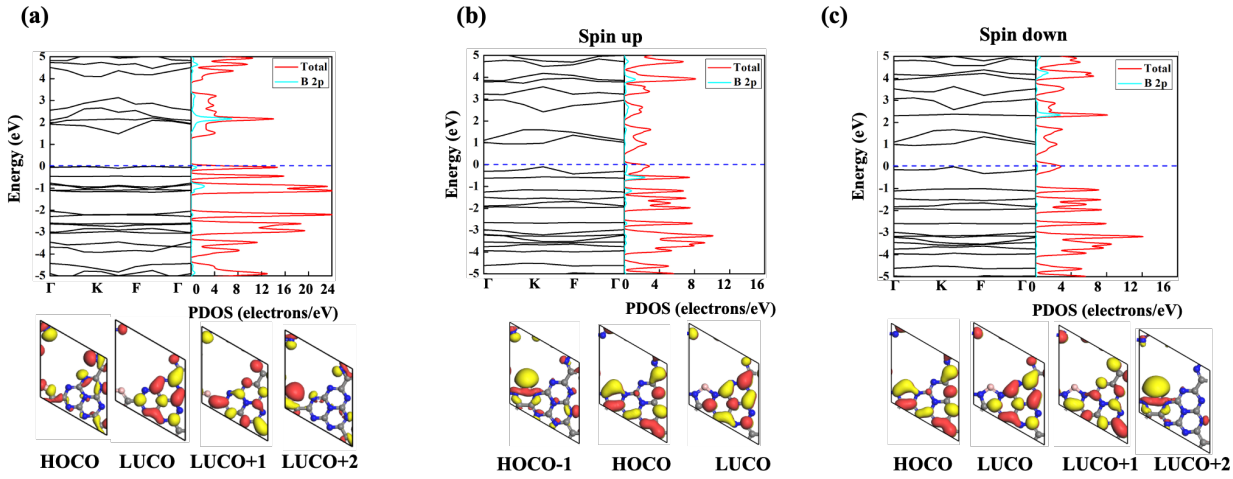

Figure B.3: The band gap, PDOS HOMO, and LUMO distributions of B_{N1}-doped g-C_9N_{10} (a), B_A-doped g-C_9N_{10} in the spin up channel (b) and spin down channel (c) by using GGA/PBE functional.

Reference

[1] D. R. Lide, CRC handbook of physics and chemistry, CRC Press, Boca Raton, USA, **76**,1995-1996 (2001).

[2] C. Ling, X. Niu, Q. Li, A. Du, J. Wang, J. Am. Chem. Soc., **140**, 14161-14168 (2018).

Appendix C

Supporting Information in Chapter 5

Table C.1: Band gap (E_g) of corrugated graphene (G), GDY, N (sp-N1, sp-N2, Pyri-N)-doped GDY, N (sp-N1, sp-N2, Pyri-N)-doped GDY/G were calculated by the PBE functional and HSE06 functional.

	E_g (eV)		
	PBE	HSE06	Ref.
corrugated G	zero-gap semiconductor	zero-gap semiconductor	—
GDY	0.5	0.9	0.89 (HES06) [1]/1.10 (GW) [2]
sp-N1GDY	metallic	metallic	Metallic [3]
sp-N2GDY	metallic	metallic	—
Pyri-NGDY	0.6	0.97	—
sp-N1GDY/G	metallic	metallic	—
sp-N2GDY/G	metallic	metallic	—
Pyri-NGDY/G	metallic	metallic	—

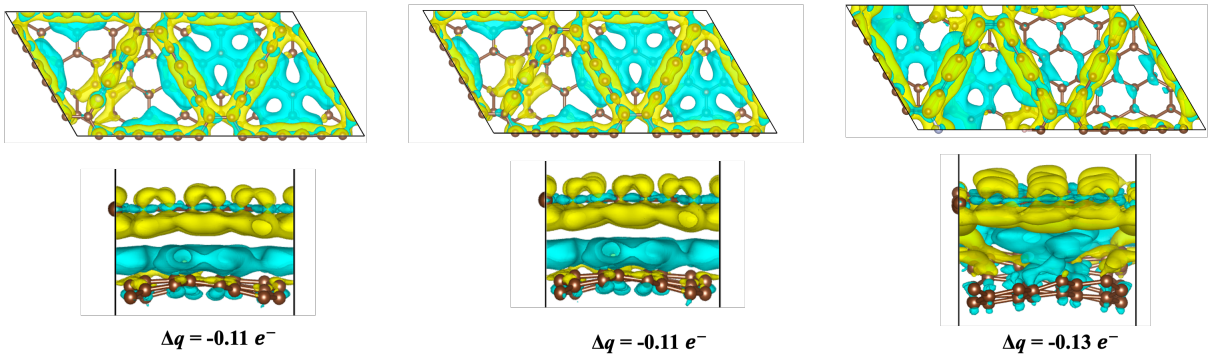

Figure C.1: The top view and side view of CDD on sp-N1GDY/G (a), sp-N2GDY/G (b), and Pyri-NGDY/G (c). The yellow and blue isosurfaces represent charge accumulation and depletion, respectively. The isosurface value is around 0.00018 e/Å^3. The Bader charge of three N-doped GDY/G is listed in which $\Delta q = Z - q$, where Z is the total valence electrons of atoms (1, 4, and 5 for H, C, and N, respectively) and q is the total Bader electrons.

Table C.2: The calculated work function of planar graphene, corrugated graphene, GDY, sp-N1GDY, sp-N2GDY, Pyri-NGDY, sp-N1GDY/G, sp-N2GDY/G, and Pyri-NGDY/G.

	work function	Ref.
planar graphene	4.20 eV	4.25 eV [4], 4.38 eV [5], 4.50 eV (Exp.) [6]
corrugated graphene	4.10 eV	—
GDY	5.10 eV	5.13 eV [7], 6.0 eV (Exp.) [7]
sp-N1GDY	4.53 eV	—
sp-N2GDY	4.53 eV	—
Pyri-NGDY	4.93 eV	—
sp-N1GDY/G	4.40 eV	—
sp-N2GDY/G	4.40 eV	—
Pyri-NGDY/G	4.62 eV	—

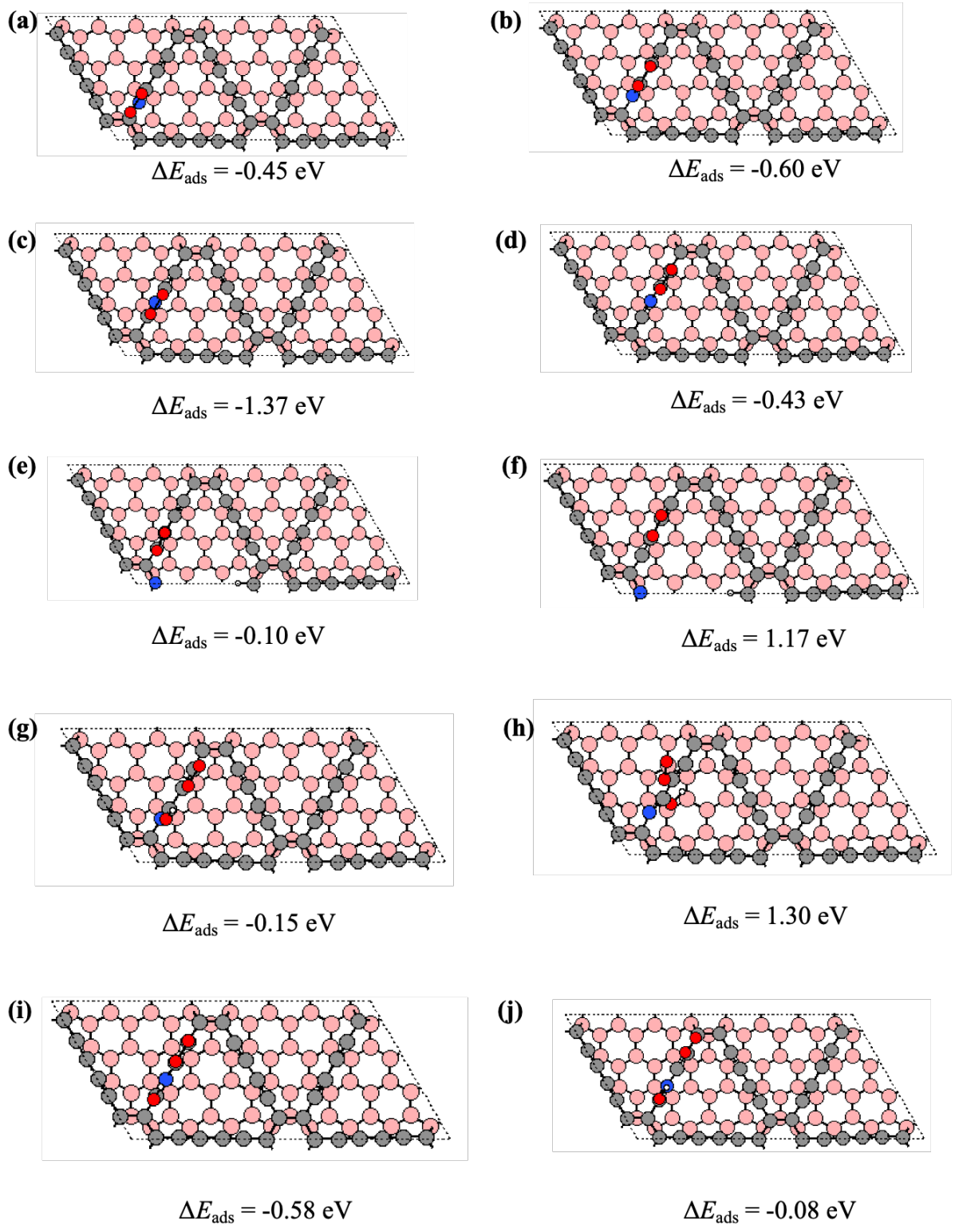

Figure C.2: The possible active sites of O_2 absorption on sp-N1GDY/G (a, b), sp-N2GDY/G (c, d), Pyri-NGDY/G (e, f), sp-N1GDY(OH)/G (g, h), and sp-N2GDY(OH)/G (i, j). Red, white, gray, pink, and blue balls are O atoms, H atoms, C atoms in N-doped GDY, C atoms in G, and N atoms, respectively.

Table C.3: Adsorption energy (ΔE_{ads}/eV) of each ORR intermediate on each surface and distance (d/Å) between O_2 and surface in vacuum.

	ΔE_{ads} (O_2)	d	ΔE_{ads} (2O)	ΔE_{ads} (O+OH)	ΔE_{ads} (OOH)	ΔE_{ads} (O)	ΔE_{ads} (OH)	ΔE_{ads} (H_2O)
sp-N1GDY/G	−0.60	1.425	−11.71	−9.56	—	−6.05	−4.08	−0.11
sp-N1GDY(OH)/G	−0.15	3.074	—	—	−1.23	−4.97	−2.86	−0.09
sp-N2GDY/G	−1.37	1.368	−12.81	−10.17	—	−7.08	−4.36	−0.18
sp-N2GDY(OH)/G	−0.58	1.426	−13.47	—	—	—	—	—
Pyri-NGDY/G	−0.10	3.100	—	—	−0.93	−4.98	−2.52	−0.06

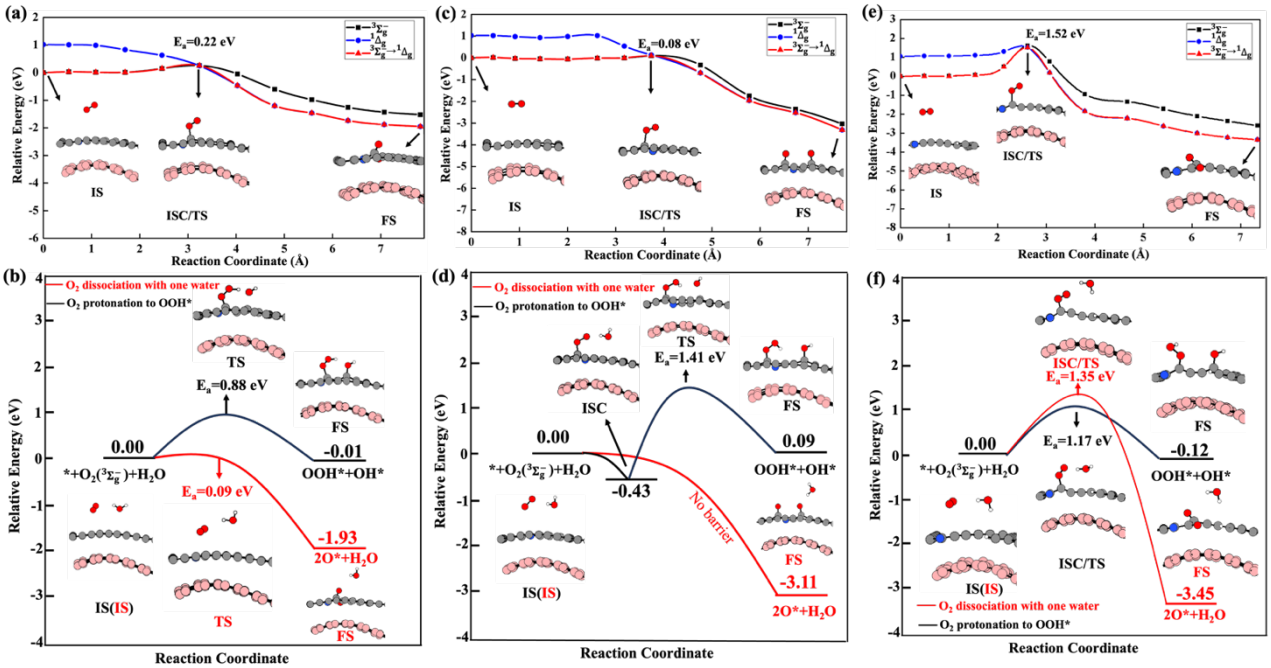

Figure C.3: Reaction path of (a) O_2 dissociation, (b) O_2 protonation to OOH*, and O_2 dissociation with one H_2O on sp-N1GDY/G. Reaction path of (c) O_2 dissociation, (d) O_2 protonation to OOH*, and O_2 dissociation with one H_2O on sp-N2GDY/G. Reaction path of (e) O_2 dissociation, (f) O_2 protonation to OOH*, and O_2 dissociation with one H_2O on Pyri-NGDY/G. Structures corresponding to the initial state (IS), intersystem crossing state/transition state (ISC/TS), and final state (FS) are shown. Red, white, gray, pink, and blue balls are O atoms, H atoms, C atoms in N-doped GDY, C atoms in G, and N atoms, respectively.

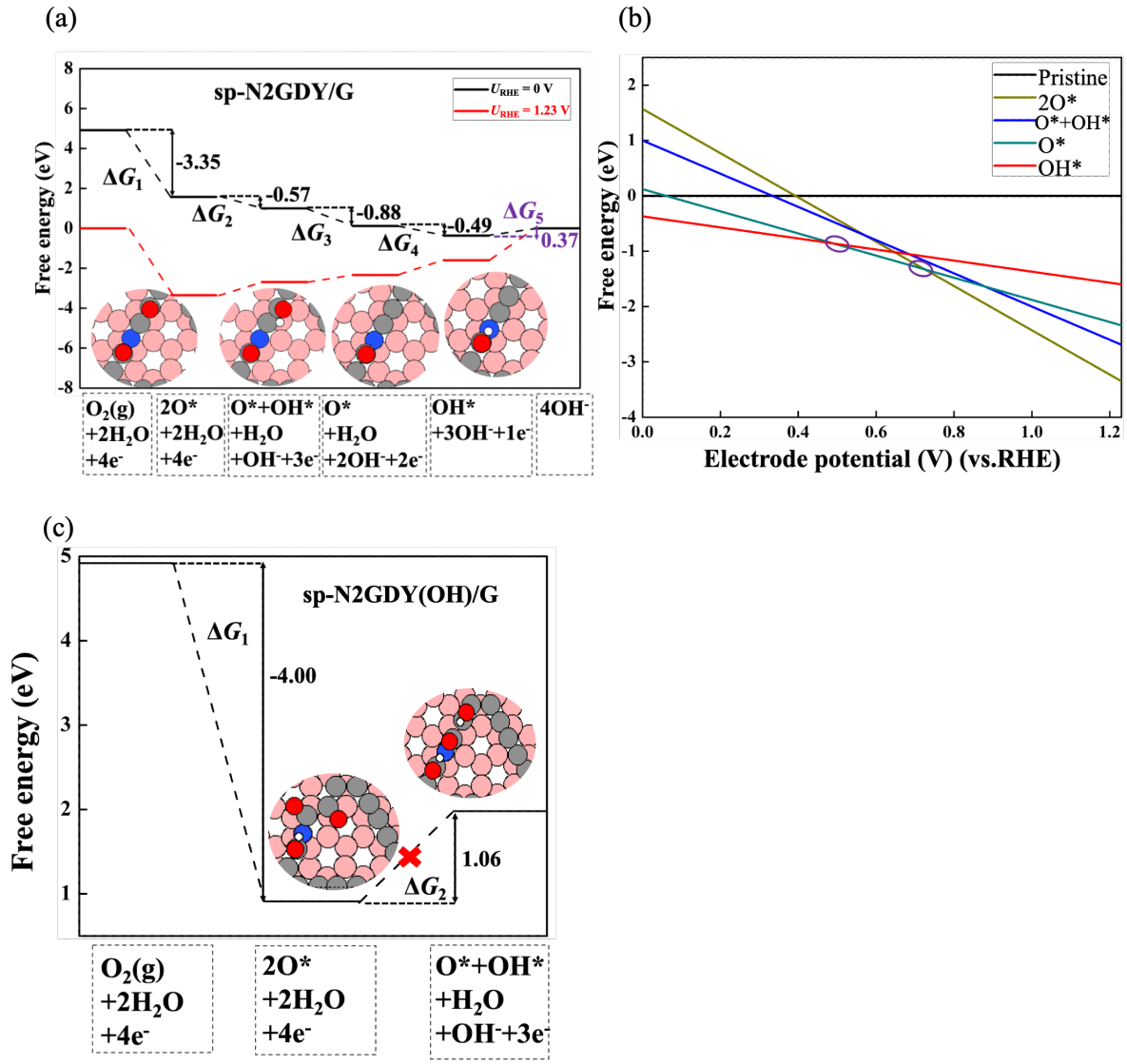

Figure C.4: Free energy diagram (a) and structures of each ORR intermediate on sp-N2GDY/G, (b) free energy of each ORR intermediate versus electrode potential (vs. RHE) on sp-N2GDY/G; Free energy diagram and structures (c) of ORR intermediates on sp-N2GDY(OH)/G. Red, white, gray, pink, and blue balls are O atoms, H atoms, C atoms in N-doped GDY, C atoms in G, and N atoms, respectively.

Table C.4: The calculated E_{ZPE}, TS, and $\int_0^T C_P dT$ of gas-phase molecules and each ORR intermediate.

	E_{ZPE}/eV	TS/eV	$\int_0^T C_P dT$/eV
2O*	0.18	0.11	0.061
O*+OH*	0.49	0.11	0.062
OOH*	0.45	0.18	0.086

O*	0.10	0.05	0.026
OH*	0.40	0.06	0.037
H_2O (g)	0.56	0.58	0.106
H_2 (g)	0.27	0.43	0.091

Table C.5: Reaction Gibbs free energy of each ORR intermediate on sp-N1GDY/G, sp-N1GDY/G(OH), and Pyri-NDGY with and without water, reaction Gibbs free energy of ORR on sp-N2GDY/G and sp-N2GDY/G(OH) without water.

	ΔG_1	ΔG_2	ΔG_3	ΔG_4	ΔG_5	ΔG_6	ΔG_7
sp-N1GDY/G	−2.24	−1.07	−0.88	−0.86	0.13	—	—
sp-N1GDY/G with water	−2.49	−1.07	−0.89	−0.85	0.38	—	—
sp-N1GDY/G(OH)	—	—	—	−1.08	−1.15	−0.51	−2.18
sp-N1GDY(OH)/G with water	—	—	—	−1.07	−0.90	−0.77	−2.18
sp-N2GDY/G	−3.35	−0.57	−0.88	−0.49	0.37	—	—
sp-N2GDY/G(OH)	−4.00	1.06 (×)	—	—	—	—	—
Pyri-NDGY	—	—	—	−0.74	−1.47	−0.22	−2.49
Pyri-NDGY with water	—	—	—	−0.52	−1.29	−0.48	−2.63

Table C.6: Adsorption Gibbs free energy of each ORR intermediate on sp-N1GDY, sp-N2GDY, sp-N2GDY/G, sp-N2GDY(OH)/G, and Pyri-NGDY without water; sp-N1GDY/G, sp-N1GDY(OH)/G, Pyri-NGDY/G, and Pyri-NGDY(OH)/G with and without water.

	ΔG_{ads} (2O*)	ΔG_{ads} (O*+OH*)	ΔG_{ads} (OOH*)	ΔG_{ads} (O*)	ΔG_{ads} (OH*)
sp-N1GDY	2.82	1.63	—	0.91	−0.10
sp-N1GDY/G	2.68	1.61	—	0.73	−0.13
sp-N1GDY/G with water	2.43	1.36	—	0.47	−0.38
sp-N1GDY(OH)	—	—	4.44	2.26	1.17
sp-N1GDY(OH)/G	—	—	4.41	2.23	1.15
sp-N1GDY(OH)/G with water	—	—	4.15	1.97	0.90
sp-N2GDY	1.71	1.13	—	0.48	−0.31
sp-N2GDY/G	1.57	1.00	—	0.12	−0.37
sp-N2GDY/G(OH)	0.92	1.98 (×)	—	—	—
Pyri-NDGY	—	—	4.86	2.41	1.59
Pyri-NDGY/G	—	—	4.70	2.21	1.47
Pyri-NDGY/G with water	—	—	4.44	1.81	1.29

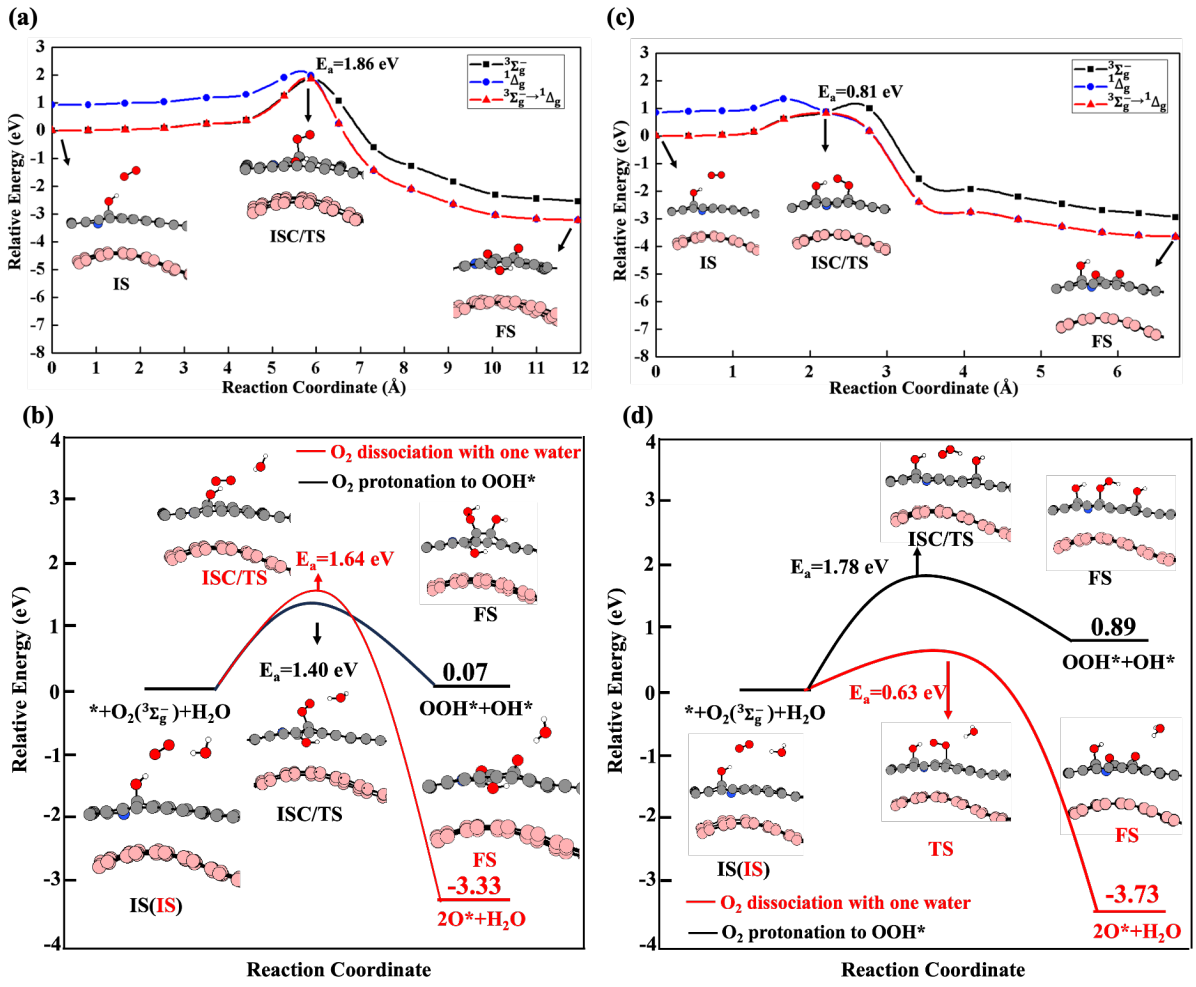

Figure C.5: Reaction path of (a) O_2 dissociation, (b) O_2 protonation to OOH*, and O_2 dissociation with one H_2O on sp-N1GDY(OH)/G. Reaction path of (c) O_2 dissociation, (d) O_2 protonation to OOH*, and O_2 dissociation with one H_2O on sp-N2GDY(OH)/G. Structures corresponding to the initial state (IS), intersystem crossing state/transition state (ISC/TS), and final state (FS) are shown. Red, white, gray, pink, and blue are O atoms, H atoms, C atoms in N-doped GDY, C atoms in G, and N atoms, respectively.

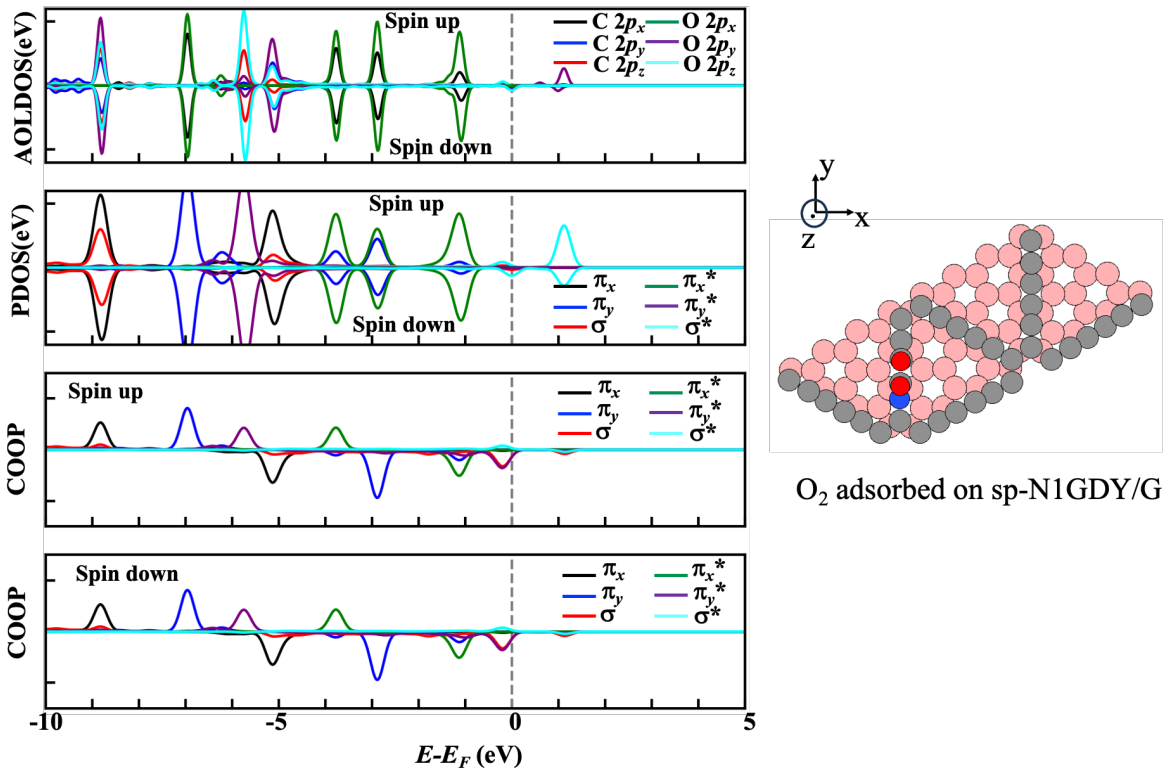

Figure C.6: The atomic orbital local density of states (AOLDOS), projected density of states into crystal orbitals (PDOS), and crystal orbital overlap population (COOP) of O_2 adsorbed on sp-N1GDY/G. Red, gray, pink, and blue are O atoms, C atoms in N-doped GDY, C atoms in G, and N atoms, respectively.

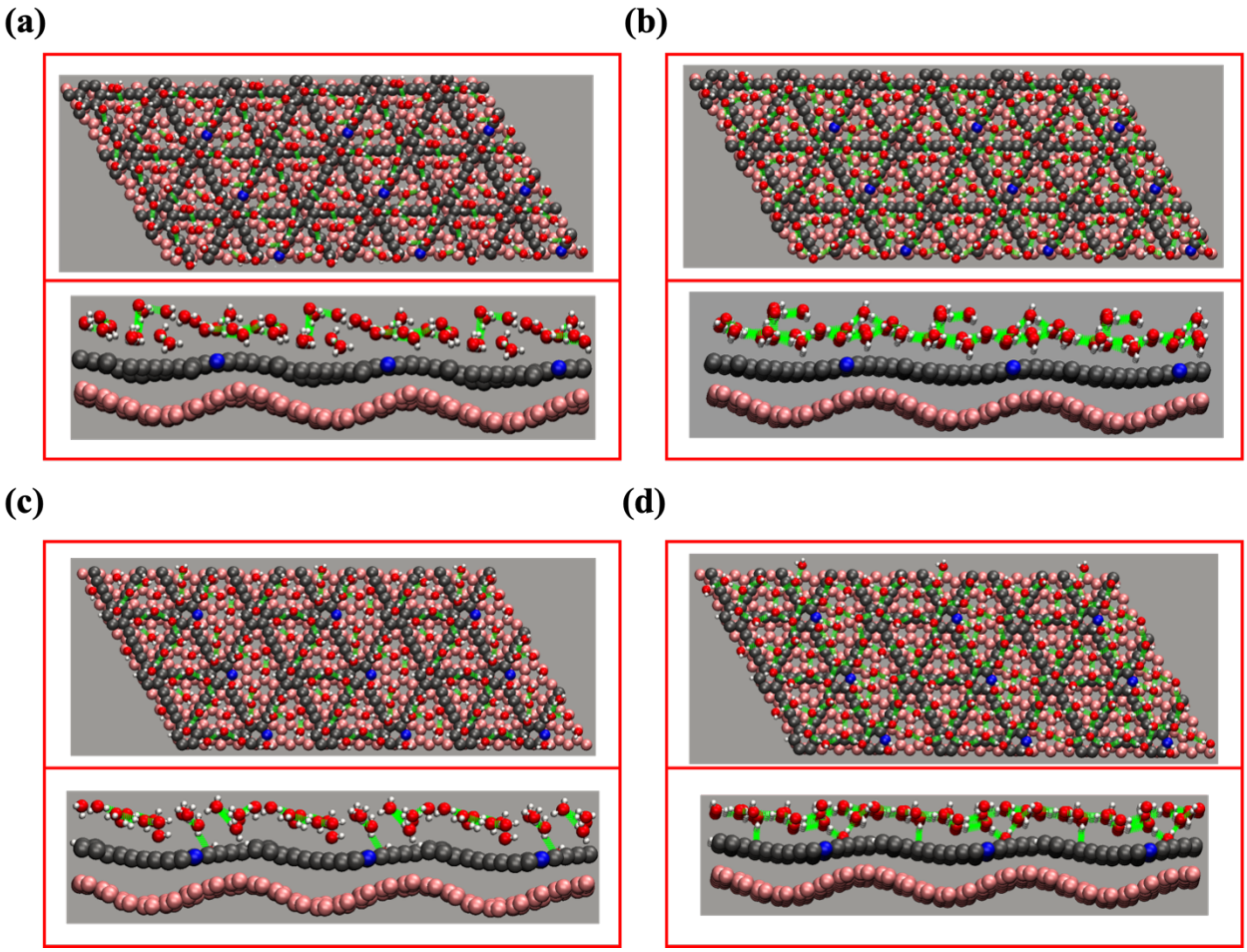

Figure C.7: Top view (left) and side view (right) of H bond networks on the sp-N1GDY/G in 400 K (a) and 0 K (b) and Pri-NGDY/G in 400 K (c) and 0 K (d) with 3×3 supercell. Red, white, gray, pink, and blue balls are O atoms, H atoms, C atoms in N-doped GDY, C atoms in G, and N atoms, respectively. The green dashed lines represent the H bond networks.

Table C.7: The $\Delta E_{\mathrm{nH_2O*}}$, and ΔSol of each ORR intermediate on sp-N1GDY/G with ice-like bilayer layer and five snapshots from AIMD, n is water number.

	$\Delta E_{\mathrm{nH_2O*}}$ (eV/H_2O)	n	ΔSol (2O*)	ΔSol (O*+OH*)	ΔSol (OOH*)	ΔSol (O*)	ΔSol (OH*)
Ice-like bilayer	−0.45(H-up)/ −0.46(H-down)	16	−0.31	−0.26	−0.32	−0.28	−0.27
AIMD-1	−0.43	18	−0.28	−0.28	−0.20	−0.27	−0.22
AIMD-2	−0.42	17	−0.26	−0.27	−0.26	−0.26	−0.21
AIMD-3	−0.41	17	−0.28	−0.28	−0.29	−0.28	−0.29
AIMD-4	−0.41	17	−0.23	−0.23	−0.28	−0.23	−0.26
AIMD-5	−0.43	19	−0.20	−0.20	−0.27	−0.20	−0.21
Average with 5 AIMD snapshots	—	—	−0.25	−0.25	−0.26	−0.25	−0.24

Table C.8: The $\Delta E_{\mathrm{nH_2O*}}$ and ΔSol each ORR intermediate on Pyri-NGDY/G with ice-like bilayer layer and five snapshots from AIMD. n is the water number.

	$\Delta E_{\mathrm{nH_2O*}}$ (eV/H_2O)	n	ΔSol(OOH*)	ΔSol(O*)	ΔSol(OH*)
Ice-like bilayer	−0.45(H-up)/ −0.46(H-down)	16	−0.27	−0.45	−0.21
AIMD-1	−0.43	17	−0.20	−0.39	−0.21
AIMD-2	−0.44	17	−0.20	−0.40	−0.10
AIMD-3	−0.43	17	−0.23	−0.32	−0.13
AIMD-4	−0.43	17	−0.37	−0.37	−0.15
AIMD-5	−0.40	17	−0.31	−0.46	−0.33
Average with 5 AIMD snapshots	—	—	−0.26	−0.40	−0.18

Table C.9: The adsorption Gibbs free energy of each ORR intermediate on sp-N1GDY/G, sp-N1GDY(OH)/G, and Pyri-NGDY/G with and without water using PBE+D2 functional.

	ΔG_{ads} (2O*)	ΔG_{ads} (O*+OH*)	ΔG_{ads} (OOH*)	ΔG_{ads} (O*)	ΔG_{ads} (OH*)
sp-N1GDY/G	2.57	1.38	—	0.70	−0.16
sp-N1GDY/G with water	2.24	1.06	—	0.40	−0.44
sp-N1GDY(OH)/G	—	—	4.23	2.18	0.97
sp-N1GDY(OH)/G with water	—	—	3.86	1.88	0.69
Pyri-NDGY/G	—	—	4.58	2.20	1.35
Pyri-NDGY/G with water	—	—	4.30	1.67	1.09

Table C.10: The $\Delta E_{\mathrm{nH_2O*}}$ and the ΔSol of each ORR intermediate on sp-N1GDY/G and Pyri-NGDY/G with ice-like bilayer using PBE+D2 functional.

	$\Delta E_{\mathrm{nH_2O*}}$ (eV/H_2O)		ΔSol (2O*)	ΔSol (O*+OH*)	ΔSol (OOH*)	ΔSol (O*)	ΔSol (OH*)
	H-up	H-down					
sp-N1GDY/G	−0.56	−0.57	−0.33	−0.32	−0.37	−0.30	−0.28
Pyri-NGDY/G	−0.56	−0.57	—	—	−0.28	−0.53	−0.26

References:

[1] Q. Yue, S. Chang, J. Kang, S. Qin, J. Li, J. Phys. Chem. C, **117**, 14804-14811 (2013).

[2] G. F. Luo, X. M. Qian, H. B. Liu, R. Qin, J. Zhou, L. Z. Li, Z. X. Gao, E. G. Wang, W. N. Mei, J. Lu, Y. L. Li, S. Nagase, Phys. Rev. B: Condens. Matter Mater. Phys., **84**, 075439 (2011).

[3] N. N.T. Pham, Applied Surface Science Advances, **11**, 100301 (2022).

[4] W. Hu, T. Wang, R. Zhang, Jinlong Yang, J. Mater. Chem. C, **4**, 1776-1781 (2016).

[5] M. Legesse, F. E. Mellouhi, E. T. Bentria, M. E. Madjet,T. S. Fisher, S. Kais, F. H. Alharbi, Appl. Surf. Sci. **394**, 98-107 (2017).

[6] Y. J. Yu, Y. Zhao, S. Ryu, L. E. Brus, K. S. Kim and P. Kim, Nano Lett., **9**, 3430-3434 (2009).

[7] F. Xu, K. Meng, B. Zhu, H. Liu, J. Xu, J. Yu, Adv. Funct. Mater., **29**, 1904256 (2019).

Acknowledgments

I extend my gratitude to all people who have supported, helped, and encouraged me in my journey to earn my Ph.D. degree.

I would like to express my sincere gratitude to my supervisor, Prof. Yoshitada Morikawa, His rigorous approach to research and his diligent spirit of inquiry serves as a lifelong role model for me. Whenever I encountered difficulties in life or in my studies, Professor Morikawa always provided full support, making me feel the warmth of family.

I want to extend my thanks to Assoc. Prof. Ikutaro Hamada, Assist. Prof. Kouji Inagaki and Assist. Prof. Yuji Hamamoto for their valuable insights into my research. I also thank Prof. Kazuto Yamauchi and Prof. Kenta Arima for their willingness to be vice examiners in my doctoral dissertation. I especially thank Prof. Likai Yan from Northeast Normal University in China for her best advice and suggestions.

I am grateful to all secretaries and colleagues in Morikawa Laboratory for their help and encouragement during this academic journey.

I am also thankful for the support provided by the Japan Society for the Promotion of Science (JSPS) Research Fellowship for Young Scientists; by the JST SPRING program; and by Professional Development Consortium for Computational Materials Scientists-Innovative Professional Development Program (PCoMS-IPD).

Lastly, I want to thank, my parents, my husband, Wenjia Huang, my family members, my two cats, and my friends for their unwavering companionship and support. I love them so much!

October 2023

WANG YUELIN

Biography

List of Publications:

1. **Yuelin Wang,** Thanh Ngoc Pham, Yu Tian, Yoshitada Morikawa*, Likai Yan*, Density functional theory study on a nitrogen-rich carbon nitride material C_3N_5 as photocatalyst for CO_2 reduction to C1 and C2 products, *Journal of Colloid and Interface Science*, 2021, vol. 585, pp. 740-749.
2. **Yuelin Wang,** Thanh Ngoc Pham, Likai Yan*, Yoshitada Morikawa*, Activity and selectivity of N_2 fixation on B doped g-C_9N_{10}: A density functional theory study, *Journal of Materials Chemistry C*, 2022, vol. 10, pp. 11791-11800.
3. **Yuelin Wang,** Thanh Ngoc Pham, Harry H. Halim, Likai Yan, Yoshitada Morikawa*, DFT investigation on oxygen reduction reaction over nitrogen (N) doped graphdiyne as an electrocatalyst: the importance of pre-adsorbed OH* and solvation effect, *Materials Advances*, 2023, DOI: 10.1039/D3MA00502J.
4. Kenta Kuroishi, Muhammad Rifqi Al Fauzan, Thanh Ngoc Pham, **Yuelin Wang**, Yuji Hamamoto, Kouji Inagaki, Akitoshi Shiotari, Hiroshi Okuyama, Shinichiro Hatta, Tetsuya Aruga, Ikutaro Hamada, Yoshitada Morikawa, A flat-lying dimer as a key intermediate in NO reduction on Cu (100), *Physical Chemistry Chemical Physics*, 2021, vol. 31, pp. 16880-16887.

List of Presentations

1. **Yuelin Wang,** Thanh Ngoc Pham, Yoshitada Morikawa*, Likai Yan*, Density functional theory study on a nitrogen-rich carbon nitride material C_3N_5 as photocatalyst for CO_2 reduction to C1 and C2 products, JPS 76th Annual Meeting, The Physical Society of Japan, 2021 Mar 12th-15th, online, oral.

2. **Yuelin Wang,** Thanh Ngoc Pham, Likai Yan, Yoshitada Morikawa*, Density functional theory on nitrogen (N) doped graphdiyne as electrocatalyst for oxygen reduction reaction (ORR), The 9th International Symposium on Surface Science (ISSS-9), 2021 Nov 28th-Dec 1st, online, oral.
3. **Yuelin Wang,** Thanh Ngoc Pham, Likai Yan, Yoshitada Morikawa*, N_2 fixation on single B and double B doped g-C_9N_{10}: A density functional theory study, JPS 77th Annual Meeting, The Physical Society of Japan, 2022 Mar 15th-19th, online, poster.
4. **Yuelin Wang,** Yoshitada Morikawa*, Density functional theory study on a nitrogen-rich carbon nitride material C_3N_5 as photocatalyst for CO_2 reduction to C1 and C2 products, 日本表面真空学会関東支部セミナー 表面科学と原子層科学のエッジ, 2022 Mar 29th-30th, online, poster.
5. **Yuelin Wang,** Thanh Ngoc Pham, Yoshitada Morikawa*, Likai Yan*, Density functional theory study on a nitrogen-rich carbon nitride material C_3N_5 as photocatalyst for CO_2 reduction to C1 and C2 products, The 9th Tokyo Conference on Advanced Catalytic Science and Technology (TOCAT9), 2022, July 24th -29th , online, oral.
6. **Yuelin Wang,** Thanh Ngoc Pham, Likai Yan*, Yoshitada Morikawa*, Activity and selectivity of N_2 fixation on B doped g-C_9N_{10}: A density functional theory study, The 22nd International Vacuum Congress (IVC-22), 2022, September 11th-16th, Sapporo, poster.

Award

The Japan Society of Vacuum and Surface Science Best Female Student Award, 2022.